

Rotational spectroscopy
of acetone and its
mono- ^{13}C isotopologues

I n a u g u r a l - D i s s e r t a t i o n
zur Erlangung des Doktorgrades der
Mathematisch-Naturwissenschaftlichen Fakultät
der Universität zu Köln

vorgelegt von

Matthias Hakan Ordu
aus Köln

Köln, 2017

1. Gutachter: Prof. Dr. Stephan Schlemmer
2. Gutachter: Prof. Dr. Joachim Hemberger

Tag der mündlichen Prüfung: 22. April 2016

Für Alyssa Bunyola

Hinweis

Diese Dissertation berichtet über eines von zwei größeren Projekten, die ich während meines Promotionsstudiums am I. Physikalischen Institut der Universität zu Köln bearbeitet habe. Das zweite, nicht weiter dargestellte Projekt war die Entwicklung und der Aufbau eines Einseitenband-Heterodynempfängers um 345 GHz mit einem flüssig-heliumgekühlten Supraleiter-Isolator-Supraleiter-Übergang als erster Mischerstufe. Diese Technologie, die normalerweise in astronomischen Observatorien eingesetzt wird, sollte in diesem Gerät im Labormaßstab zur Detektion der extrem schwachen Linienemission von Probengasen in einem neuartigen Emissionsspektrometer genutzt werden. Die Fortschritte dieses Laborinstrumentierungsprojekts werden hier nicht weiter ausgeführt, da sich gezeigt hatte, dass beide Projekte für eine gemeinsame Darstellung in derselben Dissertation zu umfangreich sind. Mehrere Arbeitsgruppen des Instituts sind an diesem kollaborativen Projekt beteiligt und es wurden bis jetzt keine Ergebnisse daraus veröffentlicht.

Note

This thesis reports on one out of two larger projects which I pursued during my PhD studies at the I. Institute of Physics in Cologne. The second project, not reported here, was the development and construction of a single-side-band heterodyne receiver operating around 345 GHz, with its first mixer stage built as a liquid helium cooled superconductor–insulator–superconductor junction. This technology is normally deployed in astronomical observatories but was intended to be applied in a laboratory-scale device to enable the detection of extremely weak line emission from samples of molecular gases in a novel emission spectrometer. The proceedings of this laboratory instrumentation project are not reported here because it turned out that both projects were too extensive to be presented in one thesis. The collaborative effort involving several workgroups of the Institute is still ongoing and none of its results have been published elsewhere to date.

Kurzzusammenfassung

Aceton, $(\text{CH}_3)_2\text{CO}$, gehört zu den größten der fast 200 bis heute im interstellaren Medium oder in zirkumstellaren Hüllen entdeckten Moleküle. Die Ursprünge dieser chemischen Vielfalt sind Gegenstand der aktuellen astrochemischen Forschung. Der Vergleich interstellarer Häufigkeiten komplexer Moleküle (wie Aceton) und ihrer isotopensubstituierten Analoga (wie Aceton- ^{13}C) wird entscheidend sein, um die Reaktionswege zu identifizieren, die dieses Phänomen hervorgerufen haben, welches Berührungspunkte zu unserem Verständnis der Entstehung von Sternen und des Ursprungs des Lebens aufweist.

Der Nachweis eines Moleküls und die Vermessung seiner Häufigkeit kann nur gelingen, wenn eine präzise Vorhersage seines Rotationspektrums aus Laborbeobachtungen gewonnen wurde. Eine herausfordernde Aufgabe für jedes komplexe Molekül, doch umso mehr, wenn Gegebenheiten wie funktionelle Gruppen existieren, die sich in einer Oszillationsbewegung mit großer Amplitude befinden und so die Komplexität des Spektrums weiter erhöhen. Aceton, ein Molekül mit zwei Methylgruppen in oszillierender Torsionsbewegung, gehört zu den anspruchsvollsten bekannten Fällen in dieser Hinsicht, da die Kopplung zwischen diesen zwei Eigenbewegungen und der Rotation des Gesamtmoleküls hier besonders stark ist.

Erst im Jahr 2005 waren sowohl das Auflösungsvermögen und die Empfindlichkeit astronomischer Millimeterwellen-Observatorien als auch die Zuverlässigkeit der Vorhersage des Acetonspektrums so weit fortgeschritten, dass der Nachweis von Aceton im interstellaren Medium über ein provisorisches Niveau hinausgehen konnte. Damit war die Entwicklung jedoch nicht beendet: Die interstellaren Spektren der ALMA-Ära enthalten zahlreiche neue Linien, die

zu bereits entdeckten Molekülen gehören, ihnen aber nicht zugeordnet werden können, weil die vormals erfolgreichen Vorhersagen in manchen Quantenzahlenbereichen, die früheren Beobachtungen nicht zugänglich waren, zu ungenau sind.

Im Verlauf der Versuche, das Laborspektrum von Aceton-2-¹³C zu modellieren, wurde deutlich, dass die für den Bedarf der heutigen Astronomie nötige Vorhersagepräzision nicht erreicht werden kann, ohne Ergänzungen am Modell vorzunehmen. Im Anschluss daran konnte dieses erweiterte Modell ebenfalls erfolgreich auf das Spektrum von Aceton-¹²C angewendet werden.

In dieser Dissertation werden nach einer detaillierten Diskussion des erweiterten Modells die resultierenden Modellparameter vorgestellt, welche neue Vorhersagen für Aceton-¹²C, Aceton-1-¹³C und Aceton-2-¹³C erlauben. Ein erstes Beispiel, in dem Spektrallinien der korrigierten Vorhersage für Aceton-¹²C in einem Spektrum aus dem Sternentstehungsgebiet Sagittarius B2 erfolgreich identifiziert werden konnten, wird ebenfalls gezeigt.

Abstract

Acetone, $(\text{CH}_3)_2\text{CO}$, is among the largest of the almost 200 molecules so far detected in the interstellar medium or circumstellar shells. The origins of this chemical richness in space are a matter of current astrochemical research. Comparing the interstellar abundances of complex molecules (like acetone) to their isotopically substituted analogues (like acetone- ^{13}C) will be pivotal to identify the reaction pathways that have brought about this phenomenon which is touching our understanding of star formation and the origin of life.

Detecting an interstellar molecular species and measuring its abundance can only succeed if a precise prediction of its rotational spectrum has been derived from laboratory observations. This task is challenging for every complex molecule, but even more so if further complications like functional groups undergoing large-amplitude motions exist. Acetone, a molecule with two torsionally oscillating methyl groups, belongs to the most difficult cases known in this regard, as the coupling between these two large-amplitude motions and the overall rotation is especially strong.

It was not before 2005 that the resolution and sensitivity of astronomical millimetre-wave observatories and the reliability of the spectral prediction for acetone had proceeded so far that acetone could be detected in the interstellar medium in a way that was not tentative. However, the development did not end there: Interstellar spectra of the ALMA era contain plenty of new lines from already detected molecules which are not assignable to them because the once successful predictions are too imprecise in some quantum number ranges which were not detectable in the past.

During the attempts to model the laboratory spectrum of acetone-2-¹³C it became clear that the necessary precision for a prediction which will match the needs of modern astrophysics cannot be gained without amendments to the model. Afterwards, this enhanced model could be successfully applied to the spectrum of acetone-¹²C as well.

In this thesis, the resulting model parameters which enable new predictions for the rotational spectra of acetone-¹²C, acetone-1-¹³C, and acetone-2-¹³C are presented after a detailed discussion of the enhanced model. Furthermore, a first example is shown where spectral lines from the corrected prediction for acetone-¹²C were successfully identified in a spectrum from the star-forming region Sagittarius B2.

Contents

1	Introduction	1
2	Theoretical consideration	19
2.1	Overview	19
2.2	Energy spectrum of an asymmetric-top molecule . . .	20
2.3	General aspects of internal rotation	25
2.4	The ERHAM model	28
2.4.1	Nomenclature of the tunneling parameters . . .	41
2.4.2	Numerical implementation	42
2.5	Effects of symmetry	44
2.5.1	Four group symmetry	45
2.5.2	Permutational symmetry groups	46
2.5.3	Symmetry analysis of acetone- ^{12}C and $^{-13}\text{C}_1$	48
2.6	General spectral features	51
3	Experiments	57
3.1	Technical summary	58
3.2	Spectroscopy of acetone-2- ^{13}C	59
3.2.1	Measurements	59
3.3	Spectroscopy of acetone- ^{12}C	66
3.4	Spectroscopy of acetone-1- ^{13}C	67
3.4.1	Detection in natural abundance	67
3.4.2	Proposed experiment for an in-situ synthesis	73
4	Spectral analysis and results	80
4.1	Data analysis with AABS	80
4.2	Fitting procedure with ERHAM	82
4.3	Results for acetone-2- ^{13}C	91

4.3.1	Torsional ground state	91
4.3.2	First excited torsional state ($v_{12} = 1$)	110
4.4	Results for acetone- ^{12}C	117
4.5	Results for acetone-1- ^{13}C	118
5	Implications, summary and outlook	125
5.1	Related results	125
5.1.1	Acetone lines in an ALMA Sgr B2 spectrum	125
5.1.2	Dipole moment of acetone	127
5.2	Summary and Outlook	127
A	Tables from the theoretical formalism	130
A.1	Representations of molecular coordinates	130
A.2	Character and product tables	131
A.3	Correlation tables	137
B	Manufacturers and models	139

List of Figures

1.1	Structure of acetone and its <i>mono</i> - ¹³ C isotopologues	3
1.2	Subsequent improvement of a predicted acetone spectrum	16
2.1	Influence of rotational asymmetry on the general energy level scheme of a rigid, non-distorted molecule .	24
2.2	Lowest-order torsional potential of a threefold internal rotor	26
2.3	Influence of the barrier height on the torsional energy levels	29
2.4	ERHAM: Origin of seemingly forbidden transitions . .	54
2.5	Internal axes, atom positions and internal rotational directions in acetone	55
2.6	Acetone-2- ¹³ C: Observed relative intensities in the laboratory spectrum	55
2.7	Acetone-2- ¹³ C: Overview spectrum up to 1.5 THz . .	56
3.1	General setup of a source-modulated absorption spectrometer	58
3.2	MIDAS-COINS: Optical and vacuum setup	62
3.3	MIDAS-COINS: Absorption cells	63
3.4	MIDAS-COINS: Beam splitter system	64
3.5	Acetone- ¹³ C: Isotopic abundances	67
3.6	Acetone-1- ¹³ C: Predictive uncertainty, <i>J</i> dependence	69
3.7	Acetone- ¹² C: Distribution of line spacings in the predicted spectrum	70
3.8	Acetone-1- ¹³ C: Feasibility of acetone- ¹² C high-sensitivity measurements	72

3.9	Reaction scheme for the dry distillation of calcium acetate	73
3.10	DT-TG measurement of calcium acetate	74
3.11	Acetone-1- ¹³ C: Yield optimisation by acetic acid-2- ¹³ C content	76
3.12	Acetone-1- ¹³ C: Proposed experiment for an in-situ synthesis	78
4.1	AABS screenshot	81
4.2	AABS-ERHAM work sequence	82
4.3	ERHAM: Time complexity	84
4.4	Acetone-2- ¹³ C: Canonical fit statistics for J, N, f	102
4.5	Acetone-2- ¹³ C: Canonical fit statistics for (q, q') , obs.-calc., $(K_a - K_c)/(J + 1)$	103
4.6	Acetone-2- ¹³ C: J dependence of torsional and asymmetry splittings for $K''_a = 3$	104
4.7	Acetone-2- ¹³ C: Canonical fit, frequencies, K dep.	106
4.8	Acetone-2- ¹³ C: Canonical fit, splittings, K dep.	107
4.9	Acetone-2- ¹³ C: Canonical fit, errors, K dependence	108
4.10	Acetone-2- ¹³ C: Evidence for a v_{12} torsional satellite	112
4.11	Acetone-1- ¹³ C: Line confusion in natural abundance	118
4.12	Acetone-1- ¹³ C: Line splittings at 264 GHz	119
5.1	Acetone- ¹² C: New lines in ALMA Sgr B2 spectrum	126

List of Tables

2.1	Acetone- ^{12}C and - $2\text{-}^{13}\text{C}$: Spin weights	49
2.2	Acetone- ^{12}C and - $2\text{-}^{13}\text{C}$: Relative intensities and selection rules	50
2.3	Acetone- $1\text{-}^{13}\text{C}$: Spin weights	52
2.4	Acetone- $1\text{-}^{13}\text{C}$: Relative intensities and selection rules	52
3.1	Acetone- $2\text{-}^{13}\text{C}$: Measurement setups	60
4.1	Evaluation of non-canonical tunneling parameters	92
4.2	Acetone- $2\text{-}^{13}\text{C}$ ground state fit	96
4.3	Acetone- $2\text{-}^{13}\text{C}$, $v_{12} = 1$ fit	113
4.4	Acetone- ^{12}C : Fit results	114
4.5	Acetone- $1\text{-}^{13}\text{C}$: Fit results	122
A.1	Coordinate representations	130
A.2	C_s character table	131
A.3	C_3 character table	131
A.4	$C_{2v} / V(a, b, c)$ character table with e/o assignments	132
A.5	G_{18} character table	133
A.6	G_{18} product table	134
A.7	G_{36} character table	135
A.8	G_{36} product table	136
A.9	$G_{18}\text{-}\sigma$ correlation	137
A.10	$G_{36}\text{-}\sigma$ correlation	138

*Technology has never been a surrogate for a good idea –
but even a good idea can never replace instinct.*

Michael Cretu

Chapter 1

Introduction

Acetone, $(\text{CH}_3)_2\text{CO}$, is among the simplest asymmetric rotors featuring two methyl groups which undergo a large-amplitude torsional vibration [Fig. 1.1 a)]. This motion is subject to a potential barrier of a specific height, which defines the strength of coupling to the molecule's overall rotation and between the two rotors. Torsional-rotational coupling generally takes place within all molecules with two internal rotors, a fact which made it very difficult to obtain a correct model of the rotational energy spectrum for such molecules for several decades. Its especially low barrier, or equivalently its strong coupling, made acetone a touchstone molecule of rotational-torsional spectroscopy. The exploration of its spectrum and molecular properties was therefore pursued at the forefront of technical possibilities in spectroscopy and calculational performance. The detection of acetone in the interstellar medium raised new astrochemical questions, with changing perspectives but no definitive answers each time a new step of technology or predictive accuracy was reached. This thesis continues this development, which is outlined in the following, towards an unprecedented predictational quality of its rotational spectrum, and paves the way for future investigations of acetone formation in interstellar environments by presenting new predictions for the rotational spectra of its singly ^{13}C -substituted isotopologues.

Timeline of acetone spectroscopy

Before the announcement of ERHAM¹ in 1997, there were some sophisticated, but no comprehensive solutions to the problem of molecules with two internal rotors. Fits to the spectrum based on perturbative Hamiltonians, which were computationally very demanding and allowed for approximative predictions for lower quantum numbers only. On the experimental side, there was a continuous development towards increased sensitivity, frequency coverage up to the sub-millimetre range, resolution and data acquisition speed. Moreover, the correct torsional excitation frequencies and the barrier height could not be uniquely determined for a long time. Altogether, there was always a basis for a steadily recurrent interest in acetone spectroscopy.

Acetone belongs to the first organic molecules investigated [2] when microwave spectroscopy evolved after World War II [101]. In 1959, following two mostly unsuccessful attempts by other groups, Swalen and Costain published the first assignment of 16 microwave transitions of acetone [89] together with extensive further results (mentioned in the following), notwithstanding their small data set. This started a series of works to add more rotational transitions in line with the technical progress. Swalen and Costain's assignments were made possible by a new algebraic group they introduced to correctly handle the symmetry of wavefunctions for the special case of non-rigid molecules with C_{2v} symmetry; an approach which was consolidated by Myers and Wilson [72] only one year later. The symmetry calculations presented in Section 2.5 follow a slightly refined methodology [9, 10], which has grown over the years after, and use different groups which are, though, still isomorphic to those presented in these pioneering works.

The first broadband measurement of the infrared spectrum from 300 cm^{-1} was reported by Cossee and Schachtschneider in 1966 [14], who tried to assign the observed wavenumbers to vibrational and torsional modes using two different calculations. They also cited one wavenumber out of their measuring range from a publication which had recently assigned this line to the co-rotating torsional mode, but none of the works which appeared soon after could reproduce this value nor any other values ascribed to the higher energy

¹A phenomenological model based on an effective rotational Hamiltonian; see [32, 35]

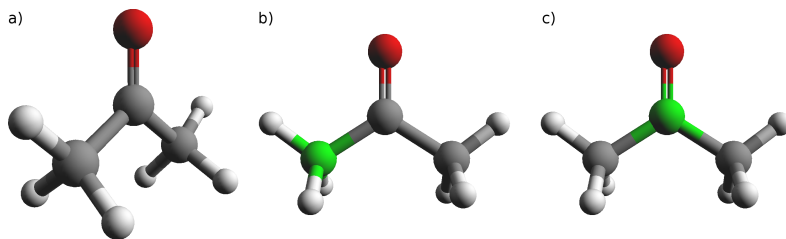


Figure 1.1: a) Equilibrium structure of acetone, $(\text{CH}_3)_2\text{CO}$, and its two *mono*- ^{13}C isotopologues acetone-1- ^{13}C [b)] and acetone-2- ^{13}C [c)], which were also spectroscopically analysed in this thesis. All molecular structures depicted herein were calculated with ArgusLab [91] using an AM1 Hamiltonian [18].

counter-rotating mode. Nonetheless, in 1972 a more comprehensive assignment of the strongest transitions was published by Mann and Dixon [61], and the order of transitions defined by their list has been used to number the vibrational modes of acetone since. It was not until 1986 that Groner *et al.* [37] were able to find an unambiguous value for the second torsional mode (ν_{17} , 124.5 cm^{-1}) in a Fourier transform infrared (FTIR) spectrum, and finally Kundu *et al.* [53] detected the first mode (ν_{12} , 77.8 cm^{-1}) in a Rydberg spectrum [63] in 1992.

By comparison of the torsional splittings with a Mathieu function table (cf. Section 2.3), Swalen and Costain were able to derive a value for the height of the barrier to internal rotation. Several contradictory values were published with later reports on rotational and vibrational spectroscopy works. Only a deeper analysis of the torsional potential function by Groner, performed with his new ERHAM method, brought clarity in 2000 [33]. He determined a value of $251.4 \pm 2.6\text{ cm}^{-1}$, which is quite low compared to more typical values such as approx. 950 cm^{-1} for dimethyl ether [34].

A significant step forward for molecules with two internal rotors was made when ERHAM was introduced in 1997 (see Section 2.4 or the original publications [32, 35]). While good results could already be achieved for single-rotor molecules with a perturbative treatment under the principle axis method (PAM) or the internal axis method (IAM) [59], this model could not be straightforwardly extended to molecules with two internal rotors because the indispensable coup-

ling terms could hardly be handled within a reasonable calculational framework to reproduce experimental accuracy. The ERHAM model is the logical extension of the concept of phenomenological Hamiltonians, which had been successfully used for single-rotor, quasi-rigid² molecules since the 1970s, to molecules with two symmetric internal rotors. Its advantages – mainly a complete handling of all coupling terms with merely one minor approximation of which no exceptions are known to date; adaptability to double-rotor molecules of arbitrary symmetry; and a substantial reduction of calculation time under full retention of all asymmetric rotor parameters – are counterbalanced by the loss of information about the torsional potential, which can only be inferred from additional, not purely rotational measurements. A FORTRAN implementation of a least-squares algorithm for the ERHAM model (called **ERHAM**), which, being the current state of the art [36], had since been used for the acetone predictions, was likewise used for the calculations in this thesis (Chapter 4).

With the great improvements of the ERHAM model at hand, it was obvious to try and fit spectra from the excited torsional states, too. This was accomplished for $v_{12} = 1$ in 2006 [38], and for $v_{17} = 1$ in 2008 [38].

The latest publication on the acetone spectrum reports an attempt to fit the given acetone data with a dedicated PAM program for molecules with two methyl rotors and C_{2v} symmetry [44]. Indeed, this non-phenomenological approach achieves an overall improvement of the fit by fitting parts of the data set better, yet other parts are fit worse. To date, the introduced programme does not yet allow for predictions and lacks the general applicability and computational efficiency of **ERHAM**.

The first, and still the most recent, spectroscopic work on acetone-¹³C₁ was published by Lovas and Groner [60] in 2006. They used a Balle-Flygare-type spectrometer (a resonator-based FTMW³ spectrometer, where the sample molecules are expanded into a cold jet), leading to sufficiently high sensitivity at low quantum numbers to see both *mono*-¹³C isomers of acetone in natural abundance. They reported observations of 11 rotational transitions, where the four torsional components (five for acetone-1-¹³C) could be assigned in all cases, giving a total of 44 (55) transitions. This thesis ties in with

²i.e., featuring only small-amplitude internal motions

³FTMW = Fourier-transform microwave

the predictions they made by extrapolation from measurements below 25 GHz.

Acetone in the interstellar medium

A new series of open questions was added to the acetone case when it was first detected by spectral observations of the extended star forming region Sagittarius (Sgr) B2 close to the Galactic centre by Combes *et al.* in 1986 [13]. This introduction shall give but a brief summary of the extensive literature in this field to outline the scientific context of this thesis within the research on interstellar acetone.

Interstellar molecules are detected by observations of their unique spectra⁴, which are usually seen in emission due to their internal excitation in dense molecular clouds ($T_{kin} \approx 10 - 300$ K) in front of the cold cosmic microwave background (2.725 K). These spectra must be compared to spectral predictions for the gas under interstellar conditions, which must be derived from laboratory observations under terrestrial conditions (i.e., higher pressure and room temperature). The accuracy of the predicted spectrum should exceed that of the observatories, which is usually the case if the respective molecular model can be fit to the assigned transition with experimental uncertainty (peak detection typically of the order $\Delta f/f \sim 10^{-7}$). At the time of its interstellar discovery, laboratory spectroscopy of acetone had proceeded up to ~ 300 GHz [95], and a prediction of sufficient precision for observations around 3 mm was available.

Combes *et al.* found lines of four rotational transitions ($J = 8$ and 9) in the source Sgr B2 (OH)⁵, at a time when it was not known that the nearby hot-core source Sgr B2 (N-LMH) is hosting a much larger number of complex⁶ organic molecules (COMs). Accordingly,

⁴The term “spectral fingerprint” alludes to the extremely strong dependence of line frequencies in rotational spectra on the molecular structure.

⁵Notable sources within the large Sgr B2 cloud include (OH), a region of strong OH maser emission, (N) about 1'19" to the north, and (M) in the middle between these regions. Sgr B2(N) contains the hot-core region (N-LMH), “Large Molecule H Heimat”, where an unusually large number of complex molecules has been found.

⁶The complexity ascribed to a molecular species strongly depends on the researcher’s point of view. While the complexity of enzymes or DNA is accepted as standard in organic chemistry or molecular biology, current astrochemical models are dealing with molecules consisting of not much more than 10 atoms [24].

the acetone lines were seen closely above the noise limit, partially merged with other unknown signals; and only few transitions were reported in total.

The first detection was therefore considered tentative by the astrophysical community [45, 94] until it could be confirmed with more sensitive instruments by Snyder *et al.* in 2002 [88]. One of their main goals was to determine the peak position of the acetone signal, which they found indeed towards Sgr B2 (N-LMH). They were able to assign 20 further acetone lines, based on the good quality of the extensive prediction by Groner *et al.* [36] which had just been published. Snyder *et al.* derived a column density about three orders of magnitude greater than Combes *et al.*, which is partially a result of more up-to-date assumptions about the source structure and temperature (170 K instead of 20 K). From this result they derived a fractional abundance of $(4 - 30) \cdot 10^{-10}$ with respect to H_2 , about 600 times higher than the original value by Combes *et al.* They discussed their findings in the light of several earlier works by Herbst *et al.* and concluded that the amount of acetone in Sgr B2 (N-LMH) still cannot be explained by a formation solely in the gas phase. Eventually, Snyder *et al.* were also the first to record a contour map of one spectral line, which showed a compact, ellipsoidal object.

Combes *et al.* also suggested a gas-phase reaction scheme for interstellar acetone formation from acetaldehyde: The radiative association $\text{CH}_3^+ + \text{CH}_3\text{CHO} \rightarrow \text{CH}_3\text{COCH}_4^+ + h\nu$, followed by the dissociative recombination $\text{CH}_3\text{COCH}_4^+ + e^- \rightarrow (\text{CH}_3)_2\text{CO} + \text{H}$. In 1990, however, Herbst *et al.* [40] presented evidence that the rate coefficient of the proposed radiative association might be too low to explain the observed abundances, and suggested further observations towards the Orion compact ridge, where organic molecules had been detected at higher abundances than could be explained from known reaction rates [24, 26].

It took until 2005 that acetone was detected in Orion KL⁷ by Friedel *et al.* [23]. Until then, Orion KL was considered as harbouring nitrogen-bearing molecules at the hot core, spatially distinct from oxygen-bearing molecules at the compact ridge, making it a good object to study the influence of local conditions on interstellar chemistry. Contrastingly, Friedel *et al.* found acetone towards

⁷Kleinmann-Low nebula, the most active star forming region within the Orion Nebula and the closest source where massive star formation can be observed.

the hot core, but not above 3σ towards the compact ridge, suggesting an influence of nitrogen chemistry on acetone formation. This idea was not too unrealistic, as the picture of interstellar chemistry had changed from pure gas-phase reactions to gas-grain chemistry in the meantime, where catalytic reactions within the ice mantles of interstellar dust grains take place at lower cloud temperatures and the onset of star formation triggers a sublimation of the products through heating.

Since then, research on interstellar acetone strongly accelerated. After one confirmation by Goddi *et al.* in 2009 [28], two later papers by Friedel and Widicus Weaver [22,100] were the first to lower the confusion about interstellar acetone a little. They reported the first study of Orion KL at high angular resolution and substantially improved sensitivity, involving the spectra of eight molecular species. They found that the model of chemical differentiation between nitrogenic and oxygenic species, which had arisen from the lower sensitivity of former astronomical equipment, had to be given up, as all complex molecules considered within their study showed a much greater spatial overlap at lower abundances. Acetone was found mainly in parts of the cloud where the overlap between ethyl cyanide ($\text{C}_2\text{H}_5\text{CN}$) and acetic acid (CH_3COOH) was greatest. Interpreting this result as showing a link between the formation of these two species and acetone would be too early, as Orion KL hosts many other species which had not been considered in this study. Friedel and Widicus Weaver also analysed the dynamics of the same species and found that acetone seems to be robuster against changing physical or chemical conditions than other complex molecules. It is seen close to the hottest structures of the region (rotational temperatures of methanol, CH_3OH , up to ~ 400 K), but not actually tracing them.

The latest publication on acetone in Orion KL by Peng *et al.* 2013 [77] is an independent PdBI⁸ survey of Orion-KL focusing purely on the problem of acetone formation. While their observations (including lines around 225 GHz for the first time) are similar to those reported by Widicus Weaver and Friedel, they conclude that an alternative formation path involving N-bearing molecules should exist which is missing in all previous models on acetone formation in Orion-KL.

Only two months earlier, a third interstellar source containing

⁸Plateau de Bure Interferometer, operated near Grenoble, France

acetone was found by Codella *et al.* with the high-mass young stellar object G24.78+0.08 [12]. The detection is only tentative because only one acetone transition ($18_{4,14} \leftarrow 17_{5,13}$), with all four components overlapping, matches a particular pattern observed in one of the 2 GHz SMA⁹ sidebands, but it is still reasonable because acetone is expected to trace star forming regions. The most recent publication on interstellar acetone by Rong *et al.* 2015 reports a detection (by thirteen lines) in one further high-mass star forming region, W51 North [84]. Among investigations concerning other species, they found hints that grain-surface reactions may be more suitable to explain acetone formation, while the structurally similar dimethyl ether [(CH₃)₂O] should rather have a gas-phase formation route similar to that of methyl formate (CH₃OCHO). A rotational temperature of 140 K could be derived.

The greater picture: Star formation and interstellar chemistry

The development of interstellar acetone detections is exemplary for the changes observational (sub-)millimetre astronomy is currently undergoing, and the challenges still to be mastered to gain a coherent picture of interstellar chemistry. See [98] for an excellent review article by W. D. Watson (1976) where the basic, and still valid, foundations of modern astrochemistry are collected.

Interpreting interstellar molecular spectra is highly demanding for a number of reasons. To detect an interstellar molecule, one must know the frequencies and intensities of all of its spectral lines within the observed frequency range with a precision that matches or exceeds that of the telescopes. The observed intensities depend on the molecules' rotational temperature; if candidate lines are found, the absolute intensity of the predicted spectrum can be scaled to match the observed spectrum. The frequencies are Doppler shifted by a usually inhomogeneous velocity distribution of the source. The connections between observed spectra and physical conditions make interstellar spectroscopy a highly sensitive tool, often even the only one, to explore these conditions and thus gain an understanding of the complex processes underlying interstellar chemistry.

Interstellar spectra are composed from the emission of all species

⁹Submillimeter Array, operated at the Mauna Kea Observatory, Hawai'i, USA

present in the observed source. With increasing molecular complexity, the total emitted power spreads over a growing spectral density, which leads to a decreasing specific line intensity. As a result, one observes a superposition of some very strong, usually well-separated lines from smaller species, and a background of increasingly merged weak lines originating from the more complex species. For this reason, the correct absolute intensities for newly investigated species – especially for the complex ones, dubbed “molecular weeds” by astronomers –, which are needed to derive their relative abundances, can be correctly determined only if one knows the intensities of all other species participating in blended lines. Superposition also lowers the number of lines which can be uniquely assigned to a certain species, which is hampering the detection of complex species in particular.

Deriving the abundance of an interstellar molecular species from column densities, which in turn are calculated from the flux densities received from unique emission lines of such species, is crucial to gain a correct quantitative understanding of interstellar chemistry. There are several technical problems relating to column density determinations, see e.g. the discussion in [100]. An additional source of error arises from the predicted intensities: The molecular model based on laboratory work must provide a correct estimate of the partition function Q , where all energy levels populated at a given temperature have to be taken into account. This is especially important for molecules like acetone, which exhibit low-lying vibrational or torsional states (e.g. acetone’s $v_{12} = 77.8 \text{ cm}^{-1}$, corresponding to an excitational temperature of 112 K) that are significantly populated even in cooler interstellar sources.

Interstellar molecules are observed in a multiplicity of sources with distinct chemistries. The largest, fully hydrogenated organic molecules are found in hot molecular cores [8]. These dense, compact clouds show temperatures above 100 K and are typically found in active star-forming regions. The research interest in rotational spectra of complex organic molecules (COMs) is therefore also driven by the astrophysical research on star formation [41, 86]. Progress in understanding this highly complex, turbulent, feedback-driven, multi-scale process is currently fostered by an international interdisciplinary effort, combining approaches like magnetohydrodynamics, quantum thermodynamics, astrochemistry and numerical simu-

lations.

Stars form out of interstellar gas and dust clouds on billion-year timescales. While the presence of molecules and their rise in complexity with increasing (proto-)stellar mass is clearly evidenced, the role molecules play during star formation is still unclear. For instance, recent investigations [27] suggest that the presence of molecules is not a compulsory prerequisite to star formation (which would be inconsistent with primordial star formation from atomic hydrogen), but rather the conditions leading to gravitational mass accretion up to stellar scale are favouring molecular growth, too. On the other hand, molecules are thought to play an essential role during the gravitational collapse of a molecular cloud into a proto-stellar core, as they regulate the thermal budget of a proto-stellar core by broadband emission of photons, antagonising collisional heating and thus allowing the collapse to proceed.

A realistic model of star formation cannot be obtained without a sufficient knowledge of the underlying processes on all scales. Basic to everything else is the microscopic scale, involving quantum mechanical, thermal and electromagnetic interactions of the available ingredients (atoms and molecules, ions and radicals, dust, cosmic rays, etc.) with each other and their surroundings. The molecules form a major constituent and energy reservoir of this scale. Particular questions regarding the molecules include:

- Which physical processes can a molecule principally undergo during its lifetime (e.g. charge-transfer reactions, dissociative recombination, etc., see e.g. [92])?
- Which of these processes are selected by the physical and chemical conditions of the particular star just forming (e.g. temperature, transient shock waves, local radiation / PDRs¹⁰, static electromagnetic fields, spatial distribution of atomic species, etc.)?
- The speed (i.e., rate coefficients) of the possible chemical reactions, within the ice mantles of dust grains or in the gas phase, at the given ambient temperatures
- The sequence of changes to the conditions (e.g. molecular

¹⁰photon dominated regions or photo-dissociation regions

evaporation from grain surfaces in response to increased temperature) and their timing

- The degree of molecular complexity reached by this sequence of processes before star formation is completed
- The complex process of incorporation of these molecules into the circumstellar proto-planetary disk.

The prevailing picture of molecule formation in interstellar conditions – a fact deemed impossible not a hundred years ago – is that atoms, ions, radicals and small molecules condense onto cold dust grains, coating them into an ice mantle. Their mobility in ice is low, but not zero, just enough to migrate the ice and occasionally, if activation energy is present, undergo chemical reactions with other ice-mantle species. This way, they outlast captured until the dust is heated up during the onset of star formation. In the gas phase, with increased mobility and direct exposure to radiation, further reactions become possible, increasing molecular complexity if destructive processes are not dominating. A review article representing the state of the art in gas-grain chemistry modeling as of 2008 is [24].

One open question in astrochemistry is the role of carbon monoxide. It is the most abundant molecule containing carbon and, due to its sole composition of carbon and oxygen, of high influence on both carbon and oxygen chemistry in the ISM. While its high abundance is a hint that the formation of organic molecules should usually start from CO, observations of highly unsaturated carbon species in cold environments, in conjunction with the overabundant element hydrogen, suggest that COMs could also be formed from these by subsequent hydrogenation reactions during cloud collapse and heating.

Further interesting questions exist regarding the molecular complexity created by interstellar chemistry. For instance, one may ask whether molecules like *n*-propyl cyanide (C_3H_7CN), which base on a carbon chain, are the product of a pure carbon chain undergoing hydrogenation, or built from smaller precursors like e.g. methyl cyanide and ethanol in a more modular way; whether molecules like acetone ($(CH_3)_2CO$) containing a C=O double bond were formed from carbon monoxide by methyl addition or from a pure hydrocarbon by oxygen addition; or whether the formation of branched isomers [4] or conformers, like *tert*-butyl cyanide or *gauche-anti n*-butyl cyanide,

is disadvantaged from linear configurations like *anti-anti n*-butyl cyanide, as is known from chemistry on earth [75]. As interstellar molecules form under conditions far from thermal equilibrium, future detections of exotic conformational isomers (conformers) of known molecules in the ISM can be expected. Observations and analyses of interstellar conformational abundances in comparison to their equilibrium distribution, based on their differing formation energies, are expected to give new insights into interstellar chemistry.

The interest in interstellar COMs does not end with star formation and astrochemistry *per se*. Besides their suitability as highly sensitive probes for the local physical conditions within a source, it is peculiar that all species with more than five atoms identified so far are organic [41]. They are therefore capable of forming species (not yet detected) which could have been the molecular precursors of life on Earth. It is an important conceptual difference whether molecules enabling the formation of life were formed in the ISM and have only been transported to Earth, meaning that this process may happen in any other planetary system as well, or if conditions on Earth are so “special” that life has accidentally formed here from minor precursors. While more than 80 different amino acids of most probably extraterrestrial origin¹¹ have been found in meteorite cores and even in a sample of cometary outflow to date [6, 19, 54], only one presumed precursor of glycine, the smallest proteinogenic amino acid, could be identified in the ISM [3, 87].

Isotopic abundances in the ISM

Isotopically substituted molecules, which are also called isotopologues, and their respective isomers called isotopomers, are especially interesting for interstellar astronomy. Lighter or heavier atoms introduce slight changes to the adjacent bond lengths, thereby shifting the frequencies of all spectral lines, and sometimes even changing molecular symmetry, which usually strongly impacts the appearance of the whole spectrum. If, for instance, one methyl carbon atom in acetone ((CH₃)₂CO) is replaced by ¹³C, the symmetry of the main isotopologue is broken (see Section 2.5) and each rotational transition splits into five components, with a different intensity pattern, instead of the four components known from the main isotopologue.

¹¹As suggested by their isotopic signatures and racemic mixture.

Isotopologues also behave different chemically, which becomes especially apparent at cold cloud temperatures (some 10 K) which are small compared to the energy released during exothermal reactions like $\text{H}_3^+ + \text{HD} \rightarrow \text{H}_2\text{D}^+ + \text{H}_2$ (230 K) or $\text{CH}_3^+ + \text{HD} \rightarrow \text{CH}_2\text{D}^+ + \text{H}_2$ (370 K) [45]. In the past decades, many interstellar objects were found to host molecules with isotopic signatures exceeding the cosmic values, sometimes by many orders of magnitude [64]. Isotopes are often inherited to more complex species along preferred reaction paths, leading to a strong enhancement for one species and depletion for the others. For more than four decades [99], the fractionation reactions leading to interstellar isotopic enhancement or depletion have been subject to ongoing observations [102], calculations [65], theoretical works [85], and experiments [43].

As regards carbon-13, it has been calculated to get strongly enriched in carbon monoxide by cold gas-phase ion-neutral reactions [20, 55]. For this reason, astronomical observations with the aim to obtain reliable values for the abundances of interstellar singly ^{13}C -substituted species can give strong hints on the role CO plays in the formation of a molecule or its constituents. Furthermore, it is possible that many of the still unknown interstellar spectral lines (“U lines”) belong to signals from enriched isotopologues whose laboratory spectra simply have not yet been analysed. In their review article on complex organic interstellar molecules [41], Herbst and van Dishoeck mention a millimetre-wave survey [90] where the number of U lines was reduced from roughly 8000 to 6000 after some spectral data from isotopologues and excited states of known species had been added to the catalogue.

Observations of interstellar isotopic signatures thus are a promising tool to gain insight into the complex phenomena of interstellar chemistry. Signatures may be compared between different interstellar regions, different conformational or other isomers of the same species, or molecules of high structural similarity but possibly a different formation path, such as dimethyl ether, $(\text{CH}_3)_2\text{O}$, and acetone, $(\text{CH}_3)_2\text{CO}$. For instance, acetone has to date been found only in two high-mass star forming regions, whereas dimethyl ether is also found in the low-mass star forming region IRAS 16293 – 2422 [11]. It is questionable whether this non-detection originates from a lack of sensitivity or differences in the chemistry of these particular regions. Isotopic signatures, being a sensitive and versatile probe for

the conditions and history of a given site, can also help solve the ever-returning question whether a species is formed in the gas phase or on grain surfaces [52], and they increasingly come into play as several new astronomical observatories for the (sub-)millimetre region have recently been launched or are getting finished these days.

Ongoing technical developments in observational and laboratory astronomy

The interpretation of astronomical spectra has widely evolved since Fraunhofer's first observations of the visible solar spectrum with its famous absorption lines from atoms in the solar atmosphere. Besides recording the position, intensity, polarisation and time dependence of astronomical sources, spectral analysis is still the most important means to gain insight into their physical and chemical conditions. To date, nearly all spectral regions are covered by a number of observatories, one of the technically most demanding being the THz regime [16]. Together with the microwave / millimetre-wave region, this part of the electromagnetic spectrum reflects the characteristic energy scale for the excitation of molecular rotation. As the spectral transition frequencies of a molecule are characteristic for its structure and the intensities depend sensitively on its physical state, (sub)millimetre spectroscopy is the method of choice to investigate the chemical composition and the physical conditions of cold to warm inter-, circum-, and protostellar gases.

However, a clear identification of an interstellar molecular species is difficult because the beam arriving at a telescope usually contains signals from a large number of species within the same source, producing a dense spectrum with many spectral lines superposed. A sufficiently large number of spectral lines can be identified only if precise predictions of spectral line frequencies and intensities exist for each of the known species at the model temperature of the source. With increasing molecular complexity (i.e., large weight and asymmetric structure), the spectra become denser and weaker at the same time. For these reasons, collaborations of the most sensitive spectroscopic laboratories and astronomical observatories are essential to expand our understanding of the mechanisms which have formed this variety of molecules under interstellar conditions [86]. More

than 180 molecular species¹² have been found by spectral analysis of interstellar molecular clouds and circumstellar envelopes to the current date.

The previous paragraphs already hinted at the current situation of missing spectral predictions derived from laboratory spectroscopy. The astronomical (sub-)millimetre observatories of the latest generation, above all the Stratospheric Observatory for Infrared Astronomy (SOFIA, [42]), the Atacama Large Millimetre / submillimetre Array (ALMA), the already exhausted Herschel satellite [15] or the upcoming Northern Extended Millimetre Array (NOEMA), are unprecedented in sensitivity and angular and frequency resolution. Interstellar maps and spectra are about to be unveiled in ever more detail, and signals from isotopologues and excited torsional states of many known species will become visible for the first time. Obtaining reliable and precise spectral predictions for the prospective species in this vein is among laboratory astrophysics' major jobs for the next decades [71].

Another consequence of this technical progress, which is especially relevant for COMs, is that earlier spectral predictions, which may have sufficed for past astrophysical detections, have grown too inaccurate to serve as a data source for spectral analysis of the data generated by the new-generation observatories. Any imprecision in predicted spectra can become influential if one wants to model the correct intensities of stronger superposition lines or detect an unknown species with lines of similar intensity. The complex interstellar species are therefore sometimes dubbed “weed molecules”, which are to be separated from the species of interest. Past works on astrophysical spectra relied on calculated line frequencies which used to reside within an acceptable range around the true frequencies. The width of this range was a direct consequence of larger line widths or other experimental uncertainties encountered in earlier laboratory spectra. With their new spectrometric equipment, showing enhanced sensitivity and frequency resolution, modern observatories have stricter acceptability limits for predictive deviations. Moreover, transitions with quantum numbers beyond the boundaries of former fits (meaning weaker branches and higher quantum numbers, especially in K) are now observed in astronomical data for the first time, but cannot be correctly identified because the old predictions for

¹²Source: Cologne Database for Molecular Spectroscopy, CDMS [68–70]

such branches are systematically shifted from the true frequencies.

An example involving recent ALMA 3-mm data is presented in Chapter 5 to show that the latter effect can be striking for challenging molecules like acetone. Improved spectral predictions for acetone may also be of use for atmospheric research, where acetone was found to be an atmospheric pollutant [1, 17] intervening with ozone chemistry.

A closer inspection of an acetone spectrum measured in the labor-

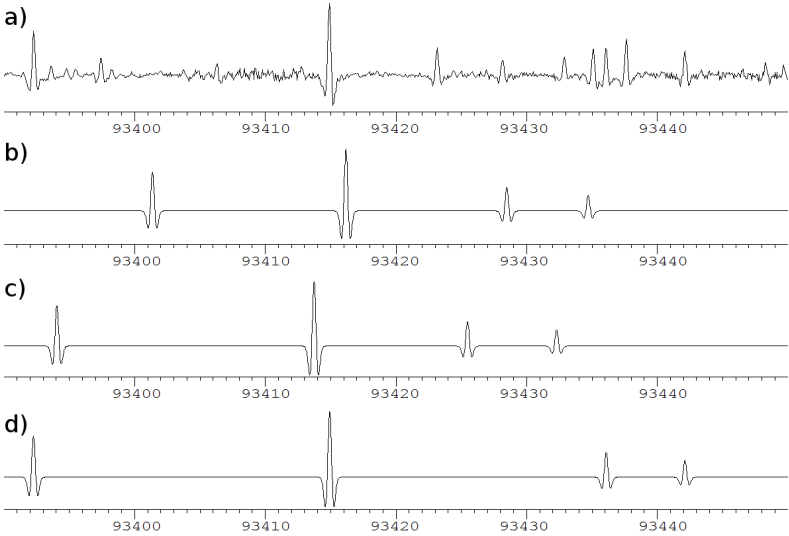


Figure 1.2: The four component lines of the acetone- ^{12}C transition $27_{15,12} \leftarrow 27_{14,13}$ as seen in a spectrum measured in the laboratory [a]; see Section 3.3] and predicted from three different fits [b) to d)]. Starting with the prediction by Groner *et al.* [b)], the fit was repeated after four lines, which would seemingly match the predicted intensity pattern in the depicted frequency range, and a handful of others had been added to the data set. The resulting prediction [c)] showed significant shifts towards the assigned frequencies, but no satisfactory agreement. Spectrum d) shows the final prediction according to a revised fit (see Section 4.4) after about 1000 new assignments in the range 38 – 130 GHz. Frequencies are given in MHz.

atory [Fig. 1.2 a)] shows that correct assignments of line frequencies often cannot be obtained straightforwardly: In the prediction from the JPL catalogue¹³ [spectrum b)], the discrepancy is clearly visible for the strongest component. For the three weaker components, one is tempted to assign nearby lines (such as the the two lines between 93420 and 93430 MHz) as candidates. This was tried as a first approach, together with a handful of other *Q*-branch lines which seemed to be easily assignable, and yielded the prediction shown in spectrum c). The fit was flexible enough to shift the lines towards the assigned positions, but a true fit within experimental uncertainty could not be reached. Only a more comprehensive analysis (presented in Section 4.4) with a new set of parameters found following a non-standard procedure (discussed in Sections 4.2 and 4.3.1), and a data set of twice the original size brought a full convergence on these four lines with the correct intensity pattern, but the actual positions of the two weakest components being far from the original candidates. Interestingly, these four lines are a nice example where correct predictions were finally achieved although none of them were assigned for the extended data set.

Thesis overview

This thesis reports on the least-square fits of an extended ERHAM model to assigned spectral lines from the torsional-vibrational ground state of acetone and its isotopologues acetone-1-¹³C and acetone-2-¹³C. For the latter species, also the lowest torsionally excited state was fitted. The theory of molecules with two internal rotors and the ERHAM model are presented in Chapter 2 together with symmetry considerations. Chapter 3 describes all experiments performed to measure portions of the absorption spectra of said molecules, and suggests a future experiment which would be adequate to measure the spectrum of an enriched sample of acetone-1-¹³C, which could only be measured in natural abundance so far. All spectral measurements on acetone and its two ¹³C isotopologues were performed at the I. Institute of Physics¹⁴, University of Cologne. Detailed explanations of the fitting procedure and the resulting parameters obtained for each species are given in Chapter 4. In Chapter 5 a case study

¹³A database of molecular rotational spectra hosted by the NASA Jet Propulsion Laboratory [67]

¹⁴Hereafter called “the Institute”.

is shown where the new predictions for the main isotopologue have been used to find interstellar spectral lines which were predicted wrongly before. The chapter continues with a short comment on the prevalent literature values of the dipole moment of acetone and closes with a summary of the results and an outlook on future works needed to accomplish what was started here. Tables from the theory chapter and additional information on the laboratory equipment used during the measurements have been collected in the Appendix (page 130).

Chapter 2

Theoretical consideration

2.1 Overview

The appearance of the rotational spectrum of a large class of molecules, including acetone, derives from the fact that their respective equilibrium structure constitutes an asymmetric top. The term asymmetry is meant here purely in terms of the mass distribution which becomes effective during a molecule's overall rotation. In mathematical terms, the geometrical arrangement of its nuclei results in three different non-zero components in the diagonalised moment of inertia tensor. This rotational asymmetry is independent of the symmetry operations existing for the point group formed by the equilibrium structure of its nuclei. The spectrum of a general asymmetric-top molecule is described in the standard literature [30, 93] and summarised in Section 2.2.

A major effect in the spectrum of acetone arises from the collective torsional motion of the hydrogen atoms located in each of the two methyl groups with respect to the rotating frame (Section 2.3). This internal large-amplitude motion (LAM) couples to the molecule's overall rotation, causing a splitting of each asymmetric rotor line into four components (five for acetone-1-¹³C). While spacing and order of these torsional components can vary strongly with the rotational state, their intensity distribution always follows one out of two patterns, depending on the rotational quantum numbers involved in the transition. Intensity patterns and selection rules for

acetone- $^{13}\text{C}_1$ are explained in Section 2.5 within the group theoretical framework described in the literature [9, 10].

Reconstructing the full torsional-rotational Hamiltonian from assignments of recorded spectra is computationally too demanding to establish a reasonable workflow which allows for iterative assigning and fitting. A practical, time-saving procedure to calculate an effective rotational Hamiltonian (ERHAM) has therefore been established, together with a homonymous FORTRAN program, by P. Groner in 1997 [32]. It builds upon the insight that the Hamiltonian depends periodically on the rotational quantum numbers and symmetry labels, and applies several approaches, including molecular symmetry, to simplify the calculation as much as possible. The theory behind this effective model and its software implementation ERHAM [47] is outlined in Section 2.4. The program ERHAM cannot be used to determine the potential energy surface (PES) of a molecule only from its rotational spectrum, but it has proven its practical use to fit and predict rotational spectra of molecules with two or more internal periodic large-amplitude motions, see e.g. [52].

The general appearance of the rotational spectra of acetone- ^{12}C and $^{13}\text{C}_1$, as derived from the theory presented, is explained in Section 2.6.

2.2 Energy spectrum of an asymmetric-top molecule

The general theory of a rotating asymmetric molecule has been extensively described in the literature [30, 93]. It starts with the classical Hamilton function of a freely rotating rigid body,

$$\mathcal{H} = \frac{\hbar^2}{2} \left(\frac{P_a^2}{I_a} + \frac{P_b^2}{I_b} + \frac{P_c^2}{I_c} \right) \quad (2.1)$$

$$= AP_a^2 + BP_b^2 + CP_c^2 \quad (2.2)$$

which is formally identical to the quantum mechanical Hamilton operator by straightforward application of the principle of correspondence. The labels a , b and c of the principle axes of inertia are chosen such that the principal moments of inertia fulfill the relation $I_a \leq I_b \leq I_c$. A rearranged form of eq. (2.2) more useful for

spectroscopy is

$$\mathcal{H} = \frac{1}{2}(A + C)P^2 + \frac{1}{2}(A - C)\mathcal{H}(\xi) \quad (2.3)$$

with $P^2 = P_a^2 + P_b^2 + P_c^2$, the reduced Hamiltonian $\mathcal{H}(\xi) = P_a^2 + \xi P_b^2 - P_c^2$ and the asymmetry parameter $\xi = 2B - A - C / (A - C)^1$. The two limiting cases which can generally be discerned for a rotating asymmetric body are the prolate top ($I_a = I_b < I_c \Rightarrow \xi = -1$) and the oblate top ($I_a < I_b = I_c \Rightarrow \xi = +1$). Although the theory of the asymmetric top deals with all other non-spherical² configurations, i.e., $-1 < \xi < +1$, its quantum mechanical treatment is based on the symmetric-top solutions of the Schrödinger equation, which are therefore displayed in the following.

The symmetric rotor

Two further axes systems are important for a proper description of a rotating molecule: The space-fixed or laboratory axes system X, Y, Z and the body-fixed or molecular axes system x, y, z , which is usually chosen according to symmetry considerations. In many cases it is advantageous to have the x, y, z system coinciding with the a, b, c system, and one out of six assignment possibilities called representations is chosen (See Table A.1). The representations of choice for near-prolate and near-oblate tops are I^r and III^l , respectively, where the z axis coincides with the symmetry axis a or c to yield a Hamiltonian of most simplified structure.

In a force-free environment, which can be assumed for all experiments described here, the total angular momentum and its direction in the laboratory frame are conserved:

$$\frac{d\mathbf{P}}{dt} = \hat{\mathbf{X}} \left(\frac{dP_X}{dt} \right) + \hat{\mathbf{Y}} \left(\frac{dP_Y}{dt} \right) + \hat{\mathbf{Z}} \left(\frac{dP_Z}{dt} \right) = 0 \quad (2.4)$$

This is still true in the rotating frame, but in the corresponding equations (Euler's equations of motion) an additional fictitious torque $\boldsymbol{\omega} \times \mathbf{P}$ called Euler force occurs as a compensation for the change of

¹The asymmetry parameter is called κ in the literature. This would create confusion here, however, because κ is also an important parameter in the ERHAM model.

²Bodies with $I_a = I_b = I_c$ are called spherical rotors.

coordinates:

$$\hat{\mathbf{X}} \left(\frac{dP_x}{dt} \right) + \hat{\mathbf{Y}} \left(\frac{dP_y}{dt} \right) + \hat{\mathbf{Z}} \left(\frac{dP_z}{dt} \right) + \boldsymbol{\omega} \times \mathbf{P} = 0 \quad (2.5)$$

For an appropriate representation, the equality of the moments of inertia typical for symmetric tops is inherited to x and y , and it follows from Euler's equation of motion for the z component,

$$\frac{dP_z}{dt} + \left(\frac{1}{I_x} - \frac{1}{I_y} \right) P_x P_y = 0 \quad (2.6)$$

that P_z is conserved, too. The operators P_Z, P_z , and $P^2 = P_X^2 + P_Y^2 + P_Z^2 = P_x^2 + P_y^2 + P_z^2$ therefore have common eigenfunctions $|JKM\rangle$ with the Hamiltonian, with quantum numbers defined by the algebraic properties

$$\langle JKM|P^2|JKM\rangle = \hbar^2 J(J+1), J \in \mathbb{N}_0 \quad (2.7a)$$

$$\langle JKM|P_z|JKM\rangle = \hbar K, -J \leq K \in \mathbb{Z} \leq J \quad (2.7b)$$

$$\langle JKM|P_Z|JKM\rangle = \hbar M, -J \leq M \in \mathbb{Z} \leq J \quad (2.7c)$$

The energy levels of the two symmetric-top cases are thus found to be³

$$\langle J, K|\mathcal{H}_R^{(P)}|J, K\rangle = h[BJ(J+1) + (A-B)K^2] \quad (2.8)$$

for the prolate case, and

$$\langle J, K|\mathcal{H}_R^{(O)}|J, K\rangle = h[BJ(J+1) + (C-B)K^2] \quad (2.9)$$

for the oblate case. Note that K measures the projection of angular momentum on the respective symmetry axis a or c , and that the energy depends quadratically on both J and K . As a consequence, except for $K = 0$, the energy levels do not depend on the sign of K and are therefore doubly degenerate. A prolate top features a series of energies increasing with K for a given J , whereas the same series is decreasing for an oblate top.

³Eigenfunctions and -values are independent of M due to momentum conservation.

The distorted asymmetric rotor

For a slightly asymmetric top the direction of angular momentum with respect to a symmetry axis makes a difference in rotational energy, and the aforementioned symmetric-top degeneracy is lifted. This effect is called asymmetry splitting and is best observed with transitions involving low- K states (see Fig. 2.1). In highly asymmetric molecules ($\xi \approx 0$) the splittings become so large that the levels are better considered K -independent. Indeed, K is not a quantum number any more, but as the energy shifts are continuous in ξ , the asymmetric energy levels can still be uniquely assigned to one symmetric-top level of either symmetry. The differently defined K values are written with subscript a and c , respectively, to enable an unambiguous labeling $J_{K_a K_c}$ of the asymmetric rotor levels. Each level belongs to one of the cases $K_a + K_c = J$ or $K_a + K_c = J + 1$. For a given J , the levels form a stack with a unique enumeration scheme, starting from the lowest energy level $(K_a, K_c) = (0, J)$ and alternately increasing K_a by 1 and decreasing K_c by 1 until the top level $(K_a, K_c) = (J, 0)$ is reached.

This idealised energy level scheme is altered by effects of centrifugal distortion. Depending on the rotational state, centrifugal forces will change the molecular geometry. In the Hamiltonian this can be expressed by additional terms of higher order in the angular momentum components. The most general form of a Hamiltonian which allows for fitting experimental data without containing indeterminate constants is the so-called standard Hamiltonian developed by Watson [97]:

$$\mathcal{H}_{st} = \sum_{p,q,r=0}^{\infty} h_{p,q,r} (P_x^p P_y^q P_z^r + P_z^r P_y^q P_x^p) \quad (2.10)$$

Time-reversal symmetry and hermiticity enforce the order $n = p + q + r$ of all terms to be even. Furthermore, for molecules of orthorhombic symmetry⁴ it is found that all odd powers p , q , r of angular momentum components must be zero. With a unitary transformation and a number of redefinitions and simplifications a reduced form for strongly asymmetric tops (“ A reduction”) can be reached, which is shown here up to $n = 8$, the highest order used for

⁴Orthorhombic molecules belong to one of the point groups C_{2v} , V_h or V .

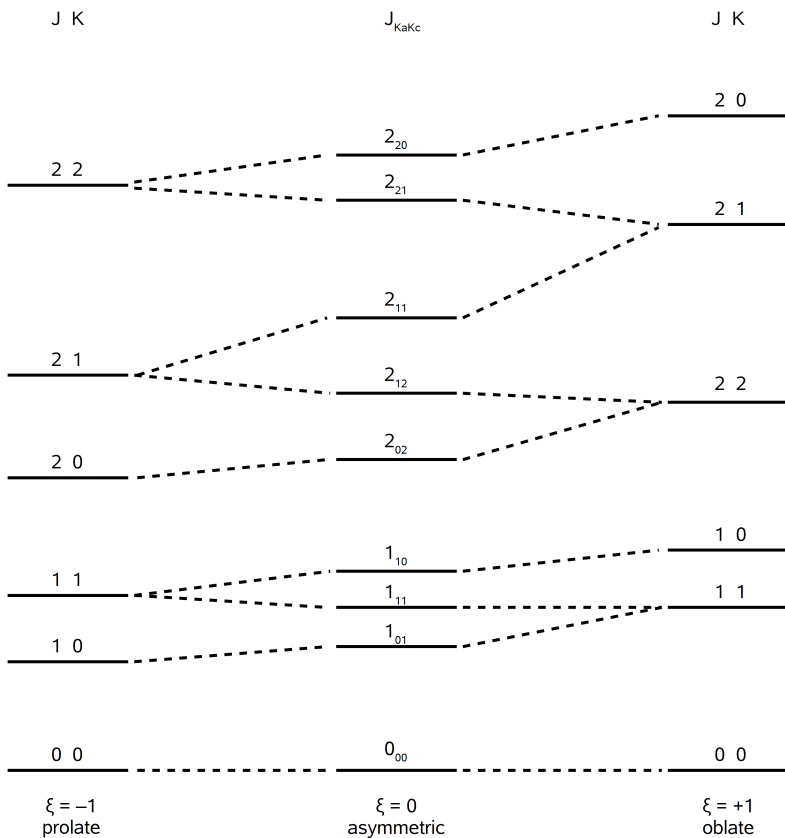


Figure 2.1: Influence of rotational asymmetry on the general energy level scheme of a rigid, non-distorted molecule. For $\xi \neq \pm 1$, the degeneracies of the prolate and oblate limiting cases are lifted and K is not a good quantum number any more. Because the asymmetric-top energy levels interconnect the limiting-case levels seamlessly, their respective K values can be used as labels in the $J_{K_a K_c}$ notation. Image adapted from [30].

the fit of the torsional ground state of acetone-2-¹³C:

$$\mathcal{H}_{red}^{(A)} = \mathcal{H}_r + \sum_{\substack{n=4 \\ n \text{ even}}}^{10} \mathcal{H}_d^{(n)} \quad (2.11)$$

$$\mathcal{H}_r = \frac{1}{2}(A+B)P^2 + [C - \frac{1}{2}(A+B)]P_z^2 + \frac{1}{2}(A-B)(P_x^2 - P_y^2) \quad (2.12)$$

$$\begin{aligned} \mathcal{H}_d^{(4)} = & \Delta_J P^4 - \Delta_{JK} P^2 P_z^2 - \Delta_K P_z^4 - 2\delta_J P^2 (P_x^2 - P_y^2) \\ & - \delta_K [P_z^2 (P_x^2 - P_y^2) + (P_x^2 - P_y^2) P_z^2] \end{aligned} \quad (2.13)$$

$$\begin{aligned} \mathcal{H}_d^{(6)} = & \Phi_J P^6 + \Phi_{JK} P^4 P_z^2 + \Phi_{KJ} P^2 P_z^4 + \Phi_K P_z^6 \\ & + 2\phi_J P^4 (P_x^2 - P_y^2) + \phi_{JK} P^2 [P_z^2 (P_x^2 - P_y^2) + (P_x^2 - P_y^2) P_z^2] \\ & + \phi_K [P_z^4 (P_x^2 - P_y^2) + (P_x^2 - P_y^2) P_z^4] \end{aligned} \quad (2.14)$$

$$\begin{aligned} \mathcal{H}_d^{(8)} = & L_J P^8 + L_{JJK} P^6 P_z^2 + L_{JK} P^4 P_z^4 + L_{KKJ} P^2 P_z^6 + L_K P_z^8 \\ & + 2l_J P^6 (P_x^2 - P_y^2) + l_{JK} P^4 [P_z^2 (P_x^2 - P_y^2) + (P_x^2 - P_y^2) P_z^2] \\ & + l_{KJ} P^2 [P_z^4 (P_x^2 - P_y^2) + (P_x^2 - P_y^2) P_z^4] \\ & + l_K [P_z^6 (P_x^2 - P_y^2) + (P_x^2 - P_y^2) P_z^6] \end{aligned} \quad (2.15)$$

Note that A , B and C now are effective coefficients containing the respective rotational constant and further coefficients from transformed distortion terms of the same order. For nearly symmetric tops a different reduction of similar form (“ S reduction”) is found, where terms involving P_x or P_y are combined in the lowering / raising operators $P_+ = P_x + iP_y$ and $P_- = P_x - iP_y$.

2.3 General aspects of internal rotation

This section summarises the key points of Lin and Swalen’s fundamental review on internal rotation [59] as applicable for acetone. Besides its overall rotational and vibrational modes, each of the two methyl groups (to be more precisely, the hydrogens) of acetone may oscillate in a common movement. Said hydrogen atoms are light compared to the “backbone” carbon and oxygen atoms involved in the overall vibrational modes. Two consequences arise from this

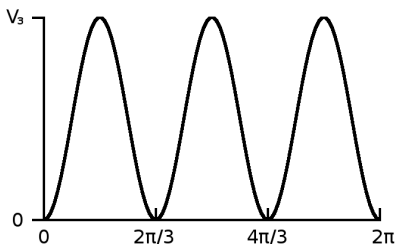


Figure 2.2: The sinusoidal torsional potential of an ideal three-fold internal rotor.

fact: First, the energies for torsional excitation already start from around 100 cm^{-1} , meaning that the lowest torsional excitations are always populated at room temperature. The second consequence is that the oscillatory amplitude of the hydrogen nuclei is so large that a significant exchange of energy with the molecule's overall rotation takes place and the coupling terms cannot be properly described by perturbation theory.

The oscillating protons of a methyl group form a system with three equivalent configurations. This is expressed by a potential which is threefold periodic with respect to the torsional angle τ . The physics governing the movement of a molecular structural subgroup, with a rotational degree of freedom about the axis defined by the bond between this group and the rest of the molecule (“the framework”), can be explained in a dedicated consideration of its sub-Hamiltonian H_I . Because the scope of this thesis only comprises methyl groups without deuteration, the discussion is restricted to the case that the internal rotor exhibits C_3 symmetry about its torsional axis. The three equivalent configurations of the rotating hydrogen atoms are reflected by a $2\pi/3$ -periodic potential,

$$V(\tau) = \sum_{k=0}^{\infty} a_k \cos 3k\tau \quad (2.16)$$

For an understanding of the general results, it is sufficient to assume that the second- and higher-order corrections to the sinusoidal potential can be neglected. If, furthermore, a_0 is chosen such that

$V(0) = 0$, one gets the approximate expression

$$V(\tau) \approx \frac{V_3}{2}(1 - \cos 3\tau) \quad (2.17)$$

displayed in Fig. 2.2. Denoting the moments of inertia of the internal rotor and the rigid frame as I_α and I_β , respectively, one can define a reduced moment of inertia

$$I_r = \frac{I_\alpha I_\beta}{I_\alpha + I_\beta} \quad (2.18)$$

of the system with respect to the axis of internal rotation, and with a corresponding rotational constant $F = \hbar^2/2I_r$, set up the Schrödinger equation for the internal rotor:

$$-F \frac{d^2 U(\tau)}{d\tau^2} + \left[\frac{V_3}{2}(1 - \cos 3\tau) - E \right] U(\tau) = 0 \quad (2.19)$$

The solutions of this equation range between two limiting cases for the barrier height V_3 : the vanishing potential $V_3 \rightarrow 0$ and the hard-wall potential $V_3 \rightarrow \infty$. For $V_3 \rightarrow 0$, eq. (2.19) takes the form

$$-\frac{d^2 U(\tau)}{d\tau^2} + \frac{E}{F} U(\tau) = 0 \quad (2.20)$$

which is readily solved by the free-rotor functions

$$|m\rangle = \frac{\pi}{\sqrt{2}} e^{im\tau} \quad (2.21)$$

and yields the energy levels

$$E = Fm^2 \quad (2.22)$$

Quantisation originates from the requirement that the solutions must be periodic under a full rotation, i.e., the boundary condition $U(\tau) = U(\tau + 2\pi)$ can only be fulfilled if $m \in \mathbb{Z}$. Particularly, m may have a positive or negative sign, which means that all free-rotor levels are doubly degenerate because the rotor is able to turn clockwise or counterclockwise. On the contrary, the presence of a high barrier $V_3 \rightarrow \infty$ turns the system into an oscillator. This is seen if the potential is expanded into powers of τ ,

$$\cos 3\tau = 1 - \frac{9}{2}\tau^2 + \mathcal{O}(\tau^4) \quad (2.23)$$

giving a harmonic oscillator for small values of τ ,

$$\frac{d^2U(\tau)}{d\tau^2} + \frac{1}{F}(E - \frac{9}{4}V_3\tau^2)U(\tau) = 0 \quad (2.24)$$

with the energies

$$E = 3\sqrt{V_3F}(v + \frac{1}{2}), v \in \mathbb{N}_0 \quad (2.25)$$

The equidistant levels are now threefold degenerate because the oscillation may likewise take place in each of the three potential wells. Now the dynamics of the real internal rotor with a finite barrier height become obvious: while, especially for the lowest states, a free rotation is hindered by the barrier, the system may still tunnel between the potential wells. For a mathematical description the torsional equation (2.19) is rescaled into Mathieu's equation:

$$\frac{d^2M(x)}{dx^2} + (b - s \cos^2 x)M(x) = 0 \quad (2.26)$$

where $3\tau + \pi = 2x$, $V_3 = \frac{9}{4}Fs$, and $E = \frac{9}{4}Fb$ have been inserted. The boundary condition for the Mathieu functions is now $M(x) = M(x + 3\pi)$, and it is fulfilled by two different types of solutions: A set of functions with period π belonging to nondegenerate eigenvalues $b_{v,0}$, and another one with period 3π whose eigenvalues $b_{v,\pm 1}$ are doubly degenerate. The second label, the symmetry number $\sigma = 0, \pm 1$, is used to differ between the three solutions pertaining to one harmonic oscillator label v , which is the same for two subsequent degenerate and nondegenerate eigenvalues (see Fig. 2.3). The symmetry labels shown in the Figure correspond to the symmetry species under the rotations of the C_3 group (see Table A.3). It is seen that the finite-barrier case can be regarded as a splitting of the harmonic oscillator levels, which increases as the barrier height is decreased. The double degeneracy of the free-rotor levels is maintained from a convergence of two A levels if m is a multiple of three, and from one of the E levels otherwise.

2.4 The ERHAM model

For a molecule like acetone with two internal rotors, the periodic potential shown in Fig. 2.2 is superposed with itself in a second dimension, resulting in an "egg-crate"-like potential energy surface. Due to

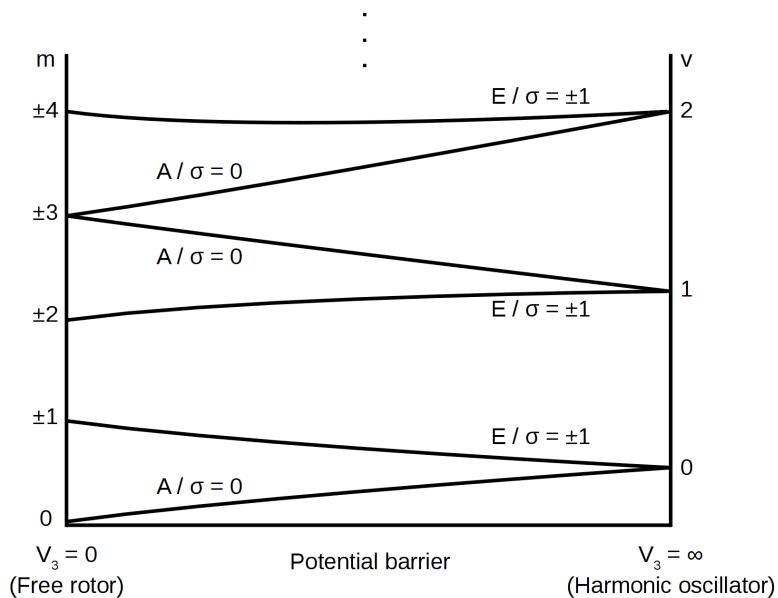


Figure 2.3: Schematic behaviour of the energy levels between the extreme cases of free rotation and an infinitely high harmonic oscillator. Image adapted from [30].

the strong coupling of internal and overall rotation, actually solving the full rotational-torsional Hamiltonian with all internal coordinates and the potential would be computationally too demanding to perform a realistic workflow of subsequent assigning and fitting. Instead, the periodicity of the potential can be inherited to all basis functions, matrix elements and energy levels by Fourier expansion. A skilful choice of basis is necessary to simplify the terms as far as possible, and the remaining free parameters split into four groups:

- Those of the reduced Watson Hamiltonian for a rigid⁵ asymmetric rotor with centrifugal distortion,
- the coefficients of the Fourier expansion of the internal energy levels (i.e., the eigenfunctions of the Hamiltonian \mathcal{H}_I describing the internal rotation),
- the so-called tunneling parameters describing integrals over two functions of the basis functions in Fourier space,
- and a few geometrical parameters describing the length ρ_k and relative orientation of the vectors $(\rho_0)_k$ (defined below), which are needed for a simplification in addition to the mentioned choice of basis.

The following sections give a detailed summary of this theory as it is published in [32, 35].

Structure of a Hamiltonian involving internal rotation

The general Hamiltonian of a molecule with internal rotation can be represented in two different ways:

$$\mathcal{H} = \mathcal{H}_R + \mathcal{H}_{RI} + \mathcal{H}_I \quad (2.27a)$$

$$= \sum_l R_l T_l \quad (2.27b)$$

⁵“Rigid” here denotes a molecule without internal rotation, whereas centrifugal distortion is permissible with no restriction. In contrast, an imaginary molecule without centrifugal distortion is said to be in its equilibrium configuration.

The sub-Hamiltonians in eqn. (2.27a) describe (from left to right) the pure terms for overall rotation, the interaction products between overall and internal rotation, and the terms involving only the momenta of internal motion. On the other hand, eq. (2.27b) states that every term whatsoever must be a product of operators containing some power of overall (R_l) and internal (T_l) momenta, which will be useful for more detailed examinations. The generalised index l denotes an expansion in an appropriate representation; see the examples given in Section 2.4.1. One may notice further that in a field-free experiment there is no potential in addition to the internal potential $V(\tau_1, \tau_2)$ described above.

Apart from that, \mathcal{H} is identical to the kinetic energy, which is most easily expressed in terms of the overall angular velocity $\boldsymbol{\omega} = (\omega_x, \omega_y, \omega_z)$ and the internal angular velocity $\dot{\boldsymbol{\tau}} = (\dot{\tau}_1, \dot{\tau}_2)$:

$$T = \frac{1}{2}(\boldsymbol{\omega}^t, \dot{\boldsymbol{\tau}}^t) \begin{pmatrix} \mathbf{I}_\omega & \mathbf{I}_{\omega\tau} \\ \mathbf{I}_{\omega\tau}^t & \mathbf{I}_\tau \end{pmatrix} \begin{pmatrix} \boldsymbol{\omega} \\ \dot{\boldsymbol{\tau}} \end{pmatrix} \quad (2.28)$$

It is yet more worthwhile for a quantum mechanical treatment to convert T into an expression in terms of the conjugate momenta $\mathbf{P} = -\frac{i}{\hbar}\nabla_\omega$ and $\mathbf{p} = -\frac{i}{\hbar}\nabla_{\dot{\boldsymbol{\tau}}}$:

$$T = (\mathbf{P}^t, \mathbf{p}^t) \begin{pmatrix} \mathbf{A} + \boldsymbol{\rho}\mathbf{F}\boldsymbol{\rho}^t & -\boldsymbol{\rho}\mathbf{F} \\ -\mathbf{F}\boldsymbol{\rho}^t & \mathbf{F} \end{pmatrix} \begin{pmatrix} \mathbf{P} \\ \mathbf{p} \end{pmatrix} \quad (2.29)$$

with the matrices

$$\mathbf{A} = \frac{\hbar^2}{2}\mathbf{I}_\omega^{-1}, \quad (2.30a)$$

$$\boldsymbol{\rho} = \mathbf{I}_\omega^{-1}\mathbf{I}_{\omega\tau}, \quad (2.30b)$$

$$\mathbf{F} = \frac{\hbar^2}{2}(\mathbf{I}_\tau - \boldsymbol{\rho}^t\mathbf{I}_\omega\boldsymbol{\rho})^{-1} \quad (2.30c)$$

$\boldsymbol{\rho}$ is a matrix which can be subdivided into a constant part $\boldsymbol{\rho}_0$ and a variable part $\Delta\boldsymbol{\rho}$. It depends only on the molecule's moments of inertia, thus on its geometry, and the column vectors of $\boldsymbol{\rho}_0 = [(\boldsymbol{\rho}_0)_1, (\boldsymbol{\rho}_0)_2]$ define two axes which are each physically meaningful for either of the two internal rotors and play a major role during the remaining discussion. With said definitions one obtains the final form of the three partial Hamiltonians:

$$\mathcal{H}_R = \mathbf{P}^t(\mathbf{A} + \Delta\boldsymbol{\rho}\mathbf{F}\Delta\boldsymbol{\rho}^t + \Delta\boldsymbol{\rho}\mathbf{F}\boldsymbol{\rho}_0^t + \boldsymbol{\rho}_0\mathbf{F}\Delta\boldsymbol{\rho}^t)\mathbf{P}, \quad (2.31a)$$

$$\mathcal{H}_{RI} = -(\mathbf{P}^t\Delta\boldsymbol{\rho}\mathbf{F}\mathbf{p} + \mathbf{p}^t\mathbf{F}\Delta\boldsymbol{\rho}^t\mathbf{P}), \quad (2.31b)$$

$$\mathcal{H}_I = (\mathbf{p}^t - \mathbf{P}^t\boldsymbol{\rho}_0)\mathbf{F}(\mathbf{p} - \boldsymbol{\rho}_0^t\mathbf{P}) + V. \quad (2.31c)$$

The internal Hamiltonian H_I

A straightforward approach to obtain a usable model without the need to actually solve the Schrödinger equation is to assume the existence of solutions which are products of free rigid-top wavefunctions $|JKM\rangle$ describing the states of overall rotation and the unknown solutions of H_I describing those of internal rotation. The solutions of H_I can be constructed from free-rotor functions in the torsional coordinates of the k -th internal rotor:

$$|j_1\sigma_1j_2\sigma_2\rangle = |j_1\sigma_1\rangle|j_2\sigma_2\rangle, \text{ with} \quad (2.32)$$

$$|j_k\sigma_k\rangle = \frac{1}{\sqrt{2\pi}} e^{i(n_k j_k + \sigma_k)\tau_k} \quad (2.33)$$

Note that the free-rotor functions contain a phase shift in form of the so-called symmetry numbers σ_k . Before constructing the eigenfunctions of H_I , it is highly useful to simplify its matrix elements in this basis in order to remove their explicit dependency on the overall angular momentum \mathbf{P} . Starting from the basis

$$|JKMj_1\sigma_1j_2\sigma_2\rangle = |JKM\rangle|j_1\sigma_1j_2\sigma_2\rangle \quad (2.34)$$

the functions $|JKM\rangle$ can be rotated into a basis $|JK_kM\rangle$, where K_k denotes the projection of K on the new z_k axis defined by $(\rho_0)_k$. The matrix elements are then rewritten as

$$\begin{aligned} & \langle JK'Mj'_1\sigma'_1j'_2\sigma'_2|\mathcal{H}_I|JKMj_1\sigma_1j_2\sigma_2\rangle \\ &= \sum_{K_1K_2} Y_{K'K}(K_1, K_2) \langle j'_1\sigma'_1j'_2\sigma'_2|\mathcal{H}_I(K_1, K_2)|j_1\sigma_1j_2\sigma_2\rangle \end{aligned} \quad (2.35)$$

with a projection term

$$\begin{aligned} Y_{K'K}(K_1, K_2) &= \frac{1}{2} (\langle JK'M|JK_1M\rangle \langle JK_1M|JK_2M\rangle \langle JK_2M|JKM\rangle \\ &+ \langle JK'M|JK_2M\rangle \langle JK_2M|JK_1M\rangle \langle JK_1M|JKM\rangle) \end{aligned} \quad (2.36)$$

tracking the effect of the basis rotation, and the matrix elements

$$\begin{aligned} & \langle j'_1\sigma'_1j'_2\sigma'_2|\mathcal{H}_I(K_1, K_2)|j_1\sigma_1j_2\sigma_2\rangle \\ &= \sum_{k=1}^2 \sum_{l=1}^2 (n_k j'_k + \sigma_k - \rho_k K_k) F_{j'_1-j_1, j'_2-j_2}^{(kl)} (n_l j_l + \sigma_l - \rho_l K_l) \\ &+ V_{j'_1-j_1, j'_2-j_2} \end{aligned} \quad (2.37)$$

in the desired form containing no further differential operators and vector products. Note that only those matrix elements with identical $\sigma_{k/l}$ are displayed because the symmetry numbers are conserved. This becomes obvious by noting that, just like the potential, the $F^{(kl)}$ are periodic functions,

$$F^{(kl)}(\tau_1, \tau_2) = \sum_{j_1 j_2} F_{j_1, j_2}^{(kl)} e^{i(n_1 j_1 \tau_1 + n_2 j_2 \tau_2)} \quad (2.38)$$

and hence all matrix elements off-diagonal in the symmetry numbers vanish due to orthogonality of the free-rotor functions.

The eigenvectors $U_{j_1 j_2 \nu \sigma_1 \sigma_2}^{(K_1, K_2)}$ of \mathcal{H}_I in a complex standard space are obtained by diagonalisation,

$$\mathcal{H}_I(K_1, K_2) U_{j_1 j_2 \nu \sigma_1 \sigma_2}^{(K_1, K_2)} = E_{\nu \sigma_1 \sigma_2}^{(K_1, K_2)} U_{j_1 j_2 \nu \sigma_1 \sigma_2}^{(K_1, K_2)} \quad (2.39)$$

and can be used to construct the assumed solutions to the Schrödinger equation for an internal excitation ν ,

$$|\nu \sigma_1(K_1) \sigma_2(K_2)\rangle = \sum_{j_1 j_2} U_{j_1 j_2 \nu \sigma_1 \sigma_2}^{(K_1, K_2)} |j_1 \sigma_1 j_2 \sigma_2\rangle \quad (2.40)$$

which in turn are vectors in a Hilbert space. Inserting this ansatz into the Schrödinger equation and multiplying both sides by $\langle j'_1 \sigma_1 j'_2 \sigma_2 |$ yields

$$\sum_{j_1 j_2} \langle j'_1 \sigma_1 j'_2 \sigma_2 | \mathcal{H}_I(K_1, K_2) | j_1 \sigma_1 j_2 \sigma_2 \rangle U_{j_1 j_2 \nu \sigma_1 \sigma_2}^{(K_1, K_2)} = E_{\nu \sigma_1 \sigma_2}^{(K_1, K_2)} U_{j'_1 j'_2 \nu \sigma_1 \sigma_2}^{(K_1, K_2)} \quad (2.41)$$

This equation can be used together with eq. (2.37), as well as periodicity and other basic arguments not shown here in detail, to deduce further relationships which enable Fourier expansion of the eigenquantities, which is the central step towards the effective Hamiltonian, and provide deeper insights into the nature of the results.

Fourier transformation

The eigenvalues, -vectors and -functions of \mathcal{H}_I are periodic functions of the torsional angles. For example, the corresponding relationship for the eigenvalues is

$$E_{\nu \sigma_1 \sigma_2}^{(K_1, K_2)} = E_{\nu, \sigma_1 + \lambda_1 n_1, \sigma_2 + \lambda_2 n_2}^{(K_1, K_2)}, \lambda_{1,2} \in \mathbb{Z} \quad (2.42)$$

It is therefore possible to write the internal rotor energies and eigenfunctions as Fourier series:

$$E_{\nu\sigma_1\sigma_2}^{(K_1,K_2)} = \sum_{q_1=0}^{N_1-1} \sum_{q_2=0}^{N_2-1} e^{2\pi i(q_1\sigma_1/n_1+q_2\sigma_2/n_2)} \epsilon_{\nu q_1 q_2}^{(K_1,K_2)} \quad (2.43)$$

These expressions introduce various new symbols. While real numbers can be used as coefficients in the energy series, the expansion of the eigenfunctions results in a new set of complex functions $\vartheta_{\nu q_1 q_2}^{(K_1,K_2)}(\tau_1, \tau_2)$ which are called localised functions. Their name was coined from the observation that, if the torsional energies $E_{\nu\sigma_1\sigma_2}^{(K_1,K_2)}$ for the considered state ν lie sufficiently deep below the potential barrier, their probability density is centered in one of the minima of the potential function V^6 . The conjugate indices of the symmetry numbers, q_k , can be regarded as a numbering scheme for the potential wells as they determine the well where the respective function is localised. The finite upper bounds of summation needed for numerical evaluation are defined by $N_k = m_k n_k$, with m_k being a large integer chosen such that the occurrence of the real numbers ρ_k in the Fourier terms (cf. the extended formulas below) does not (at least up to a good approximation) affect the periodicity of the expanded quantity.

It has been found in accordance with earlier results reported for phenomenological Hamiltonians of molecules with a single internal rotor [31] that the quantities given above also depend periodically on the projections K_k of the overall angular momentum on the ρ axes. With the abbreviations $\epsilon_{\nu q_1 q_2} \equiv \epsilon_{\nu q_1 q_2}^{(0,0)}$ and $\vartheta_{\nu q_1 q_2} \equiv \vartheta_{\nu q_1 q_2}^{(0,0)}$ the full periodicity relations can be written as

$$E_{\nu\sigma_1\sigma_2}^{(K_1,K_2)} = \sum_{q_1=0}^{N_1-1} \sum_{q_2=0}^{N_2-1} e^{2\pi i(q_1(\sigma_1-\rho_1 K_1)/n_1+q_2(\sigma_2-\rho_2 K_2)/n_2)} \epsilon_{\nu q_1 q_2} \quad (2.44a)$$

$$\vartheta_{\nu q_1 q_2}^{(K_1,K_2)}(\tau_1, \tau_2) = \vartheta_{\nu 00} \left(\tau_1 - \frac{2\pi q_1}{n_1}, \tau_2 - \frac{2\pi q_1}{n_1} \right) \cdot e^{i(\rho_1 K_1(\tau_1-2\pi q_1/n_1)+\rho_2 K_2(\tau_2-2\pi q_2/n_2))} \quad (2.44b)$$

These expressions show that the K dependence appears only in the exponential factors and that the energy Fourier coefficients

⁶For an appropriate choice of a complex phase factor $\varphi_{\sigma_1\sigma_2}$ defined in [32].

and localised functions can be traced back to quantities which are independent of K . Furthermore, any imaginary part of the localised functions must come from the exponential factors, as $\vartheta_{\nu q_1 q_2}^{(0,0)}$ is real. The role of q enabling to select a particular potential well is seen from eq. (2.44b), too.

The matrix elements of an operator $t(\tau_1, \tau_2)$, which shall be independent of the internal angular momenta p_1 and p_2 , in the basis of eigenfunctions of \mathcal{H}_I in Fourier representation is therefore:

$$\begin{aligned}
& \langle \nu' \sigma_1(K'_1) \sigma_2(K'_2) | t(\tau_1, \tau_2) | \nu \sigma_1(K_1) \sigma_2(K_2) \rangle \\
&= \frac{1}{m_1 m_2} \sum_{q_1=0}^{N_1-1} \sum_{q_2=0}^{N_2-1} e^{2\pi i (q_1 \sigma_1 / n_1 + q_2 \sigma_2 / n_2)} \\
&\quad \cdot \int_{-m_1 \pi}^{m_1 \pi} \int_{-m_2 \pi}^{m_2 \pi} \vartheta_{\nu' 00}^{(K'_1, K'_2)*}(\tau_1, \tau_2) t(\tau_1, \tau_2) \vartheta_{\nu q_1 q_2}^{(K_1, K_2)}(\tau_1, \tau_2) d\tau_1 d\tau_2 \\
&= \sum_{q_1 q_2} e^{\pi i (q_1 (2\sigma_1 - \rho_1 (K_1 + K'_1)) / n_1 + q_2 (2\sigma_2 - \rho_2 (K_2 + K'_2)) / n_2)} T_{\nu' \nu q_1 q_2}^{(\kappa_1, \kappa_2)}
\end{aligned} \tag{2.45}$$

where, in (2.45), the explicit K dependence of the localised functions was inserted and $\kappa_i = K_i - K'_i$ was used. The Fourier coefficients

$$\begin{aligned}
T_{\nu' \nu q_1 q_2}^{(\kappa_1, \kappa_2)} &= \frac{1}{m_1 m_2} e^{-\pi i (\rho_1 q_1 \kappa_1 / n_1 + \rho_2 q_2 \kappa_2 / n_2)} \\
&\quad \cdot \int_{-m_1 \pi}^{m_1 \pi} \int_{-m_2 \pi}^{m_2 \pi} e^{i(\rho_1 \kappa_1 \tau_1 + \rho_2 \kappa_2 \tau_2)} \vartheta_{\nu' 00}(\tau_1, \tau_2) t(\tau_1, \tau_2) \vartheta_{\nu q_1 q_2}(\tau_1, \tau_2) d\tau_1 d\tau_2
\end{aligned} \tag{2.46}$$

can be interpreted as descriptions of t during a tunneling motion between the potential wells $(0,0)$ of torsional state ν' and (q_1, q_2) of state ν . For $t = \mathbf{1}$ one can further define

$$i_{\nu' \nu q_1 q_2}^{(\kappa_1, \kappa_2)} := e^{\pi i (\rho_1 q_1 \kappa_1 / n_1 + \rho_2 q_2 \kappa_2 / n_2)} T_{\nu' \nu q_1 q_2}^{(\kappa_1, \kappa_2)} [t(\tau_1, \tau_2) = \mathbf{1}] \tag{2.47}$$

which is useful for the Fourier transformations of scalar products shown below. If $K_1 = K_2$, they obey the orthogonality relation

$$i_{\nu' \nu q_1 q_2}^{(0,0)} = \delta_{\nu' \nu} \delta_{0 q_1} \delta_{0 q_2} \tag{2.48}$$

which derives from the general orthogonality relation

$$\begin{aligned}
& \frac{1}{m_1 m_2} \int_{-m_1 \pi}^{m_1 \pi} \int_{-m_2 \pi}^{m_2 \pi} \vartheta_{\nu' q'_1 q'_2}^{(K_1, K_2)*}(\tau_1, \tau_2) \vartheta_{\nu q_1 q_2}^{(K_1, K_2)}(\tau_1, \tau_2) d\tau_1 d\tau_2 \\
&= \delta_{\nu' \nu} \delta_{q'_1 q_1} \delta_{q'_2 q_2} \\
\stackrel{q'_1=0}{\stackrel{q'_2=0}{\implies}} & \frac{1}{m_1 m_2} \iint e^{-2\pi i \left(\frac{\rho_1 K_1 q_1}{n_1} + \frac{\rho_2 K_2 q_2}{n_2} \right)} \vartheta_{\nu' 0 0}(\tau_1, \tau_2) \vartheta_{\nu q_1 q_2}(\tau_1, \tau_2) d\tau_{1,2} \\
&= \delta_{\nu' \nu} \delta_{0 q_1} \delta_{0 q_2} \tag{2.49}
\end{aligned}$$

It has been found that the integrals $i_{\nu' \nu q_1 q_2}^{(\kappa_1, \kappa_2)}$ are still approximately orthogonal for tunneling states with different K :

$$i_{\nu' \nu q_1 q_2}^{(\kappa_1, \kappa_2)} \approx \delta_{\nu' \nu} \delta_{0 q_1} \delta_{0 q_2}, \quad \kappa_{1,2} \neq 0. \tag{2.50}$$

A comparison of $i_{\nu' \nu q_1 q_2}^{(\kappa_1, \kappa_2)}$ with the orthogonality relation for the localised functions for $q'_1 = 0$ and $q'_2 = 0$ shows that, in the latter, the constant phase factor in (2.49) is replaced by a variable one, giving different weights and signs to the functions in certain regions of the integration domain. The approximate orthogonality thus being not self-evident, Groner states that it is usually fulfilled in a very good approximation [32, 35]. A possible interpretation of these usual conditions is that, for a given system, disadvantageous combinations of $\nu, \nu', \rho_k, K_k, m_k,$ and q_k may exist where the integrals do not vanish as expected, and further contributions to torsional energy may be mistakenly neglected by an algorithm which assumes orthogonality.

Transformed matrix elements of the rotational-torsional Hamiltonian

All sub-Hamiltonians can now be written in the basis

$$|JKM\nu\sigma_1\sigma_2\rangle = |JKM\rangle |\nu\sigma_1(K)\sigma_2(sK)\rangle \tag{2.51}$$

which is an orthonormal subset of solutions for $\mathcal{H}_I(K, sK)$ of the complete set which one would obtain with eq. (2.40). The sign $s = \text{sign}(\rho_{z_1} \rho_{z_2})$ indicates whether the two ρ vectors are pointing

into the same half space with respect to the xy plane. In comparison to the projection K of the total angular momentum on the molecule-fixed z axis, the rho-axis projections K_k used so far are not feasible to serve as quantum numbers for the whole Hamiltonian. The eigenvalues of \mathcal{H}_I , however, are essential to turn the Hamiltonian into a phenomenological one by removing the express occurrence of the potential. As they can only be included from the general solutions for $\mathcal{H}_I(K_1, K_2)$, two more rotations are needed to arrive at a satisfactory expression for \mathcal{H}_I :

$$\begin{aligned}
& \langle \nu' \sigma_1(K') \sigma_2(sK') | \mathcal{H}_I(K_1, K_2) | \nu \sigma_1(K) \sigma_2(sK) \rangle \\
&= \sum_{\nu''} \sum_{\nu'''} \langle \nu' \sigma_1(K') \sigma_2(sK') | \nu'' \sigma_1(K_1'') \sigma_2(K_2'') \rangle \\
&\quad \cdot \langle \nu'' \sigma_1(K_1'') \sigma_2(K_2'') | \mathcal{H}_I(K_1, K_2) | \nu''' \sigma_1(K_1''') \sigma_2(K_2''') \rangle \\
&\quad \cdot \langle \nu''' \sigma_1(K_1''') \sigma_2(K_2''') | \nu \sigma_1(K) \sigma_2(sK) \rangle \quad (2.52)
\end{aligned}$$

By identifying the arbitrary constants $K_k''' = K_k'' = K_k$, the central bracket takes the value $\delta_{\nu''\nu'''} E_{\nu''\sigma_1\sigma_2}^{(K_1, K_2)}$, and the matrix elements of \mathcal{H}_I can be rewritten in a form which (apart from $Y_{K'K}(K_1, K_2)$, where it is not necessary) fully supports Fourier expansion:

$$\begin{aligned}
\langle JK' M \nu' \sigma_1 \sigma_2 | \mathcal{H}_I | JKM \nu \sigma_1 \sigma_2 \rangle &= \sum_{K_1 K_2} Y_{K'K}(K_1, K_2) \\
&\quad \cdot \sum_{\nu''} \langle \nu' \sigma_1(K') \sigma_2(sK') | \nu'' \sigma_1(K_1) \sigma_2(K_2) \rangle E_{\nu''\sigma_1\sigma_2}^{(K_1, K_2)} \\
&\quad \cdot \langle \nu'' \sigma_1(K_1) \sigma_2(K_2) | \nu \sigma_1(K) \sigma_2(sK) \rangle \quad (2.53)
\end{aligned}$$

The scalar products can be transformed with eq. (2.47):

$$\begin{aligned}
& \langle \nu'' \sigma_1(K_1) \sigma_2(K_2) | \nu \sigma_1(K) \sigma_2(sK) \rangle \\
&= \sum_{q_1=0}^{N_1-1} \sum_{q_2=0}^{N_2-1} e^{2\pi i(q_1(\sigma_1 - \rho_1 K_1)/n_1 + q_2(\sigma_2 - \rho_2 K_2)/n_2)} i_{\nu\nu'', -q_1, -q_2}^{(K-K_1, sK-K_2)}, \quad (2.54)
\end{aligned}$$

in the basis as above, are finally written as:

$$\begin{aligned}
& \langle JK'M\nu'\sigma_1\sigma_2 | \mathcal{H}_{RI} | JK'M\nu\sigma_1\sigma_2 \rangle \\
&= \sum_{q_1=0}^{N_1-1} \sum_{q_2=0}^{N_2-1} e^{\pi i(q_1(2\sigma_1-\rho_1(K+K'))/n_1+q_2(2\sigma_2-s\rho_2(K+K'))/n_2)} \\
&\quad \cdot \sum_{\alpha} [-\langle JK'M | P_{\alpha} | JK'M \rangle \bar{T}_{\alpha}^{(\kappa,s\kappa)}{}_{\nu'\nu q_1 q_2} \\
&\quad\quad + \langle JK'M | P_z P_{\alpha} + P_{\alpha} P_z | JK'M \rangle T_{\alpha}^{(\kappa,s\kappa)}{}_{\nu'\nu q_1 q_2}] \quad (2.59)
\end{aligned}$$

Here, $T_{\alpha}^{(\kappa,s\kappa)}{}_{\nu'\nu q_1 q_2}$ is inferred from eq. (2.46) with $t(\tau_1, \tau_2) = \rho_1 t_{\alpha_1}(\tau_1, \tau_2) + s\rho_2 t_{\alpha_2}(\tau_1, \tau_2)$, and $\bar{T}_{\alpha}^{(\kappa,s\kappa)}{}_{\nu'\nu q_1 q_2}$ are similar tunneling parameters involving, and being the only such case in this treatment, odd orders of internal angular momentum:

$$\begin{aligned}
\bar{T}_{\alpha}^{(\kappa,s\kappa)}{}_{\nu'\nu q_1 q_2} &= \frac{1}{m_1 m_2} e^{-\pi i(q_1 \rho_1 \kappa_1 / n_1 + q_2 \rho_2 \kappa_2 / n_2)} \\
&\quad \cdot \int_{-m_1 \pi}^{m_1 \pi} \int_{-m_2 \pi}^{m_2 \pi} e^{i(\rho_1 \kappa_1 \tau_1 - \rho_2 \kappa_2 \tau_2)} \\
&\quad \cdot \sum_k t_{\alpha k}(\tau_1, \tau_2) [(p_k \vartheta_{\nu'00}(\tau_1, \tau_2)) \vartheta_{\nu q_1 q_2}(\tau_1, \tau_2) \\
&\quad\quad - \vartheta_{\nu'00}(\tau_1, \tau_2) (p_k \vartheta_{\nu q_1 q_2}(\tau_1, \tau_2))] d\tau_1 d\tau_2 \quad (2.60)
\end{aligned}$$

As tunneling parameters with even or odd order in p transform slightly differently under sign reversal of κ and q , a further sign $\omega = +1$ or -1 for even- or odd-order rotational operators, respectively, is introduced by writing

$$T_{\nu'\nu q_1 q_2}^{(\kappa_1, \kappa_2)} = \omega T_{\nu'\nu q_1 q_2}^{(-\kappa_1, -\kappa_2)*} = \omega T_{\nu\nu', -q_1, -q_2}^{(\kappa_1, \kappa_2)} = T_{\nu\nu', -q_1, -q_2}^{(-\kappa_1, -\kappa_2)*} \quad (2.61)$$

to avoid having to distinguish two classes of tunneling parameters.

All sub-Hamiltonians can now be combined in the generalised Fourier transformed matrix element of the full rotational-torsional

Hamiltonian:

$$\begin{aligned}
\langle JK'M\nu'\sigma_1\sigma_2|\mathcal{H}|JKM\nu\sigma_1\sigma_2\rangle &= \sum_l \langle JK'M|R_l|JKM\rangle \\
&\cdot \sum_{q_1=0}^{N_1-1} \sum_{q_2=0}^{N_2-1} e^{\pi i \left(\frac{q_1}{n_1} (2\sigma_1 - \rho_1(K+K')) + \frac{q_2}{n_2} (2\sigma_2 - s\rho_2(K+K')) \right)} T_l^{(\kappa, s\kappa)}{}_{\nu'\nu q_1 q_2} \\
&+ \delta_{\nu'\nu} \sum_{K_1, K_2} Y_{K'K}(K_1, K_2) \\
&\cdot \sum_{q_1=0}^{N_1-1} \sum_{q_2=0}^{N_2-1} e^{2\pi i (q_1(\sigma_1 - \rho_1 K_1)/n_1 + q_2(\sigma_2 - \rho_2 K_2)/n_2)} \epsilon_{\nu q_1 q_2}
\end{aligned} \tag{2.62}$$

The effective rotational Hamiltonian

The general matrix elements (2.62) include the energies for transitions between two different internal states ν and ν' . However, the lowest energies necessary to excite internal vibrations are large (typically some 100 cm^{-1}) compared to those of the rotational transitions of a single state ν . In a (sub-)millimetre spectrum (about $1 - 30 \text{ cm}^{-1}$), no transitions are thus observed between two torsional states, and the rotational spectrum can be calculated as a composition of separate spectra for each state. It is therefore adequate to use an effective rotational Hamiltonian where all elements off-diagonal in ν are neglected. Removing all “ ν ” subscripts and replacing $(\kappa, s\kappa)$ by (κ) , the matrix elements of the effective rotational Hamiltonian become

$$\begin{aligned}
\langle JK'M\nu'\sigma_1\sigma_2|\mathcal{H}|JKM\nu\sigma_1\sigma_2\rangle &= \sum_l \langle JK'M|R_l|JKM\rangle \\
&\cdot \sum_{q_1=0}^{N_1-1} \sum_{q_2=0}^{N_2-1} e^{\pi i \left(\frac{q_1}{n_1} (2\sigma_1 - \rho_1(K+K')) + \frac{q_2}{n_2} (2\sigma_2 - s\rho_2(K+K')) \right)} T_l^{(\kappa)}{}_{q_1 q_2} \\
&+ \sum_{K_1, K_2} Y_{K'K}(K_1, K_2) \sum_{q_1, q_2} e^{2\pi i \left(\frac{q_1}{n_1} (\sigma_1 - \rho_1 K_1) + \frac{q_2}{n_2} (\sigma_2 - \rho_2 K_2) \right)} \epsilon_{q_1 q_2}
\end{aligned} \tag{2.63}$$

Note that in this notation, which is used for consistency with the

literature, the symbols T and ϵ are still state-specific, although the subscripts ν and $\nu\nu$ have been omitted. The most compressed form of these matrix elements is

$$\begin{aligned} & \langle JK' M \nu' \sigma_1 \sigma_2 | \mathcal{H} | J K M \nu \sigma_1 \sigma_2 \rangle \\ &= \sum_{K_1, K_2} Y_{K'K}(K_1, K_2) \Sigma_0 + \sum_l \langle JK' M | R_l | J K M \rangle \Sigma_l. \end{aligned} \quad (2.64)$$

Expressions for the Fourier series Σ_0 and Σ_l depend on the equivalence of the internal rotors and the molecular symmetry and can be looked up from tables in [32]. Since they contain only equivalent methyl rotors, an identical expression for Σ_0 can be given for all acetone isotopologues treated here:

$$\Sigma_0 = \epsilon_{00} + 2 \sum_{q>0} \left[C'_{qq} \epsilon_{qq} + C'_{q-q} \epsilon_{q-q} + \sum_{q'=-q}^{q-1} (C'_{qq'} + C'_{q'q}) \epsilon_{qq'} \right], \quad (2.65)$$

where $q = q_1$ and $q' = q_2$ have been introduced for shortness. Σ_0 is a pure cosine expansion, which is seen from the definition

$$C'_{qq'} = \cos(2\pi(q(\sigma_1 - \rho K_1) + q'(\sigma_2 - \rho K_2))/n). \quad (2.66)$$

Σ_l , on the other hand, exhibits a more complex structure. It is a Fourier series structurally similar to Σ_0 , with the $\epsilon_{qq'}$ coefficients replaced by the tunneling parameters $T_l^{(\kappa)}{}_{qq'}$ and structurally refined sine and cosine expressions instead of the $C'_{qq'}$ above, but different subseries being enabled depending on details of point group symmetry, the orientation of the reference axes (s value, eq. (2.51)) and the ω values pertaining to the particular operators within $T_l^{(\kappa)}{}_{qq'}$. Furthermore, the real and imaginary parts of the tunneling parameters must be treated separately. The interested reader is referred to the original publication [32] if full comprehension is needed.

2.4.1 Nomenclature of the tunneling parameters

There are two equivalent ways to label the tunneling parameters:

- Watson-type parameter labeling: $[t]_{qq'}$, where the product operator t is represented by the label for its respective coefficient. The pair Δ_{JK} (from eq. (2.13)) and $[\Delta_{JK}]_{10}$ is an example.

- Cylindrical tensor form: $[B_{kpr}]_{qq'}$, from the definition given in [32]:

$$H_R = \sum_{kpr} \frac{1}{2(1 + \delta_{0r})} [J^k J_z^p, J_+^r + J_-^r]_+ B_{kpr} \quad (2.67)$$

While the usage of Watson-type labels is more convenient for tunneling parameters of centrifugal terms, the cylindrical tensor form is more general, because it is also defined for all product operators which are not included in one of the Watson reductions. It will be used here whenever no other label could be found for operators of a particular combination of powers. The r power used in the cylindrical tensor notation is identical to the absolute K difference, $r = |\kappa|$, from eq. (2.57). Furthermore, the order of a tunneling parameter $\eta := k + p + r$ will be used.

In the numerical fit, the right choice of tunneling parameters to describe the J or K dependence of the torsional splittings can be narrowed down to enabling parameters which are adjacent (as defined in Section 4.2) to a given parameter set with respect to their indices k and p .

2.4.2 Numerical implementation

A FORTRAN programme “ERHAM” capable of fitting the Effective Rotational Hamiltonian to a set of assigned transitions and predicting the spectrum based on the determined parameters has been developed by P. Groner and is publicly available [47]. It can be initialised with appropriate settings to reflect given molecular properties like point group symmetry, which affects the appearance of Σ_0 and Σ_l in (2.64).

ERHAM uses parameter start values and assigned transition frequencies from a user generated input file to set up the Hamiltonian in form of $(2J + 1) \times (2J + 1)$ block matrices for each torsional state ν and each combination of symmetry numbers $\sigma_1 \sigma_2$ such that all states $|JKM\nu\sigma_1\sigma_2\rangle$ are represented. Eigenvalues and -vectors of these are determined with standard algebra algorithms (including Householder transformation to upper triangular form, root finding by bisection, and singular value decomposition). This per-state mathematics is embedded in a non-linear weighted least-square

routine, which fits the parameters to the data and is iterated a predetermined number of times. Every cycle ends with an output of the determined singular values and associated right singular vectors, the standard deviation of the least-square fit, a list of the current parameter values, their uncertainties and changes, and, importantly, a correlation matrix of the parameters. The correlation score may take values between $-100\,000$ and $100\,000$, with these extreme values denoting fully linearly dependent parameters of opposite or same sign, respectively, and a value of 0 indicating two fully decoupled parameters. After the last cycle, several geometrical and physical parameters of the molecule (including torsional energy differences) are derived and, optionally, a prediction of the spectrum is generated from the obtained parameters.

A major validation of the model is the rapid convergence of the Fourier series in q and q' for states well below the barrier, as it has been expected by Groner and proven by numerous earlier spectral fits performed with ERHAM. The analyses presented in Chapter 4 confirm this once more as they require no Fourier terms beyond the order $\zeta := |q| + |q'| = 2$. Besides v , q and q' , each parameter in the ERHAM user input takes four further identifiers to be fully defined: $\omega = \pm 1$ as defined in eq. (2.61) to denote angular momenta of even or odd order, and the powers k , p and r of angular momentum defined in Section 2.4.1.

By counting the unsplit distorted rotor energy levels in ascending order, ERHAM circumvents the problem of having to select a particular coordinate representation (Section 2.2), at the price that the pseudo-quantum numbers K_a and K_c need to be derived for physical interpretation. This leads to a common counting mistake which becomes apparent if the observed spectrum contains transitions between crossing energy levels (Fig. 2.4). Consequentially, transitions between rotational energy levels thus mislabeled in K appear to have wrong transition types. As the dipole moment of acetone coincides with the b axis, apparently forbidden a - and c -type transitions appear in the assignments and predictions (Fig. 2.7).

An enhanced version ERHAMZ developed and published by Z. Kisiel [47] was used at the beginning of the works described in Chapter 4. ERHAMZ generates additional output, most importantly a list of the fifty lines that were fit worst in the current cycle and two root-mean-square errors (weighted and unweighted) for the least-square

fit. When it turned out that the array dimensions originally provided by ERHAM were insufficient for the acetone-2-¹³C data set and the parameters needed to obtain a satisfactory fit, a new fork called ERHAMO with larger arrays was compiled by the author in order to continue the analysis.

2.5 Effects of symmetry

In many physical systems the number of possible solutions to the Schrödinger equation is restricted by the presence of symmetry. Mathematical transformations which do not change the Hamiltonian, the so-called symmetry operations, may yet impose a change on the symmetry of some wavefunctions which would violate physical laws like the spin-statistics theorem. Consequently, not all *a priori* possible states are realised by the system, and selection rules between states of certain symmetry arise. The states and / or energy levels are given symmetry labels accordingly. In spectroscopy, another consequence of symmetry is the distribution of intensities, which originates from differences in the number of spin states pertaining to a particular state and its symmetry labels.

Considerations of physical symmetry are inherently connected to group theory, as symmetry operations form a group by construction. The behaviour of the total wavefunction⁷

$$\psi_{tot} = \psi_{rve}\psi_{ns} \quad (2.68)$$

under the transformations of a symmetry group applicable to the molecule can strongly depend on the molecular state described by the rovibrational wavefunction ψ_{rve} and the nuclear spin state ψ_{ns} . The transformational behaviour of these functions, determined by finding the irreducible components of the reducible representation formed by the symmetry behaviour of the molecule's nuclear spins, is the starting point for an assessment of selection rules and the distribution of intensity between the torsional components of a rotational transition.

⁷The wavefunction describing the translational motion of the centre of mass is omitted here because translational symmetry / momentum conservation is taken as given.

2.5.1 Four group symmetry

There is a general symmetry of the rotational Hamiltonian leading to selection rules for the asymmetric-top states [30]. It is a direct consequence of energy and angular momentum conservation: The constance of angular momentum means that the points in angular momentum space reached by the P vector form a sphere:

$$P^2 = P_x^2 + P_y^2 + P_z^2 = \text{constant} \quad (2.69)$$

On the other hand, the kinetic energy is constant if no external forces are applied:

$$E_r = \frac{1}{2} \left(\frac{P_x^2}{I_x} + \frac{P_y^2}{I_y} + \frac{P_z^2}{I_z} \right) = \text{constant} \quad (2.70)$$

which further restricts the angular momentum components onto an ellipsoid. As a consequence, the angular momentum vector may only point to one of the curves along the intersections of the angular momentum sphere and the energy ellipsoid. Regardless of the detailed shape of these surfaces, they are always symmetric under a C_2 rotation about the x , y , and z axes each. These operations form the Four group $V(a, b, c)$, which is isomorphic to the group C_{2v} ⁸. Under the rotations of the Four group, the angular momentum components transform according to one of the symmetry species (see the character table in Appendix A):

$$\begin{aligned} E &: P_a \rightarrow P_a, P_b \rightarrow P_b, P_c \rightarrow P_c \\ C_2(a) &: P_a \rightarrow P_a, P_b \rightarrow -P_b, P_c \rightarrow -P_c \\ C_2(b) &: P_a \rightarrow -P_a, P_b \rightarrow P_b, P_c \rightarrow -P_c \\ C_2(c) &: P_a \rightarrow -P_a, P_b \rightarrow -P_b, P_c \rightarrow P_c \end{aligned}$$

The effect of the Four group rotations on the asymmetric-top wavefunctions is expressed by the projection labels K_a and K_c . This is most easily seen by comparison to a symmetric-top wavefunction: A prolate molecule rotated by π about its symmetry axis a will change the angle ϕ to $\phi + \pi$, but will not change the other Eulerian

⁸The C_{2v} symmetry of the rotational Hamiltonian is of a general nature and not related to the C_{2v} symmetry of the equilibrium structure of acetone.

angles. The rotational wavefunction $|JKM\rangle$ depends on ϕ like $e^{iK\phi}$, so one gets the K dependence

$$C_2(a) : |JKM\rangle \rightarrow e^{iK\pi} |JKM\rangle = (-1)^K |JKM\rangle. \quad (2.71)$$

For an asymmetric top the effect on the angles is more complicated, but because a change in moments of inertia (i.e., ξ) cannot affect the symmetry of a rotational state, the transformational behaviour of the limiting prolate and oblate cases, expressed by the respective quantum number K , is inherited to the asymmetric-top wavefunctions with respect to the labels K_a and K_c . The symmetry of any state $J_{K_a K_c}$ is thus found to depend on K_a and K_c being even (e) or odd (o), and the corresponding symmetry classes according to the character table (see Table A.4) are A for $(K_a K_c) = (ee)$, B_a for (eo) , B_b for (oo) , and B_c for (oe) . Table A.4 also contains the separate e/o selection rules between these labels existing for the three asymmetric-top transition types (see [30] for a detailed explanation), and the equivalent symmetry classes of the isomorphic C_{2v} group as well.

2.5.2 Permutational symmetry groups

The formalism on permutational symmetry presented here goes back to the detailed treatment in the books by Bunker and Jensen [9, 10]. Symmetry operations of a molecule – regardless of being a rotation, reflection or inversion – can be represented by isomorphic permutations of identical nuclei. To handle the individual case, one must use the group containing the set of operations which correctly describes the physical aspect under consideration as well as the degree of experimental detail. Besides the Four group mentioned in Section 2.5.1, the following symmetry groups are used in rotational spectroscopy:

The point group. In their equilibrium configuration, the nuclei of many molecules are arranged in a symmetric manner. The operations transforming this structure into itself form the point group of a molecule.

The CNPI group. The largest permutation group of a molecule, containing all possible exchanges of identical nuclei even if they are not realised in the experiment (e.g. bond breaking of

stable molecules), is called the Complete Nuclear Permutation Inversion group.

The MS group. The set of feasible operations⁹ forms the Molecular Symmetry group, a subgroup of the CNPI group.

A symmetry analysis of the rotational states is composed of two major steps: First, the spin-statistical weight g_{ns} is determined for each rovibrational symmetry species Γ_{rve} of the MS group. For this purpose, the characters of the reducible representation Γ_{ns}^{red} formed by the spins under the symmetry transformations of the MS group are calculated by

$$\chi_{ns}^{tot}[P] = \prod_a (2I_a + 1). \quad (2.72)$$

The index a denotes sets of identical nuclei permuted by the operation P , where each nucleus not permuted by P is counted as a set of its own containing one element. Said reducible representation can be decomposed into irreducible representations Γ_{ns}^i according to the general rule

$$\Gamma^{red} = \bigoplus_i a_i \Gamma^i \quad (2.73)$$

with the coefficients

$$a_i = \frac{1}{h} \sum_R \chi^{\Gamma^{red}}[R] \chi^{\Gamma^i}[R]^* \quad (2.74)$$

This sum is taken over all symmetry transformations R and h is the number of elements in the group (e.g. $h = 36$ for G_{36}). Furthermore, the total wavefunction is required to obey the Pauli principle (e.g. ψ_{tot} must be symmetric under an even permutation of H nuclei). The allowed rovibrational symmetry species can then be concluded from the direct product table, using

$$\Gamma_{tot} \stackrel{!}{\subset} \Gamma_{rve} \otimes \Gamma_{ns}. \quad (2.75)$$

Finally, the nuclear spin weights of the rovibrational symmetry species are obtained by adding the coefficients a_i for all allowed combinations.

⁹Observable operations actually taking place during the measurement.

In the second step, these spin weights must be assigned to the torsional components of the rotational transitions. First, selection rules for the rovibrational species are established by exploiting the vanishing-integral rule: The matrix element describing the dipole moment transition between two rovibrational states, $\int \psi_{rve}^{(f)*} \boldsymbol{\mu} \psi_{rve}^{(i)} d\tau$, will vanish unless the integrand contains the totally symmetric species:

$$\Gamma_{rve}^{(f)} \otimes \Gamma[\boldsymbol{\mu}] \otimes \Gamma_{rve}^{(i)} \supset A_1 \quad (2.76)$$

The symmetry species $\Gamma[\boldsymbol{\mu}]$ is found by testing its transformational behaviour with the character table. Once more, the product table shows the complementary rovibrational species needed to fulfill the requirement (2.76).

The rovibrational selection rules thus obtained can be connected to the torsional symmetry labels $\sigma_{1,2}$ with a correlation table which interprets internal rotation as an MS group operation. These tables could be found in the literature for the cases applying here. If the MS group contains overall C_2 rotations of the molecule, the e/o selection rules shown in Table A.4 apply in addition, and a correlation table between the MS group and the Four group must be created to connect the rovibrational selection rules to those of the Four group. This way, the weights g_{ns} can be distributed to all possible transitions, delivering the relative intensities of the torsional components.

2.5.3 Symmetry analysis of acetone- ^{12}C and $^{13}\text{C}_1$

Acetone- ^{12}C

Acetone's equilibrium structure has a C_2 axis coinciding with the CO bond and the intersection line of two perpendicular reflection planes. Its symmetry is therefore described by the group C_{2v} . The CNPI group contains $6! = 720$ permutations of hydrogen, $3! = 6$ permutations of carbon-12, and a factor of 2 to account for inversion, giving a total of 8640 elements. Out of these operations, however, only those describing an internal or overall rotation (or a combination of both) are feasible. They form the MS group G_{36} and are shown in its character table A.8.

The nuclear spins in acetone are $I = \frac{1}{2}$ for the six hydrogens, and $I = 0$ for the three carbons and the oxygen. Inserting into (2.72)

yields with the numbering scheme shown in Fig. 2.5 b):

$$\chi_{ns}^{tot}[E] = 2^6 \cdot 1^3 \cdot 1 = 64$$

$$\chi_{ns}^{tot}[(132)] = 2 \cdot 2^3 \cdot 1^3 \cdot 1 = 16$$

$$\chi_{ns}^{tot}[(23)(56)^*] = 2^2 \cdot 2^2 \cdot 1^3 \cdot 1 = 16$$

$$\chi_{ns}^{tot}[(123)(456)] = \chi_{ns}^{tot}[(123)(465)] = 2^2 \cdot 1^3 \cdot 1 = 4$$

$$\chi_{ns}^{tot}[(142635)(79)^*] = \chi_{ns}^{tot}[(142536)(79)] = 2 \cdot 1 \cdot 1 \cdot 1 = 2$$

$$\chi_{ns}^{tot}[(14)(26)(35)(79)^*] = \chi_{ns}^{tot}[(14)(25)(36)(79)^*] = 2^3 \cdot 1 \cdot 1 \cdot 1 = 8$$

The decomposition of Γ_{ns}^{red} into the irreducible representations of G_{36} is obtained from these characters by evaluation of eq. (2.74):

$$\Gamma_{ns}^{red} = 10A_1 \oplus 6A_4 \oplus 3E_1 \oplus E_2 \oplus 3E_3 \oplus E_4 \oplus 8G \quad (2.77)$$

The total wavefunction [eq. (2.68)] must be symmetric under a permutation of the carbon nuclei. It follows from the character and product tables that ψ_{tot} must have A_2 or A_4 symmetry. This is not further constrained by the requirement that ψ_{tot} be (anti)symmetric under even (odd) permutations of the hydrogen nuclei. Combinations fulfilling (2.75) according to the direct product table (Table A.8) are summarised in Table 2.1, together with the spin weights g_{ns} from eq. (2.77).

Table 2.1: Allowed symmetry combinations of the rovibrational and nuclear-spin wavefunctions for acetone, and their spin-statistical weights for acetone and acetone-2-¹³C.

Γ_{rve}	Γ_{ns}	Γ_{tot}	g_{ns} (¹² C)	g_{ns} (2- ¹³ C)
A_1	$-, 6A_4$	A_2, A_4	6	12
A_2	$10A_1, -$	A_2, A_4	10	20
A_3	$6A_4, -$	A_2, A_4	6	12
A_4	$-, 10A_1$	A_2, A_4	10	20
E_1	$3E_1, E_2$	A_2, A_4	4	8
E_2	$E_2, 3E_1$	A_2, A_4	4	8
E_3	E_4, E_4	A_2, A_4	2	4
E_4	$3E_3, 3E_3$	A_2, A_4	6	12
G	$8G, 8G$	A_2, A_4	16	32

The dipole vector $\boldsymbol{\mu}$ coincides with the b axis and therefore has A_3 symmetry. The vanishing-integral rule (2.76) shows that the representation of $\psi_{rve}^{(f)}\psi_{rve}^{(i)}$ must therefore contain A_3 . This is true for the eight selection rules summarised in Table 2.2. The respective rovibrational e/o selection rules and σ labels shown there, too, are identified using the correlation tables A.4 and A.10. The relative intensities given are the respective spin-statistical weights normalised to one.

Table 2.2: Relative intensities and rovibrational selection rules applicable to the torsional components of the rotational transitions of acetone- ^{12}C and - ^{13}C .

(σ_1, σ_2)	$K_a K_c :$ $ee \leftrightarrow oo$	$K_a K_c :$ $eo \leftrightarrow oe$
$(0, 0)$	3 $A_1 \leftrightarrow A_3$	5 $A_2 \leftrightarrow A_4$
$(\pm 1, 0),$ $(0, \pm 1)$	8 $G \leftrightarrow G$	8 $G \leftrightarrow G$
$(\pm 1, \pm 1)$	1 $E_3 \leftrightarrow E_3$	3 $E_4 \leftrightarrow E_4$
$(\pm 1, \mp 1)$	2 $E_1 \leftrightarrow E_2$	2 $E_1 \leftrightarrow E_2$

Acetone-2- ^{13}C

It is seen from Fig. 1.1 c) that an isotopic substitution at position 8 does not break the symmetry of the main isotopologue, so the point and MS group of acetone-2- ^{13}C are C_{2v} and G_{36} , respectively, as well. It can thus be treated identically, the only difference in consideration being that the spin 0 of the central C atom is replaced by spin $\frac{1}{2}$. This leads to an additional factor 2 for all characters, coefficients and statistical weights associated with the nuclear spins, but leaves the final relative intensities unchanged because all sums and label assignments are identical. For completeness, the spin weights for acetone-2- ^{13}C are given in Table 2.1. Relative intensities observed for two rotational transitions are shown in Fig. 2.6. Intensities determined by the SVIEW_L peak finder are 403 (0,0) : 672 (0,1) : 180

(1,2) : 252 (1,1) for the $eo \leftarrow oe$ case and 1052 (0,0) : 2642 (0,1) : 341 (1,1) : 774 (1,2) for the $oo \leftarrow ee$ case, confirming the calculation within experimental uncertainty.

Acetone-1- ^{13}C

The asymmetric $^{13}\text{C}_1$ isotopologue of acetone is substituted at one of the equivalent positions 7 or 9 indicated in Fig. 2.5 b). As the rotational-reflectional symmetry of the other two isotopologues is broken, the remaining reflectional symmetry with respect to the C-C-C plane is described by the point group C_s (see Table A.2). This also impacts the MS group, which becomes G_{18} and is obtained from G_{36} by eliminating all classes containing C_2 rotation, represented by the permutation (79). Using the character table A.5 and the product table A.6, the procedure outlined above gives the following results:

$$\begin{aligned}\chi_{ns}^{tot}[E] &= 2^6 \cdot 2 \cdot 1^2 \cdot 1 = 128 \\ \chi_{ns}^{tot}[(123)] &= \chi_{ns}^{tot}[(456)] = 2 \cdot 2^3 \cdot 2 \cdot 1^2 \cdot 1 = 32 \\ \chi_{ns}^{tot}[(123)(456)] &= \chi_{ns}^{tot}[(123)(465)] = 2 \cdot 2 \cdot 2 \cdot 1^2 \cdot 1 = 8 \\ \chi_{ns}^{tot}[(23)(56)^*] &= 2^2 \cdot 2^2 \cdot 2 \cdot 1^2 \cdot 1 = 32 \\ \Gamma_{ns}^{red} &= 32A_1 \oplus 16E_1 \oplus 16E_2 \oplus 8E_3 \oplus 8E_4\end{aligned}\quad (2.78)$$

ψ_{tot} must be (anti-)symmetric under an even (odd) permutation of the H nuclei. While the odd permutations pose no restrictions on ψ_{tot} , the product table reveals that ψ_{tot} must have A_1 or A_2 symmetry due to the even permutations. Table 2.3 states the allowed combinations of symmetry species and their spin weights.

The vanishing-integral rule allows for all rovibrational transitions whose product representation contains the species $\Gamma[\boldsymbol{\mu}] = A_2$. Table 2.4 gives an overview of the resulting selection rules and relative intensities. Note that, unlike for the other two isotopologues, there is no distinction between $ee \leftrightarrow oo$ and $eo \leftrightarrow oe$, because C_2 is not a symmetry operation any more. Label assignments were taken from correlation table A.9.

2.6 General spectral features

A short explanation of the composition of the acetone spectrum shall be given here as a reference. The dipole moment of acetone has been

Table 2.3: Allowed symmetry combinations of the rovibrational and nuclear-spin wavefunctions, and their spin-statistical weights, for acetone-1-¹³C.

Γ_{rve}	Γ_{ns}	Γ_{tot}	g_{ns}
A_1	$32A_1, -$	A_1, A_2	32
A_2	$-, 32A_1$	A_1, A_2	32
E_1	$16E_1, 16E_1$	A_1, A_2	32
E_2	$16E_2, 16E_2$	A_1, A_2	32
E_3	$8E_3, 8E_3$	A_1, A_2	16
E_4	$8E_4, 8E_4$	A_1, A_2	16

Table 2.4: Relative intensities and rovibrational selection rules applicable to the torsional components of the rotational transitions of acetone-1-¹³C.

(σ_1, σ_2)	Relative intensity, Selection rule
$(0, 0)$	2 $A_1 \leftrightarrow A_2$
$(\pm 1, 0)$	2 $E_1 \leftrightarrow E_1$
$(0, \pm 1)$	2 $E_2 \leftrightarrow E_2$
$(\pm 1, \mp 1)$	1 $E_3 \leftrightarrow E_3$
$(\pm 1, \pm 1)$	1 $E_4 \leftrightarrow E_4$

measured as 2.89 D (see the discussion in Section 5.1.2) and is coinciding with the b axis. All observed transitions are therefore of the b type ($\Delta J = 0, \pm 1$; ΔK_a odd, ΔK_c odd). The change in dipole moment magnitude and orientation imposed by a single ¹³C substitution affects either only the absolute intensities (acetone-2-¹³C), or the resulting a and c components are too small to generate observable a - and c - type transitions to be discerned from the dense

background of low-intensity lines (acetone-1-¹³C). However, the predicted spectra contain mock *a*- and *c*-type transitions caused by the mislabeling effect explained in Section 2.4.2.

While the magnitude of the dipole moment directly influences the absolute intensities ($I \propto |\mu|^2$), the relative intensities of the rotational transitions of a particular transition type and torsional state follow the population differences introduced by the Boltzmann distribution.

The rotational spectra in this work have been recorded at room temperature, corresponding to a characteristic energy $kT \sim 204 \text{ cm}^{-1}$. This is well above the lowest torsional excitational energies ($v_{12} = 77.8 \text{ cm}^{-1}$, $v_{17} = 124.5 \text{ cm}^{-1}$). Thus, rotational spectra of torsionally excited states are visible besides the ground state spectrum. As the excitation energies are low enough to reach a significant population also in hot-core regions¹⁰, which are the only interstellar places where acetone has been found so far, a useful prediction of the spectrum for astronomical observations should contain at least the ground state and the first excited state.

As can be seen from Fig. 4.9 a), a remarkable feature in asymmetric-rotor spectra is the grouping of *R*-branch transitions of growing K_a in a rather small frequency range. The first line of a K_a series of a particular $J + 1 \leftarrow J$ transition is always the strong pair of degenerate transitions $K_a = 0 \leftrightarrow 1$. From one J to the next, these transitions lie about 10 GHz apart, establishing a convenient structure for the assignments. They are always predicted with a low uncertainty and have a characteristic intensity pattern (see Fig. 4.10), which facilitates the collection of lines from a K_a series because one can keep track of the shifts between the predicted and measured spectra from the start.

¹⁰e.g. in Orion-KL, where a peak temperature of 415 K / 289 cm^{-1} was reported in [22]

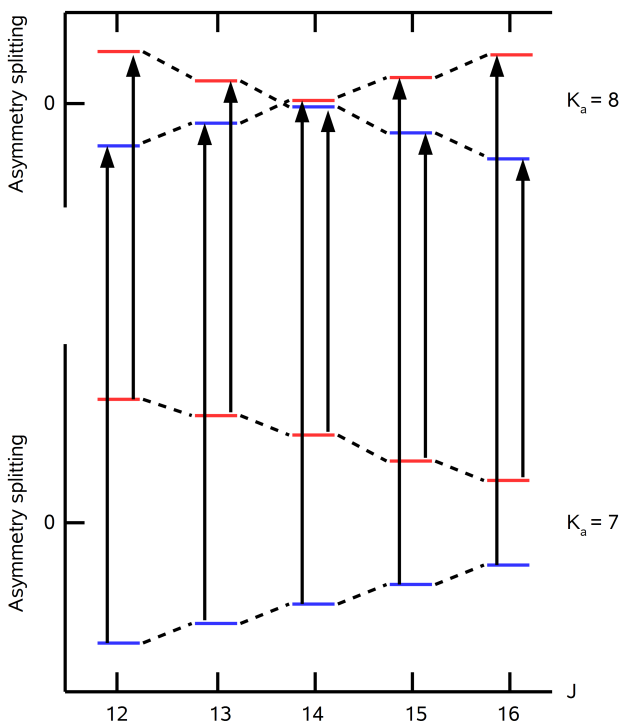


Figure 2.4: For a given J , ERHAM assumes that the energy levels are arranged in a stack with a steady counting scheme for K_a and K_c . In reality, this is not always the case, as the J dependence of asymmetry splittings may lead to crossings between the two asymmetry branches with $K_a + K_c = J$ (blue) and $K_a + K_c = J + 1$ (red) (cf. Fig. 4.6). While, physically, the transitions are connecting the same series of energy levels, the miscounting leads to predictions of seemingly forbidden transitions (which are important, though, to obtain correct predicted intensities; cf. the numerous a - and c -type lines in Fig. 2.7, where a pure b -type spectrum is supposed to be seen) and continues for all following values of J until a second energy level crossing occurs. Image adapted from [51].

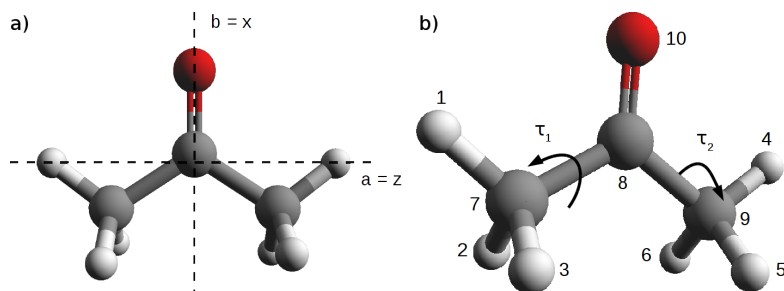


Figure 2.5: a) Assignment of the x, y, z and a, b, c axes systems. The c / y axis runs perpendicularly to the drawing plane and is not shown. C_{2v} symmetry is based on the x axis and the xz plane. The dipole moment vector μ coincides with the x axis. b) Atom positions and rotational directions for the angles τ_1 and τ_2 in acetone, as used in the symmetry considerations in this section. A carbon-13 atom is substituted at position 7 or 9 in acetone-1- ^{13}C , or position 8 in acetone-2- ^{13}C .

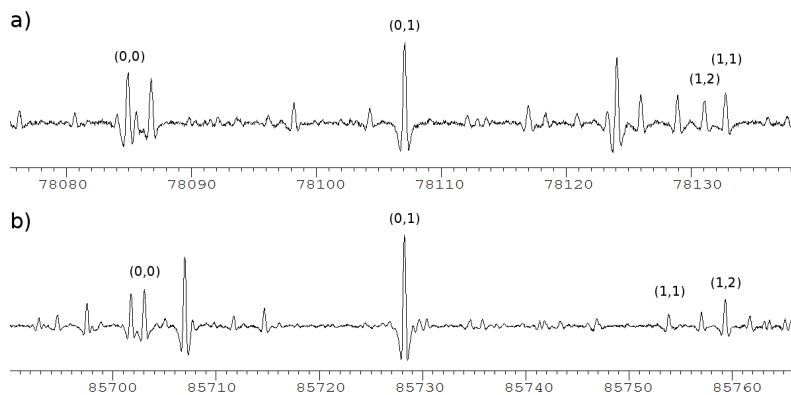


Figure 2.6: The relative intensities predicted by group theory are observed in the spectrum of acetone-2- ^{13}C . a) Components of the $eo \leftarrow oe$ transition $33_{20,13} \leftarrow 33_{19,14}$. b) Components of the $oo \leftarrow ee$ transition $32_{19,13} \leftarrow 32_{18,14}$. The symmetry labels are shown as used in ERHAM and base upon the *modulo* 3 equivalence of 2 and -1 . Frequencies are given in MHz.

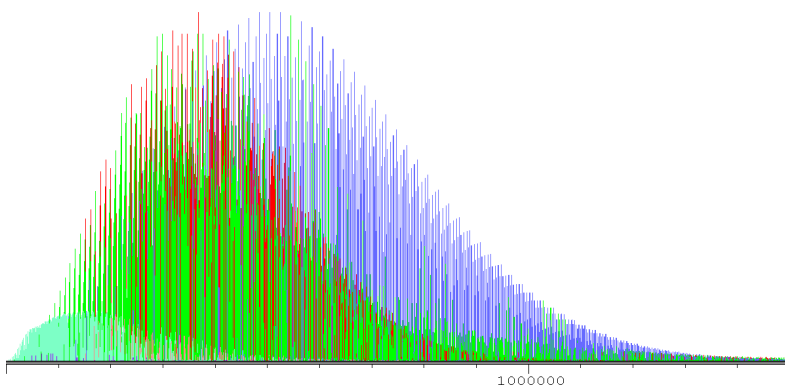


Figure 2.7: Predicted stick spectrum for acetone-2-¹³C from 0 to 1.5 THz. The x axis shows the frequency in MHz. Intensities of blended lines were not added to allow for a better distinction of the spectral components. R -branch colour codes: red = a type, green = b type, blue = c type. bQ -branch lines are shown in turquoise.

Chapter 3

Experiments

Obtaining useful predictions for the rotational spectra required measurements of portions of the actual spectra, followed by iterations of line assignments and fitting of the effective rotational Hamiltonian. The absorption measurements of these spectral portions reported in this chapter and their analysis in Chapter 4 are presented in descending order of progress in the sub-projects. The work on acetone-2- ^{13}C is most advanced because the prediction of ^{13}C spectra was considered the main goal at the beginning of the project and a pure isotopic sample was commercially available. Excluding measurements, the amount of work spent for this isotopologue is estimated with more than 5500 hours (total edit time of the fitting protocol as measured by LibreOffice). For comparison, improving the prediction for acetone- ^{12}C took only 17 days of measurements and 8 days of analysis, thanks to the extensive prediction already available since 2002 [36], but also a result of the knowledge and experience gained with the former isotopologue. Hence, the main isotopologue has the best relation between effort and scientific outcome. Acetone-1- ^{13}C could only be measured in natural abundance because it is commercially unavailable at a reasonable pricing. Research has been conducted towards a chemical experiment where it is expected that a 50% enriched sample of this isotopologue can be synthesised *in situ*, but it could not be realised due to time restrictions at the end of the PhD project. Therefore, this experiment is described here as a proposal, and test results are presented which clarify the details of how to obtain the enriched sample.

3.1 Technical summary

All absorption measurements presented here base upon the same general setup and operation principle. The typical setup (Fig. 3.1) consists of a tunable oscillator generating a polarised, monochromatic RF wave of a desired frequency, an evacuated absorption cell containing the sample gas, and a low-noise, broadband detector matching the frequency range of the source. Further common aspects are the cell technology (borosilicate glass tubes with 10 cm diameter, flanged together with PTFE gaskets, ends covered by PTFE windows tilted 10 degrees to reduce surface reflections) and the 10 MHz rubidium frequency standard enabling a frequency resolution of $\frac{df}{f} = 2 \cdot 10^{-10}$ or better. Biconvex HDPE lenses in front of the inlet and outlet window with 100 – 200 mm focal length were used to match the beam emerging from the source antenna to the cell and to focus it onto the detector antenna. In double-pass setups, the same lens can be used for both purposes. Antennas used were horn antennas of the conical Pickett-Potter [81] or diagonal type [46]. Especially below 500 GHz, matching the beam to the cell is important to enable wave propagation by total reflection on the inner surfaces of the otherwise strongly absorptive glass tubes.

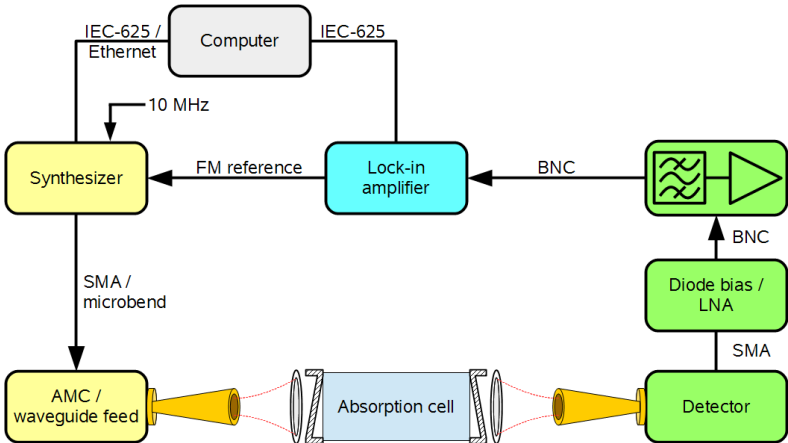


Figure 3.1: The general setup used for all source-modulated absorption measurements in this thesis. Schematic representations of optical parts are not to scale.

Absorption line detection was performed through frequency modulation of the source. To this end, a sine signal (≤ 50 kHz) from the built-in oscillator of the lock-in amplifier was used to modulate the source frequency. The detector output signal was transferred back to the lock-in amplifier, where it was demodulated at the double modulation frequency (2F mode), generating the second derivative of the absorption characteristics thus measured. A frequency-selective amplifier between the detector output and the lock-in amplifier was used to filter and amplify the 2F signal to obtain a monochromatic signal in the mV range. A LabView program was used to control data acquisition from the lock-in via an IEC-625 bus system and to display, process and store the data.

3.2 Spectroscopy of acetone-2-¹³C

3.2.1 Measurements

Seven separate portions of the rotational spectrum of acetone-2-¹³C were measured in the Cologne spectroscopy laboratories at the Institute with several different setups summarised in Table 3.1.

Table 3.1: Acetone-2-¹³C: Measurement setups

Frequency Range	Setup	RF Source	Path Length	Detector
40 – 48 GHz	1 a)	70 GHz synthesizer	2 x 7 m	Schottky diode
75 – 130 GHz	1 b)	43.5 GHz synthesizer + AMC	2 x 7 m	Schottky + tunable backshort
200 – 232 GHz	1 c)	43.5 GHz synthesizer + AMC	2 x 7 m	Schottky diode
270 – 304 GHz	2 a)	Source 1 b) + superlattice multiplier	3.4 m	4 K InSb bolometer
335 – 365 GHz	2 b)	Backward-wave oscillator	3.4 m	4 K InSb bolometer
629 – 710 GHz	2 c)	Microwave synthesizer	3.4 m	4 K InSb bolometer
840 – 910 GHz	2 d)	+ modular AMC system		

The measurements up to 232 GHz were performed at the new millimetre-wave double-pass absorption spectrometer for complex interstellar species (MIDAS-COINS, Setup 1). Its three combinable, exceptionally long absorption cells allow for a total absorption path length of up to 44 m when double-pass optics are used (Figs. 3.2 to 3.4). One or more additional lenses between adjacent cell segments are necessary for setups with long wavelengths or low source power to avoid power losses due to diffraction, which becomes stronger for wavelengths above 1 mm [29], and dielectric absorption in the cell windows and lenses. MIDAS-COINS was constructed to gain sensitivity for spectral measurements of comparably heavy, complex molecules in the millimetre regime, where the important low- J lines are mainly found, but intensities are weak due to a high density of states, an increasing fragmentation of the sample into conformers, and the Boltzmann distribution. Quantitatively, the sensitivity limit of an absorption spectrometer can be characterised by the smallest detectable line-centre power absorption coefficient, defined by $P/P_0 = \exp(-\gamma_{min}L)$. MIDAS-COINS' sensitivity limit has been measured to be not greater than $\gamma_{min} = 4.0 \cdot 10^{-7} \text{ cm}^{-1}$ for its full absorption path length $L = 44 \text{ m}$ at 104 GHz [75].

Measurements with this spectrometer are facilitated by the all-solid-state design of the RF components, which are based on the high electron mobility of GaAs Schottky diodes and render cryogenic parts unnecessary¹. Its double-pass functionality (based on turning the polarisation by 90° with a roof-top mirror of 10 cm base length) has been proven to work at up to 410 GHz at least, the only limiting factor being the large-area beam splitter (10 × 15 cm²). This part is made with silver-coated, parallel Cu conducting paths on a 48 μm thin polyimide film and is expected to become increasingly transparent above this frequency due to the grid constant of 100 μm. The hitherto existing lack of diodes still working at THz frequencies has been mitigated by a modular amplifier / multiplier system², which had come to market during the course of this thesis and is described below. It comprises matching detector diodes for each multiplier stage, which, however, are still outperformed by cryogenic InSb bolometers with their typical NEP levels of a few pW/Hz^{1/2}. Hence,

¹See [16] for a detailed discussion of the state-of-the-art technologies typically used in sub-millimetre spectroscopy.

²Manufacturers and models of laboratory equipment are listed in Appendix B.

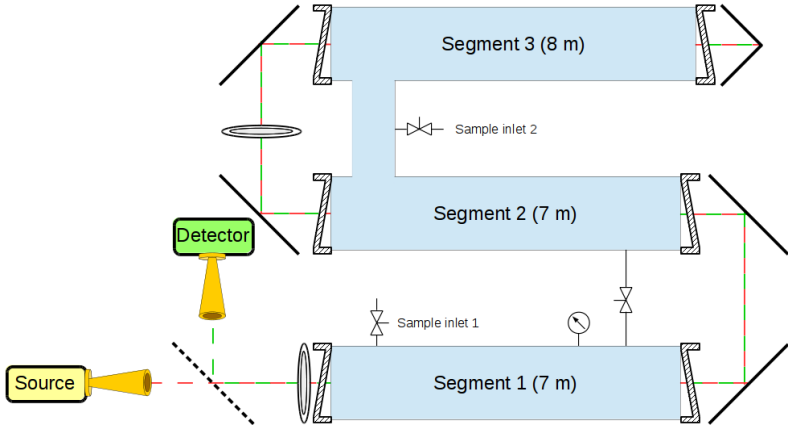


Figure 3.2: Schematic of the MIDAS-COINS optics and vacuum system. The polarised beam emerging from the source (red) passes the polariser and is reflected between the cell segments. The retroreflecting roof-top mirror turns the polarisation planes by 90° around the optical axis. The orientation of the roof-top mirror of 45° around the optical axis with respect to verticality is not shown. The polariser reflects the returning beam (green) into the detector.

the rest of the measurements up to 910 GHz deployed bolometric detection.

Sub-setups 1 a) to c) (Table 3.1) differ mainly in the pairs of source and detector installed. For setup 1 a) the RF output from a high-frequency synthesizer (in the tuning range 38 – 70 GHz; used with a typical output amplitude of 10 – 16 dBm) was directly fed to a waveguide with a short, thin coaxial cable, coupled out to the cell, and received again with a Schottky diode mounted in a waveguide. Setup 1 b) featured an amplifier-multiplier chain (AMC) as a source, with a synthesizer (10 – 43.5 GHz) being the primary oscillator and a frequency multiplication factor of three.

The AMC in setup 1 b) provides an average output power of 8 mW in the frequency range $\sim 80 - 110$ GHz. The waveguide containing the matching Schottky diode has its back side closed with a tunable back-short to circumvent dephasing losses. This technology necessitates the operator to retune the detector about every 1 GHz



Figure 3.3: Laboratory photograph of a major part of the three MIDAS-COINS absorption cells.

to maintain optimum signal recovery, but makes it possible to use the same setup over the whole tuning range of the source (75–130 GHz) and to compensate the pronounced variations of source power. The output power of source 1 b) typically varies by 3 mW in- or decrease within 600 MHz over most of the bandwidth of 55 GHz. A different AMC (multiplication factor 16, typical output 40 mW) and Schottky diode were used in setup 1 c).

Negative bias current for all Schottky diodes in setup 1 was supplied by bias boxes bespoke designed and built in analogue technology at the Institute. These bias boxes contain a low-noise operational amplifier circuit to amplify the rectified output signal from the diode before it is passed on to the frequency-selective amplifier. Suitable horn antennas [81] were used in setups 1 and 2 b), whereas diagonal antennas [46] were used otherwise.

Setup 2 is the Cologne sub-millimetre spectrometer, which uses a 3.4-m cell and the cryogenic InSb bolometer mentioned above as

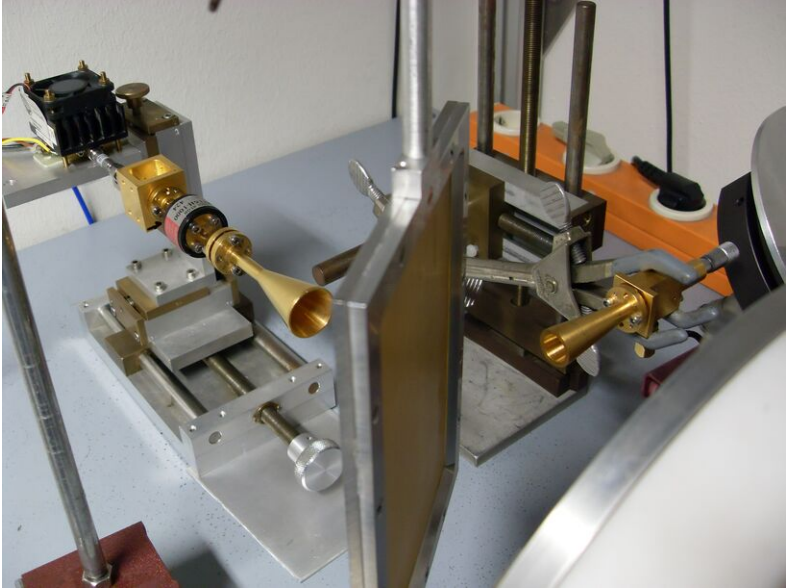


Figure 3.4: Laboratory photograph of an exemplary setup [Setup 1 b)] of radiation source (left) and Schottky detector (right). The beam splitter is visible in the centre. Parts of a cell window and a plane mirror are visible in the lower right corner and on the right border, respectively.

main components. Usually only the RF source was exchanged for a particular frequency range, because the bolometer's thermal detection principle allows for a very broad detection bandwidth (microwave up to a few THz). The detector comes with a built-in bias box containing a low-noise amplifier circuitry similar to that of the custom devices mentioned above.

This setup was first used with a backward-wave oscillator (BWO) as a radiation source around 350 GHz [setup 2 b)]. Details regarding the operation principle of the BWO sources used at the Institute are described in [57]. Radiation is generated by periodic acceleration and deceleration of electrons in a vacuum tube during their motion within a strong magnetic field along a microfabricated metal structure with a comb-like nonlinear geometry. The quasi-free movement

of electrons guarantees a high output power over the whole tuning range of the tube (> 30 mW on a tuning range of > 100 GHz for the 300-GHz tube “OB-30” used here). The BWO is operated as a sideband spectrometer: A harmonic mixer fed by part of the radiation from the beam and a local oscillator tuned to a frequency $f_{LO} = (f_{BWO} \pm 350 \text{ MHz})/m$, m being an odd integer, generates a sideband signal of 350 MHz, which is used to lock the BWO frequency by an automatically tuning phase-locked loop device (PLL). The local oscillator used for this work was an identical AMC as in setup 1 b). A redraw of this setup was that the PLL used here was a replacement for the one originally described in [57], which had allowed for broadband measurements of 1 GHz or more once the BWO frequency was locked. Contrastingly, the acetone-2-¹³C spectrum of 30 GHz was acquired in 612 single scans as the spare PLL lost lock if a range of a few ten MHz was exceeded.

After the BWO measurements, setup 2 a) was intended as a test with the same cell and detector to find out if the 100-GHz source from setup 1 b) delivers enough power to reach multiplication factors of 5 or more with a superlattice multiplier [21, 76] in order to access frequencies above 400 GHz. This test failed, yet a sufficiently strong signal identified as the pure third harmonic enabled broadband spectroscopy of acetone-2-¹³C around 300 GHz. The superlattice multiplier belongs to a series of similar devices which had been given to the Cologne spectroscopy workgroup (at the Institute) during a long-lasting collaboration with Dmitry Pavelyev³.

The goal of determining all relevant spectroscopic parameters sufficiently well for a precise prediction at least down to $\lambda \approx 2$ mm could not be met with the data collected from the experiments described so far. An inspection of the predicted spectrum as a whole (Fig. 2.7) showed that measurements up to about 1 THz were worthwhile to obtain a diversification in quantum numbers which could be expected to be adequate as a remedy. Laboratory work on this isotopologue was hence continued when a new solid-state radiation source with a frequency coverage up to 1.1 THz became available in 2014 [Setups 2 c) and d)]. Dubbed “THz Starter Kit” by the manufacturer (see Appendix B), it is a modular system consisting of a microwave-driven basis system, which is essentially an AMC with multiplication factor 9 enhanced by external modulation and power control capabil-

³Lobachevsky State University of Nizhny Novgorod, Russia

ity, and five waveguide-mounted multipliers (three doublers and two triplers) externally connectable to its output flange. The frequency range of 82–125 GHz accessible by the basis system can thus be multiplied by 2, 3, 4, 6 [Setup 2 c)], and 9 [Setup 2 d)] to cover the entire range mentioned, with only one gap between 125 and 170 GHz. The standard single-pass setup with the InSb bolometer, which provides sufficiently high sensitivity to compensate the power losses at high multiplication factors due to photonic energy conservation, was used again for broadband measurements in two atmospheric transmission windows up to 710 and 910 GHz.

3.3 Spectroscopy of acetone-¹²C

Spectral measurements of acetone's main isotopologue were originally done to search for the strongest lines of acetone-1-¹³C in natural abundance. This first approach was a response to the poor commercial availability of this isotopologue. The predictions by Lovas and Groner [60] were good up to the millimetre-wave region, so the idea formed to use the liquid helium-cooled InSb bolometer described in Section 3.2, being the most sensitive detector available for absorption experiments in this range at the Institute, in combination with Source 1 a), to search for the strongest lines, which were expected to be 2–3 orders of magnitude less intense than those of the main isotopologue (see Section 3.4).

Besides the single-line scans described there, too, preparatory broadband measurements were performed with the THz Starter Kit (Section 3.2) in frequency regions originally selected for future measurements of an enriched sample of acetone-1-¹³C (Section 3.4.2). The ¹²C spectra acquired this way were intended to be subtracted from the spectra of the enriched sample to filter out the lines from the main isotopologue, allowing for increased intensities relative to the by-product acetone-1,3-¹³C₂ by intentionally shifting the educts' stoichiometry (see the detailed explanations in Section 3.4.2). Four frequency regions (83–125 GHz, 200–250 GHz, 400–475 GHz and 800–908 GHz) could be covered in only one week thanks to the high multiplication factors of 9 to 81, allowing to exploit the synthesizer's high switching speed at microwave frequencies. Yet the first of these measurements, together with the 70-GHz measurements described above, would prove later to be sufficient for a substantial

improvement of the prediction for the main isotopologue.

3.4 Spectroscopy of acetone-1-¹³C

3.4.1 Detection in natural abundance

As explained above, the consequence of the commercial unavailability of this isotopologue is to either detect it in natural abundance in a sample of acetone-¹²C, or to chemically synthesise or enrich it in the laboratory. At the beginning of this project, the former method was chosen because of its lower barrier to realisation. The natural abundances of the acetone ¹³C isotopologues can be derived using the isotopic abundance of carbon-13, which is roughly 1.1%, from the diagram shown in Fig. 3.5. Multiplication along the paths yields a list of absolute abundances:

98.9% acetone- ¹² C	79.8 ppm acetone-1,2- ¹³ C ₂
7.25‰ acetone-1- ¹³ C	39.9 ppm acetone-1,3- ¹³ C ₂
3.63‰ acetone-2- ¹³ C	1.33 ppm acetone- ¹³ C ₃

Relevant for this thesis are the relative abundances of the three isotopologues to the left, which are 273 : 2 : 1 in rounded numbers, or 1 : 0.00733 : 0.00367 normalised to the abundance of the main isotopologue. Owing to molecular complexity, the lines of the latter are already weak and dense enough to reach the limit of detectivity

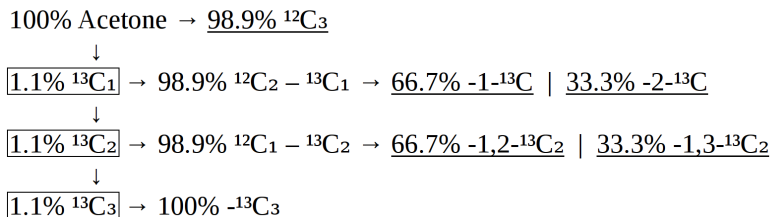


Figure 3.5: Derivation of isotopic abundances for all ¹³C isotopologues in a terrestrial sample of acetone. The 2:1 mixture of isotopomers at the *mono* and *di* stages results from statistical distribution.

if the spectra are to be explored for lines more than two orders of magnitude weaker. These circumstances indicated that a search in natural abundance could become successful only if measures were taken to increase sensitivity beyond the usual standard.

In a first approach, the range 36 – 70 GHz, where the uncertainties of the predictions by Lovas and Groner [60] were comparably small, was covered by broadband scans with the Cologne sub-millimetre spectrometer working with a combination of setup 2 a) (Table 3.1) and the source from setup 1 a). The spectra were measured at a comparably high pressure (14 μ bar in constant gas flux through the cell, compared to 5 μ bar initial static-gas pressure for acetone-2- ^{13}C) in order to improve the signal-to-noise ratio (SNR) and facilitate overnight measurements at a small expense of line centre frequency accuracy. SNR was further increased by slight over-modulation (ratio of FM deviation to HWHM⁴ ≈ 1 instead of ≤ 0.8 for acetone-2- ^{13}C).

After some lines had been assigned in this range (see the analysis in Section 4.5), an improved prediction was made, enabling further measurements around the predicted frequencies of transitions with $K = 0 \leftrightarrow 1$ at increased sensitivity in order to try whether it is possible to extend the range of quantum numbers in the J direction. The mentioned transitions belong to the strongest lines for a given J and feature a torsional splitting of only a few MHz, so that the characteristic intensity pattern derived in Section 2.5.3 is visible on one screen. For these “single-line” scans the Cologne sub-millimetre spectrometer (setups 2 in Table 3.1) was used instead of MIDAS-COINS, the main reason being that the first scans of this type were done with the superlattice source 2 a), which is too low in power to overcome dielectric absorption in the cell windows and long glass tubes. The regions measured with the superlattice multiplier span the range between 244 and 351 GHz, corresponding to $J = 25 - 36$. This was accomplished afterwards by measurements with source 1 b) between 81 and 130 GHz ($J = 8 - 13$). Said frequency ranges are advantageous because they approach the Boltzmann peak of absolute intensities (cf. Fig. 2.7) and the spectral baseline acquired from surface reflections gets weaker with increasing frequency. The measurements were performed with a static gas under starting pressures

⁴One half line width at half maximum, a common measure for line widths which will be used here throughout.

around 10 μbar .

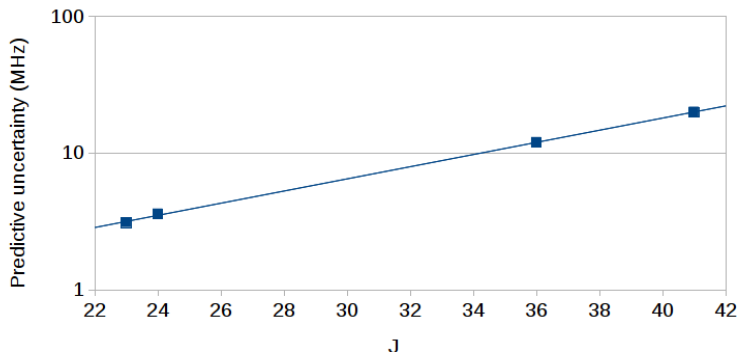


Figure 3.6: Progression of predictive uncertainty for the $K = 1 \leftarrow 0$ transitions of acetone-1-¹³C. The four sample points (squares) taken from a prediction are best fit (solid line) by the exponential law $(\Delta f)_{\text{pred}} \approx 0.3 \exp(0.1J)$ ($R^2 = 0.99955$). In the J range considered, a cubic power law $(\Delta f)_{\text{pred}} \approx 0.00016J^{3.15}$ can also be fit with the slightly worse coefficient of determination $R^2 = 0.9978$.

Besides overmodulation (FM deviation / HWHM = 1.5 [at 1 mm] and 1.33 [at 3 mm]), an increase in sensitivity could be achieved by long integration times. A total integration time of 1.8 s per frequency point was reached by averaging 3 times per visited frequency during 3 up- and downward scans with a lock-in time constant of 100 ms. As a special care taken to reduce aliasing (i.e., to decorrelate adjacent points), a delay time of 400 ms to be added before the first measurement at each frequency was set in the control software. This delay time is a compromise between the needs for a short scanning time and the best precision: A test scan with a time constant of 1 s was made to find out, by visual inspection of the lock-in display, the shortest delay time needed for full decoupling of subsequent data points (anti-aliasing). The delay time found was 8 s, so it can be concluded that the highest precision is reached if the delay time is eight times the time constant. For comparison, a usual spectral measurement with reasonably strong intrinsic intensities is one scan up- and downward, with no averaging per frequency visit, no additional

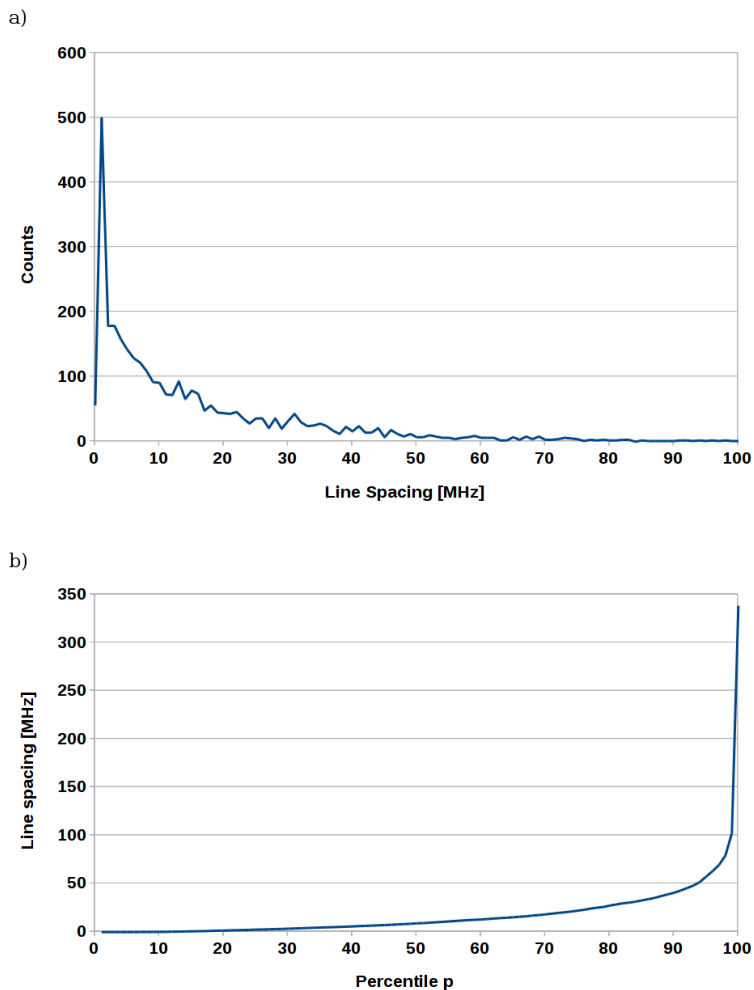


Figure 3.7: a) Distribution of line spacings in the spectrum of acetone between 75 and 130 GHz, as predicted by Groner *et al.* [36] and available in the Cologne Database for Molecular Spectroscopy (CDMS) [68–70]. b) Percentile curve of the spacings.

delay time and a time constant of 20 ms.

During the test, it was also found that the balance between anti-aliasing and lock-in relaxation speed can be controlled with a previously unknown setting of the lock-in detector: The model used for all measurements in this thesis comes with a digital filter for the X (output) channel, the steepness of which can be chosen between 6, 12, 18, and 24 decibel per octave (dB/oct.) [66]. A steeper slope corresponds to better hardware anti-aliasing. The first setting corresponds to a first-order filter (filter gain antiproportional to frequency in the high- f limit), the second to second-order filtering etc. The choice of steepness for this filter (implemented by the envelope of a frequency response function) directly influences the sampling process in the lock-in's main ADC. For the high-precision measurements presented here, second-order filtering was used, whereas a higher setting would have enforced even higher delay times. Particularly, the "eight times the time constant" rule found for the delay time holds only for this setting. Otherwise, for measurements with standard sensitivity as described before, first-order filtering is acceptable in most cases, though leading to slightly broader lines due to frequency shifts between the up- and downward scans.

The increase in integration and delay time resulted in a long duration of measurements (up to 6:32 hours for one prediction with scan widths calculated as explained below), especially for the measurements around 3 mm, where the switching speed of the synthesizer was significantly lower owing to the frequency multiplication factor of 3. This required an analysis to determine the minimum width to be scanned around each predicted line frequency. As superposition often prevents an identification of candidates for all torsional components of a rotational transition, candidates must be measured against known, unperturbed lines of the main isotopologue (calibration lines). The minimum width to be scanned is thus determined by the number of lines from the main isotopologue available for intensity calibration rather than the progression of predictive uncertainty, which follows an exponential law (Fig. 3.6), but increases still too slowly within the range of J values covered by the measurements to get a high probability of including at least one sufficiently strong calibration line.

The number of available calibration lines was taken into account indirectly by deriving a rule-of-thumb formula from a statistical analysis of the line spacings encountered in the main isotopologue pre-

diction by Groner *et al.* [36]. For this purpose, 3338 frequencies predicted for the main isotopologue in the range accessible by source 1 b) were imported into a spreadsheet and the distances of subsequent lines were calculated. Fig. 3.7 shows the differences categorised in multiples of 1 MHz [diagram a)] and as percentiles [diagram b)]. The differences of spacings for subsequent percentiles, expressed as fractions of the greatest line distance (338.651 MHz here), gives another curve which is proportional to the slope of the original percentile curve. A detail of this curve, shown in Fig. 3.8, compares percentages of line spacing differences to percentiles of line spacings, visualising the result of this analysis by interpretation as follows: For one given centre frequency f_c of a scan around a particular predicted frequency, the efforts to obtain further calibration lines become unfeasible if one has to invest more than one percent of the maximum line spacing to see one percent more prospective calibration lines. For the analysed data set, its centre frequency being $f_c = 102.5$ GHz, this is the case for the 94th percentile onwards, corresponding to a line spacing $\Delta f(f_c) = 51.9$ MHz. From these values the rule of thumb “Scan width in MHz \approx centre frequency in GHz $\times 0.5$ ” was derived.

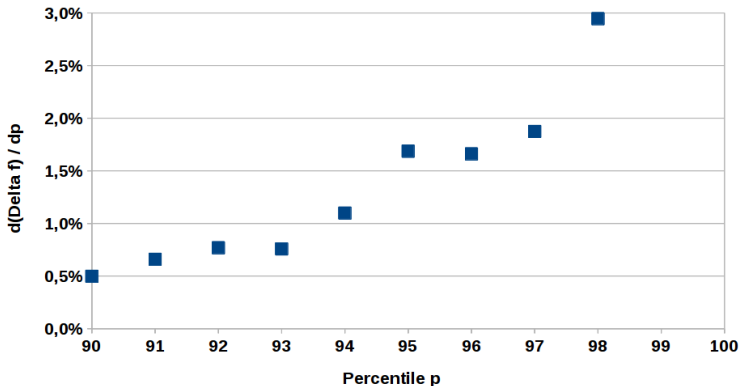


Figure 3.8: Slope of the percentile curve shown in Fig. 3.7 b) around P95. An extension of frequency range becomes unfeasible if one has to invest more than 1% of the maximum line spacing to measure 1% more calibration lines.

3.4.2 Proposed experiment for an in-situ synthesis

The outcome of the tedious work described above is insufficient for the needs of modern astronomy, where all torsional components, at least of the strongest lines, should be predicted to experimental precision in a useful frequency range (e.g. up to $\lambda = 2$ mm). Only few of the strongest lines with low values of J and K could be discerned from background noise or superposing lines from other isotopologues, which occurred frequently due to spectral density. As will be shown in Chapter 4, said goal can only be achieved at experimental precision with a combination of a sufficiently large data set of at least a few thousand transitions and a suitable, minimal selection of parameters. Therefore, further research was conducted to find a method to produce a pure or enriched sample of acetone-1-¹³C. First attempts on a Grignard synthesis [96, 103] in collaboration with chemists from the group of Axel Klein (Department of Chemistry, University of Cologne) failed due to the close boiling points of solvent and product.

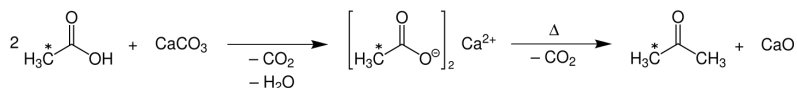


Figure 3.9: Reaction scheme for the dry distillation of calcium acetate. The position to be partially substituted by a ¹³C atom is marked with an asterisk. Image based on the original image created by Renate90 [83].

It was rather found that acetone can be produced by dry distillation (pyrolysis) of acetates. This synthesis procedure goes back to the early years of chemistry, when the synthesis of acetone by dry distillation of lead acetate was first described by Libavius (1606) [58]. Based on the cheaper and non-toxic calcium acetate, this technique⁵ was later used for industrial-scale production up to the 1950s [56]. A series of experiments sufficiently close to the method described here was reported by Neunhoffer and Paschke [73], who obtained acetone by heating of pure acetic acid in a closed quartz glass tube, or in a hot gas stream of acetic acid in both presence and absence

⁵Called *Kalksalzdestillation* in German, which translates to “lime salt distillation” in English.

of sodium acetate, at temperatures between 300 and 450 °C.

Whereas the literature describes efficient ways to form acetone directly from acetic acid, e.g. using a hot ThO_2 or MnO catalyst in a water-free environment [103], a lower degree of experimental complexity suitable for a physics laboratory can, however, be reached by classical lime salt distillation. Selectively incorporating carbon-13 into one of acetone's methyl groups can be achieved by subdividing the reaction into two steps (Fig. 3.9): First, solid calcium acetate is formed by deprotonation of acetic acid, which is commercially available with carbon-13 at the methyl position (acetic acid-2- ^{13}C), with calcium carbonate. As no further solid products occur, the acetate can be easily filtered from the solvent and the reaction can be conducted with standard equipment in a chemical laboratory. This step was successfully tested in the laboratories of Uwe Ruschewitz (Department of Chemistry, University of Cologne).

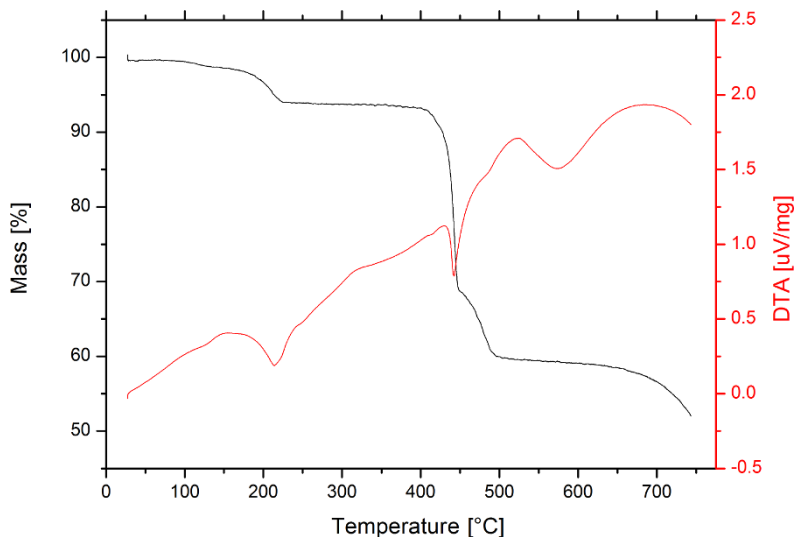


Figure 3.10: DT-TG measurement of calcium acetate. Acetone formation is observed above 400 °C, followed by a by-product above 450 °C. The endothermic peak above 150 °C is attributed to loss of crystal water. Image courtesy of Stefanie Busch, Chemistry Department, University of Cologne

The salt thus created is then dried and transferred to a half-side closed, jointless fused quartz tube suitable for heating in a tube furnace. At temperatures above 300 °C, the carbonate ions start to react with each other, forming solid calcium oxide, gaseous acetone and carbon dioxide. A catalytic function of the calcium carbonate as described in the literature [103], avoiding an output of CO₂, was neither observed in a test run with calcium acetate-¹²C at 450 °C, nor in the DT-TG⁶ measurement shown in Fig. 3.10. It is, however, possible that the conditions of these tests were too unfavourable (e.g. intentionally too high furnace temperature in the test run because an observation of grey CaO powder was expected; too quick temperature rise or an influence of air humidity during the DT-TG scan) to observe the reaction as described. This possibility should be tested when the experiment described below is set up in the future. If the formation of CO₂ cannot be avoided though, it becomes obvious from the reaction scheme (Fig. 3.9) that no carbon-13 from the methyl groups (see the consideration below) can be lost through this channel, which is another advantage of the proposed reaction scheme.

The DT-TG curve gives deeper insight on the details of the pyrolysis, which shall be exploited in the experimental realisation. Acetone formation is seen to start above 400 °C, which is quite high, but still in accordance with the furnace test run mentioned above. The steep drop of sample mass suggests that the reaction can be controlled only if the temperature is kept at a value T_{R-} low enough to just start the reaction. A low temperature is preferable by several further reasons: First, a too fast reaction would also result in an uncontrolled rise of pressure by the CO₂ produced alongside, which would deteriorate the vacuum and could even destroy the equipment if 1 bar is surpassed; and second, small amounts of product can be stored in the trap more effectively. Additionally, a slowdown of mass loss is observed above 450 °C, which is supposed to originate in the formation of acetone cracking products [103] and another reason to keep the temperature low. The cracking products were seen as a yellow staining in the condensed acetone sample. Care should also be taken that a temperature gradient in the quartz tube be avoided (by

⁶DT-TG is a combined differential thermal analysis (DTA) and thermogravimetric analysis (TGA), where the calorimetric behaviour and mass loss of a sample in an open oven are observed over a temperature ramp with constant rate. Equipment for this standardised procedure is commercially available.

heating up slowly) to suppress acetone cracking on the walls. Another endothermic reaction with a mass loss of some 5% seen above 150 °C is ascribed to the evaporation of crystal water, which has to be removed from the sample before acetone formation is started.

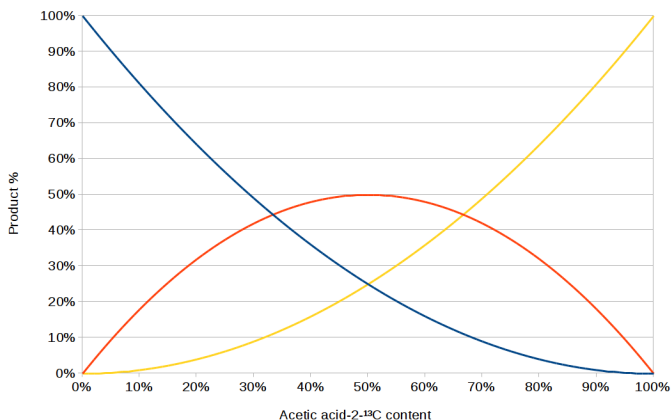


Figure 3.11: Theoretical yield of acetone-1-¹³C as a function of the content of isotopically enriched acetic acid at the beginning of synthesis. Products: blue = 12-12; yellow = 13-13; red = 12-13. The curves have been calculated from the molar fraction x of isotopic acetic acid by $x_{12-12} = (1 - x)^2$, $x_{13-13} = x^2$, and $x_{12-13} = 1 - x_{12-12} - x_{13-13}$.

The proposed reaction supports a selective ¹³C enrichment of the methyl groups. The isotope must be introduced by mixing natural acetic acid with a pure isotopic sample at the beginning of the first reaction. Fig. 3.11 shows the amount of the respective acetone isotopologues which will be produced from an acetic acid mixture of a given isotopic content. The highest yield of 50% acetone-1-¹³C is achieved with a 1:1 mixture of acetic acid-¹²C and acetic acid-2-¹³C. The reaction tolerates ±16% inaccuracy of mixture within 5% loss of desired product. A shift towards a lower portion of acetic acid-¹³C is justifiable to increase the ratio of acetone-1-¹³C to acetone-1,3-¹³C₂, as the spectrum of acetone-¹²C has been measured and can be subtracted from the spectrum of the mixed sample. For in-

stance, as a good compromise between preferences regarding a high absolute abundance of acetone-1-¹³C and a high abundance ratio to acetone-¹³C₂, an enrichment of only 33% would yield a 1:1 mixture of acetone-1-¹³C with the main isotopologue, while the ratio to doubly substituted acetone were 4:1. Using an enrichment below 33% is not recommended because of the low production efficiency, leading to a low signal-to-noise ratio for the desired product due to a low absolute abundance, and because this would mean a too high reliance on the quality of the acetone-¹²C spectrum to be subtracted.

A last obstacle to be overcome by the experiment is the capture and storage of the product. A separation of acetone from the vapour phase in a simple condenser tube is not advisable because of its volatility (vapour pressure⁷ roughly 200 mbar at 15 °C): it would evaporate during the CO₂ removal. On the other hand, removing the CO₂ is essential because its partial pressure would rise above any practical limit otherwise (vapour pressure ~ 57 bar at room temperature). A better approach is to remove the carbon dioxide by sublimation, which can normally be done in a cold trap, e.g. at liquid nitrogen temperature. However, as no reliable data for the boiling points of acetone and carbon dioxide under vacuum conditions could be found, it had to be verified experimentally whether a separation of the products could be performed as imagined.

In a preliminary experiment, a small amount of liquid acetone was filled into a glass bulb with an inlet valve for the sample and an outlet valve connected to a turbomolecular pump, and cooled down to 77 K with liquid nitrogen. Only the bottom of the bulb was immersed, so that the air in the bulb could be pumped out after the acetone had frozen. It was observed that the sample had not frozen out completely; instead, its central region remained in a jellylike condition. This is in accordance with the observed residual pressure, which could not be reduced below 500 μbar even when the bulb was immersed as a whole. The most successful freeze-out of acetone with a final background pressure of 1.5 μbar was realised by opening and closing the outlet valve several times with the bulb completely immersed.

The experiment was repeated with carbon dioxide, which was let into the bulb after having been evacuated and cooled to 77 K. The

⁷The vapour pressures given in this section were extrapolated from data points available in the GESTIS database [25].

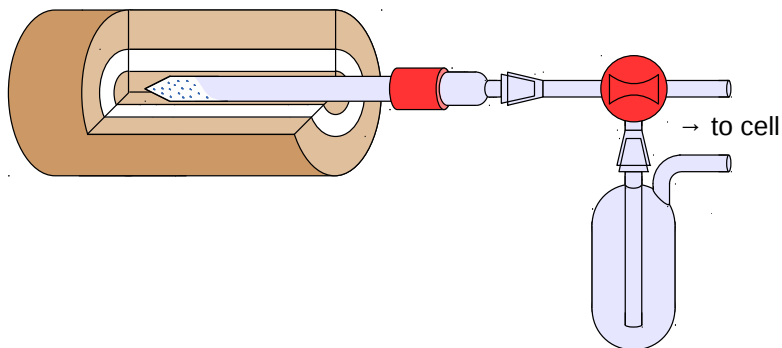


Figure 3.12: Schematic setup of the proposed experiment for an in-situ synthesis of acetone-1- ^{13}C . A pointed tube containing the calcium acetate sample (dotted light yellow) is centered in the tube furnace (brown). The reaction products can be fed to the cold trap flask by turning the valve (red). The liquid nitrogen bath, parts providing the connection to the absorption cell and several auxiliary parts are not shown.

gas deposited immediately on the walls, but left a residual pressure of 1.2 mbar. In contrast to acetone, this residual pressure could be pumped out quickly and completely, and no further evaporation of CO_2 was observed after having closed the outlet valve again. This proves that freezing out is an effective way to purify the acetone from the vapour after its formation.

Based on these insights, an experimental setup can be proposed (Fig. 3.12): The tube furnace is mounted in an elevated position, providing enough vertical space for the cold trap and the liquid nitrogen dewar standing on a laboratory jack. The oven hosts the quartz sample tube and is sealed against laboratory air with glass paddings. The sample tube has a diameter of 20 mm, which must be matched to the rest of the glass equipment outside the cell (13 mm diameter). This is done by a connector with a glass joint and a PTFE pressure sleeve. A valve shall be used to bypass the cold trap during the removal of crystal water vapour. This valve is not essential and may be omitted if introducing additional junctions affects vacuum quality stronger than expected. In this case cell and oven should be permanently connected to the cold trap, which may be cooled

down after removing the crystal water. The cold trap consists of a two-necked cylindrical flask with a glass tube fed through its upper neck and reaching its bottom. The glass setup may be connected to the cell inlet valve by a rubber hose with matching joints. Sufficient vacuum tightness has been verified for a for a setup where the quartz tube fittings were directly connected to the cell, i.e. without valve and cold trap. Trap and valve should not be omitted if a way is found to perform a catalytic reaction without CO₂ generation, as the trap allows for efficient collection and controlled release of the sample.

To the current state of knowledge, the best practice to conduct the experiment with this setup is as follows: Removal of crystal water is done first by heating up the sample to 250 °C with the valve in bypass position and the cell inlet open. When the pressure has relaxed, the glass valve is turned into trap position or, respectively, the cold trap is cooled down. The heat is then carefully increased to T_{R-} and the pressure rise is observed while some acetone is formed. If the amount of educt is too small, the reaction can alternatively be performed with the cell inlet valve closed to increase freeze-out efficiency. Oven temperature is to be decreased early enough to avoid overproduction, as any excess acetone will be removed with the CO₂ background pressure when the cold trap heats up again. The liquid nitrogen reservoir must be refilled manually. Unattended overnight scans are impossible for the same reasons. However, a thermally insulated, pressureless liquid nitrogen reservoir with a small outlet through a hose (dubbed “chicken feeder” by practical analogy) is available at the Institute and could be tried for continuous nitrogen refilling to avoid these problems if the reaction cannot be run catalytically. In this case, preserving the sample in the glass tubes at room temperature to continue measuring on the next day would be possible. A preliminary experiment with regular calcium acetate is suggested to find a way to run the reaction without CO₂ generation, to identify the reaction temperature T_{R-} , and to clarify the need for manual pressure control and the allowable reaction duration for creating the right amount of sample needed for one spectral measurement.

Chapter 4

Spectral analysis and results

4.1 Data analysis with AABS

The software package AABS¹ developed by Z. Kisiel [48, 49] was used to visualise the experimental data and assign line frequencies to predicted transitions for all species and torsional excitations treated here. A screenshot of a typical working session is shown in Fig. 4.1. AABS has been designed for keyboard-only operation to process large amounts of spectral data in a short time.

The display of experimental and calculated data is implemented in the two independent programs SVIEW_L and ASCP_L, respectively, which can be operated synchronously by providing a predetermined settings file in the working directory. Functions of SVIEW_L include zooming and shifting, background subtraction [50], smoothing, peak finding, distance measurements and `gle` output. ASCP_L can display simulated stick and / or contour spectra of multiple catalogues with a diversified colour map, quickly navigate and filter transitions of a specified type, flip through transitions within a blended line, and indicate frequencies where an assignment was already made. An assignment is made by placing a marker on a candidate transition from the catalogue and shifting an independent cursor to the frequency

¹Assignment and Analysis of Broadband Spectra

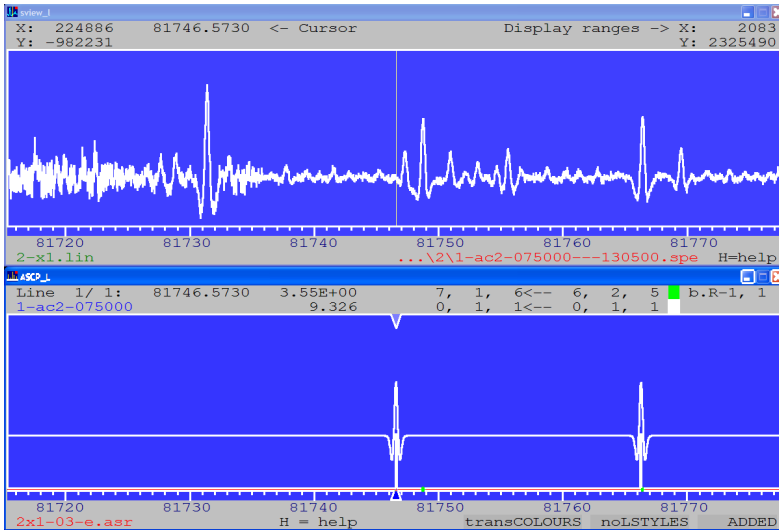


Figure 4.1: Screenshot of a typical assigning session with AABS. Upper panel: Display of the measured spectrum in `SVIEW_L`. Lower panel: Combined stick and contour plot of a predicted spectrum in `ASCP_L`. Assigned frequencies stored in an `SPFIT` line file are highlighted with green points. The linked operation of both programs is indicated by a red square in the upper right corner of both windows. Colours and white lines have been edited for clearer visibility.

of the identified candidate line in the measured spectrum. The frequency to be assigned is determined numerically by a parabola fit to a user-defined number of points around a local extremum.

Data processing of measured spectra (Fig. 4.2) included averaging of all recorded up- and downward scans, and scaling of frequencies and intensities with fixed factors as needed. The data was loaded once into `SVIEW_L` from ASCII files, but stored in a more convenient binary format (in-house standard of the developer). Input of predictions into `ASCP_L` was done in the `ASROT` format defined by the same developer [47]. Each transition assigned with AABS is saved in a line file of the `SPFIT` format used in the software by H. M. Pickett [80].

Kisiel provides several auxiliary programs [47] to facilitate data

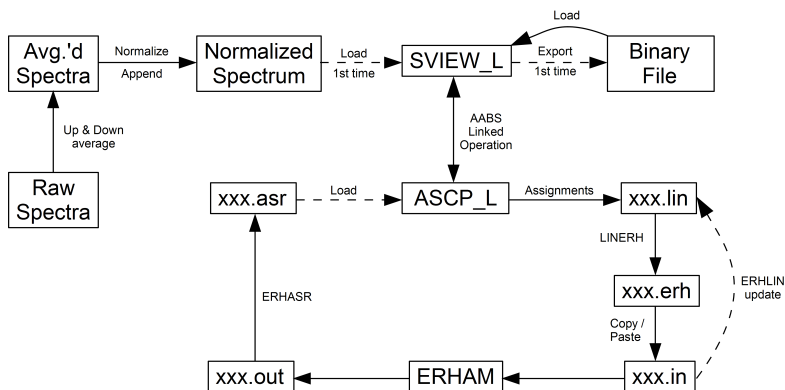


Figure 4.2: Work sequence diagram for the processing of spectral data with AABS and ERHAM, involving measurements, conversion, line assignments, fitting and prediction.

conversion between the different in- and output formats. In the course of this work, slight changes and improvements were introduced to these programs, e.g. in order to enable processing of larger files. A new `.in` to `.lin` converter, ERHLIN, was written in FORTRAN as a substitute for Kisiel's converter ERHRES, which was too bulky in handling and functionality to enable quick data conversions and could not have been easily adapted to recent changes in the ERHAM data format.

Experimental uncertainties Δf for the assigned frequencies were chosen such that the relation $HWHM \approx 6.6\Delta f$ holds on average. The ratio 6.6 was identified as the average number of frequency steps df needed to cover one HWHM in the acetone- ^{13}C measurements up to 365 GHz, including a representative estimate for the assignments provided by Lovas and Groner [60].

4.2 Fitting procedure with ERHAM

Once a new set of assignments was made, it was incorporated into the existing list of assignments and the extended data set was fit with ERHAM. Fitting had to be repeated many times for each data set under systematic variations of the parameters until a maximum number of

assignments could be fit with a minimum number of parameters, of the lowest possible order, in the best case without increasing the residue. If realistic measures have been chosen for the experimental uncertainties, the desired goal for the optimisation of the parameter set is a weighted dimensionless error (standard or root-mean-square deviation²) of 1.0. A standard deviation greatly exceeding 1.0 would mean a bad fit or too optimistic uncertainties; if it was notably below 1.0, the fit would be more accurate than expected within the borders of uncertainty. This section explains the details of the optimisation procedure and the experiences encountered with ERHAM while trying to attain the best fit.

With ERHAM's cubic time complexity in J (see Fig. 4.3) it becomes very time-consuming to find the best parameter set when the data set involves high quantum numbers, which became the case during the extensive assignments from the ground-state spectrum of acetone-2-¹³C. In addition, it was sometimes necessary to temporarily activate a very large number of parameters (sometimes more than 120) from which all unfeasible parameters had to be removed subsequently. This development enforced an efficiency optimisation of the fitting procedure.

The following procedure has proven to be most efficient in finding the optimal parameters when new lines have been assigned:

- Run a fit with the existing parameter set from the last fit which was successful without the new assignments.
- Check the summary of largest errors (cf. Section 2.4.2) for outliers in the data set. An assignment is considered as an outlier if its error substantially exceeds the error target of the current fit³. The target pursued for a good final fit of any data set in this work was one HWHM, but higher deviations were usually accepted before the final stages of the procedure had been reached. Outliers may reflect false assignments or datapoints that require additional parameters because their quantum numbers are out of the range covered by the current

²No details about the calculation of the standard deviation are provided with ERHAM; the root-mean-square deviation stated within ERHAMZ is $\sqrt{\frac{1}{N} \sum_{i=1}^N \frac{f_{obs} - f_{calc}}{\Delta f_{obs}}}$ and provides values very similar to the original ERHAM standard deviation.

³During the first fitting cycles immediately after new lines have been added, an error target of more than one HWHM may be acceptable.

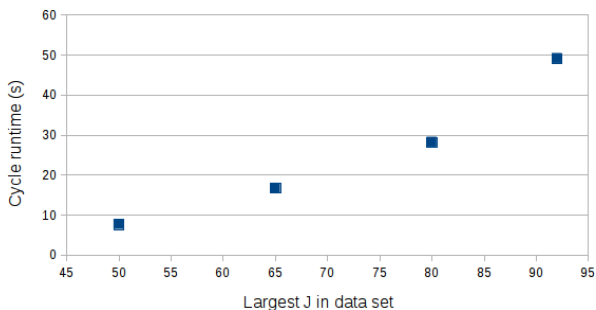


Figure 4.3: Time complexity of ERHAM in J as measured by manually stopping the execution time of each cycle in a three-cycle fit of the full data set for acetone-2- ^{13}C ($J \leq 92$) or identical fits of the same data set truncated to the indicated values. The size difference of the data sets (7627 transitions for $J \leq 50$; 9758 for $J \leq 92$) is supposed to have an effect not stronger than linear. To improve reproducibility, the fits were repeated until both the standard deviation and the difference between least and greatest cycle duration did not exceed 1 second. The values were determined by parallel execution on an 8-core 2.5 GHz machine. The data are fit equally well ($R^2 = 0.994$) by a cubic or exponential law.

parameter set. Said definition is partly subjective as it depends on the “normal” size of deviations between assigned and calculated frequencies encountered in the current fit and implies that reasonable convergence is achieved for most assignments.

Outliers are taken out of the fit for the time being by setting their frequency uncertainties to zero. Later steps aim to reincorporate as many assignments as possible⁴ by identifying the parameter set with the best performance for this data set. As long as the ERHAM model is correct, it can be expected that all outliers remaining after completion of this fitting procedure are false assignments which can be removed and assigned correctly at a later point when the frequency range where the new assignments have been made is revisited with a better prediction. Removal of outliers is repeated until all outliers have

⁴This is greatly facilitated by the usage of standard uncertainties per spectral range rather than individual uncertainties for every assigned line.

been ruled out.

As this frequently recurrent task is time-consuming and prone to mistakes, a dedicated FORTRAN application was written to set the experimental uncertainties of all assignments with an error above a user-specified threshold to zero automatically. The figure of merit for decisions on the outlier status of an assignment is the error divided by experimental uncertainty. These values are a frequency independent error measure because the uncertainties have been chosen as fixed fractions of the linewidth (see Section 4.1), which in turn scales with the frequency. Once an improved parameter set was established, ruled-out transitions could be restored easily because standard uncertainties had been used for each frequency region.

- Use a spreadsheet to copy and paste the parameter output into a comparator table and calculate the relative errors. In the comparator, the output is arranged in three columns (one for label, value and error). The relative errors are calculated in a fourth column and the columns containing the values and errors are hidden such that only the parameter identifiers, their numbers within the last fit, and their relative errors remain visible. Results from later fits are imported likewise into the columns to the right. This table allows to track the complete history of parameter responses to any changes introduced to the fit and is the basis for most decisions on further changes to the fit.
- The following steps are to be repeated for each applicable combination (q, q') in ascending Fourier order $\zeta = (|q| + |q'|)$. Centrifugal parameters can be considered as tunneling parameters with $(q, q') = (0, 0)$ and should be treated first.
- For the current pair (q, q') , add new parameters in groups of the same order (cf. Section 2.4.1) and repeat the fit. Repeat adding higher orders until no significant improvement is observed any more. At this stage, a given order is considered as an improvement of the fit if the standard deviation drops by 10% or more.
- Repeat the previous step for all other (q, q') until the standard deviation is minimised with a maximum of parameters. The

next steps are intended to filter out the smallest subset of beneficial parameters from this parameter set.

- Strongly underdetermined parameters (uncertainty $> 100\%$) can be removed immediately. If the relative uncertainties of this parameter class span more than one order of magnitude, one should however perform the removal in subclasses, starting with the greatest order of relative uncertainty, rerun the fit and proceed with the next subclass until no parameters above 100% are left before continuing with the next class. This way it is less probable that parameters will be removed accidentally because they are coupled to a bad parameter (see explanations below). When the worst parameters are removed, such coupled parameters may become well-determined rapidly.
- From now on the fit should be rerun after every major change to the parameters, which usually means an addition or removal of one or two parameters.
- Remove all remaining parameters with an uncertainty exceeding 30% . This is the threshold above which a parameter will have no significant effect on the fit any more. In rare cases, more or less well-determined parameters may exist which are acting only on the second decimal place of the standard deviation. If such a parameter is discovered (normally due to an unpredictable behaviour of its uncertainty or having index numbers which are not adjacent to those of other well-determined parameters), it can be removed likewise. The concept of adjacent parameters is explained below. A division into substeps is also advisable here if the relative uncertainties between 30% and 100% are distributed unequally.
- Some parameters are correlated to others so strongly that they will become underdetermined if one of their correlation partners is removed. During this work, parameters were regarded as coupled if their correlation index in the ERHAM output exceeded ± 80000 (cf. Section 2.4.2). Coupled parameters are known to occur in least-square algorithms if the numerical structure of the data set is pronounced too weakly to be fitted if one of the coupled parameters is removed. In algebraic

terms, coupled parameters are a weaker form of linearly dependent parameters because they still have a slight freedom of indeterminacy.

This effect is called (multi-)collinearity and has been described in the literature [7]. Collinearity should be avoided because it diminishes the integrity of the model, as an independent variation of supposedly independent parameters is no longer possible. This becomes noticeable in ERHAM primarily through a slower convergence of the least-square algorithm and disproportionate predictive uncertainties (e.g. some MHz even for assigned transitions). Proven ways to eliminate collinearity in ERHAM are comparable to what is known from systems of linear equations with linearly dependent coefficients:

- Try to identify one of the coupled parameters which fits the data set similarly well as the set of coupled parameters does. This is sufficient in the majority of cases when (mostly) parameters of high order are affected and the increase of residue due to the parameter removal is small.
- Alternatively, the coupled parameters can be kept in the parameter set until the data set is extended further. This approach is especially promising if none of the parameters in the coupled subset appears to be dispensable and further assignments are planned.
- Some cases of coupled parameters arise from other parameters having been removed from the fit too early. This case can be solved by close inspection of the comparator table to find hints when the coupling occurred for the first time.
- If persistent coupling is observed in coincidence with other general problems of the fit, this could be a hint that an important parameter might not yet have been introduced in the parameter set. This option has been used for the fit of the acetone-2-¹³C ground state successfully and will be discussed further in Section 4.3.

Decoupled parameters show an additive effect on the residue (standard deviation, see the introduction of this Section), which

can be used to obtain an indirect hint on coupling. If, for instance, the decrease in residue is known for either of two parameters if enabled alone, the residue should decrease by the sum of both effects if both parameters are enabled together. If this behaviour is not observed, an immediate localisation of the responsible parameters is possible with no further inspection of the correlation table.

- Parameters may be removed from unequal (q, q') at the same time if they are decoupled.
- In the final stages of this procedure, it is worthwhile to test if some parameters with relative uncertainties between 20% and 30% can be removed as well.
- Sometimes the situation occurs that, following this procedure, parameters of an intermediate order are removed while adjacent parameters of higher order remain in the fit and are well-determined. Two parameters pertaining to the same subset (q, q') are called adjacent if their index (κ, p, r) differs by 2 in one of the three powers κ, p, r (see Section 2.4.1). Adjacent parameters differ mainly in their order while having a comparable effect on the fit. Such “cheese holes” in the parameter set should be avoided because they destroy the monotonic convergence of the Hamiltonian. In this situation one can try to substitute the stand-alone parameter of higher order by one of its adjacent parameters of lower order. However, this is not always possible and there is no better option than accepting the “cheese hole” for the time being and continuing the procedure. Some cases have been observed where low-order tunneling parameters are not eligible because they would couple to an adjacent parameter in a different parameter subset (q, q') .

The concept of adjacent parameters is also helpful if two or more parameters seem equally eligible for being enabled, or when decoupling parameters.

- If most of the possibilities for parameter removal have been gone through, parameters may be added or removed more freely until the residue cannot be lowered further.
- After the outlier removal at the beginning of this procedure, all operations up to this point concerned only the parameters.

When the smallest possible parameter set has been determined, check the deviation summary once more for lines which have been wrongly assigned or which cannot be fit better with the current data and parameter set. These lines should be revisited with the assignment software and given zero weight if the assignment is still apparently correct.

- Go through the output of transitions and check whether lines with zero weight can be reinvoked. This is usually the case when their deviation is below one HWHM. If the procedure to minimise the parameter set was carried out correctly, there should be a substantial amount of assignments which had been weighted out from the data set at the beginning and are now described well by the revised parameter set. Cases may exist when one torsional component of a rotational transition fits well, while other assigned components still deviate strongly. In these cases it is optional to keep the well-fitting component at zero weight until a better prediction is available for all components.
- When removing a parameter from the fit, care must be taken deciding whether a parameter should be fixed to its non-zero start value or to zero. As a rule of thumb, larger parameters should be kept at their start values more likely than small ones.
- If assignments of similar transitions (i.e., transitions of one particular branch covering a small range or sequence of quantum numbers) are deviating systematically, this is a hint that there is still potential for improvements of the fit. In this case, some or all of the deviating transitions should also be incorporated to the revised data set, and parts or all of the fitting procedure should be repeated.
- If no further groups of assignments can be reinvoked and the parameters work satisfactorily, a fine tuning towards an even lower residue is often possible by revisiting some lines with the assignment software and adding and removing single parameters and transitions as required.

ERHAM does not check for convergence of the least-square loop. Especially if new data or parameters are introduced, it is advisable

to set the number of cycles (usually 2 – 3) to a high value (e.g. 30) in order to find out if the fit is really diverging or only converging slower than usual. The comparator table is useful even if the fit diverges, because it enables a quick overview of all parameters with diverging uncertainties.

As mentioned before, an important observation was made during the fit of the acetone-2-¹³C data: For the high-resolution data recorded in this work, experimental precision could only be reached when tunneling parameters were used which are not mentioned or stated as inappropriate in the literature [35]. Details about the nature of these parameters are given in Section 4.3; a verification of their irreplaceability was performed with the extended data set for the main isotopologue (Section 4.4). The use of tunneling parameters corresponding to non-tunneling operators with odd powers of angular momentum (Section 2.2), or which are forbidden in the chosen Watson-type reduction, is nonetheless justified if they improve the fit significantly because of the phenomenological nature of the ERHAM model. Tunneling parameters from one of these groups will be called *non-canonical tunneling parameters* or shortly NCTPs in the following. The use of NCTPs is considered to be in accordance with Groner’s vague statement that tunneling parameters representing unsuitable operators may be allowed in a ρ or principal axis system [35]. Choices whether to incorporate a parameter into the model were made by systematic testing and rigorous application of the following suitability criteria:

- The standard deviation drops notably, i.e., at least in the order of a few percents.
- At least the rotational and centrifugal parameters become better determined.
- One “good” parameter can play the role of several other parameters, which become ill-determined when the new parameter is introduced and can be removed from the fit. An example is seen by comparison of the first and second column of Table 4.4.
- Corrections in the choice of parameters lead to better fit results for previously poorly fit groups of lines with similar quantum numbers and selection rules.

The following sections show the results gained with this method for the ground state spectra of acetone-2-¹³C and acetone-¹²C. Fits to the frequencies observed for the acetone-1-¹³C ground state and the first excited state of the ν_{12} torsional mode of acetone-2-¹³C are also presented, but these data sets are too small to take full advantage of the described fitting procedure.

4.3 Results for acetone-2-¹³C

4.3.1 Torsional ground state

Assignments and observations

The overall goal pursued for the ground state spectrum of this species was to fit the rotational spectrum of the torsional ground state to experimental precision, or more precisely, the predictions for all lines of sufficient strength should match the observed frequencies within one HWHM. This criterion should apply at least within the boundaries of observed spectral portions above $\lambda = 2$ mm, because works on interstellar acetone to date were focused on this spectral region.

The predictions by Lovas and Groner [60] enabled first assignments of low- J, K transitions up to 130 GHz. As the measurements reported in Section 3.2 were continued, new predictions were made as soon as a satisfactory improvement of the fit was achieved. In an alternating process of measuring, assigning, fitting and predicting, the range of assigned quantum numbers was enhanced up to $J = 92$ and $K = 45$ in the final fit.

At first glance, the assignment of numerous high- J transitions seems to be unnecessary to obtain a good prediction for the desired frequency range. It appears improbable that transitions between energy levels around 1000 cm^{-1} will be observed from interstellar sources, because rotational temperatures for all acetone sources observed so far are still well below the laboratory temperature of 300 K. For comparison, Groner *et al.* had stopped assignments at $J = 60$ for the main isotopologue, which is also a good empirical upper limit for the energy levels involved in the stronger transitions around 3 mm. Yet, in the course of this work's analysis, it turned out that there were always groups of lines which could not be fit even within several multiples of one line width. The situation became better first

Table 4.1: Results of a systematic assessment of non-canonical tunneling parameters for usability in the fit for acetone-2-¹³C. See Table 4.2 for examples.

Parameter description	Observation
Purely odd κ, p, r	Allowed with the restrictions mentioned here.
Mixed even and odd κ, p, r	Allowed with the restrictions mentioned here.
$[B_{\kappa pr}]_{qq'}, \kappa < 0$	Automatically converted to $-[B_{-\kappa pr}]_{qq'}$.
$\omega = -1$	Can be tried for all parameters allowed otherwise.
$\kappa, p, r = 3, 5, \dots$	Higher odd-order parameters can be tried if a low-order adjacent parameter is well determined (uncertainty < 1%).
$[B_{\kappa 1r}]_{qq'} = -[B_{\kappa 0r}]_{qq'}$	These parameters are linearly dependent and cannot be enabled together.
Pure S -reduction parameters ($\kappa = 4, 6, \dots$)	Tested up to $\kappa = 8$ with no restrictions found.

when lines exceeding $J = 60$ were assigned above 600 GHz and the sextic centrifugal parameters became determined better. Above all, a satisfactory modeling of all reasonably strong lines and obviously correct assignments became increasingly difficult with growing diversity of assigned branches and quantum number ranges. Problems, which had gradually emerged during the data set extensions up to 365 GHz and turned out to be enduring, mainly concerned the residue, which could not be reduced below former levels after each assignment of new lines, and an inconsistency with some of the assignments by Lovas and Groner, which were not fit within several line widths any more when the parameters had been optimised for a low residue.

The working scheme pursued up to this point was to extend the parameter set by systematically exploring the effect of all allowed parameters of a given order according to the lists available from Groner [35] and Kisiel [47] after every new set of assignments. However, both lists also included examples for the declaration of NCTPs (see Section 4.2) which had not been used in earlier works for the main isotopologue [36] or the ground states of isotopologues of the structurally similar dimethyl ether [(CH₃)₂O] [21, 51, 52]. In view of the problems described – knowing that the SPFIT [80] fit for dimethyl ether’s main isotopologue indeed contains a few odd-order tunneling and non-tunneling parameters for its (10) and (01) torsionally excited states, and expecting that torsional tunneling in acetone shows enhanced coupling effects due to its lower barrier height (Chapter 1) –, it was considered worthwhile to try out some of the NCTPs.

The $\Delta K = 1$ Coriolis tunneling parameters $[g_a]_{10}$ ($= [B_{010}^-]_{10}$) and $[g_b]_{10}$ ($= [B_{001}^-]_{10}$) were added first, and it was found that they improved the fit by lowering the residue about 17% and removed the inconsistency regarding the microwave assignments. Both of them had uncertainties below 15% from the start and exceeded all other tunneling parameters in magnitude (> 0.1 MHz). This improvement encouraged a systematic evaluation of all possible definitions for NCTPs, the results of which are summarised in Table 4.1. It was found that some parameters were rejected by ERHAM or led to a diverging fit; most had no noticeable effect; but gradually a handful of useful NCTPs emerged, mainly for $(q, q') = (1, 0)$. Eventually, an accurate fit of 9760 transitions at 5922 frequencies was possible with 74 parameters and a dimensionless standard deviation of 1.20.

Found parameters are shown in Table 4.2 (“Stand-alone fit”), with the results given by Lovas and Groner shown to the left for comparison.

In his 2012 review paper [35], Groner discourages the use of tunneling parameters if their non-tunneling counterpart is not used in the fit. It was therefore tried at several stages of this work to follow his advice and fit the given data set with the restriction to enable tunneling and non-tunneling parameters only synchronously. During all of these attempts it became clear quickly that this restriction prevented a successful modeling, as the standard deviation could not be reduced below 3.0 in the best case (cf. Section 4.2). It may thus be concluded that it is advisable to make full use of the phenomenological nature of the ERHAM model, i.e., try out NCTPs, whenever canonical parameters alone are not successful to achieve a satisfactory reproduction of observed frequencies.

The successful use of NCTPs and the independent treatment of tunneling and non-tunneling parameters raises the question about their interpretation. As no non-canonical non-tunneling parameters were used, it can be concluded that the Watson-type reduced Hamiltonian describing the feedback between overall rotation and centrifugal deformation is still valid and the effects described by the additional tunneling parameters concern the torsional splitting only. With growing torsional excitation, the tunneling methyl protons encounter increasing forces, amplitudes and coupling strength before they approach free torsional rotation (cf. Section 2.3). The necessity of one Coriolis-type tunneling parameter to fit an excited-state spectrum of dimethyl ether, but not its ground-state spectrum, may reflect this circumstance. Following up on this argument, the lower torsional barrier height in acetone (251 cm^{-1} [33], compared to 950 cm^{-1} [34] for dimethyl ether) accounts for the larger number of NCTPs, and also for the larger number of tunneling parameters in total, even for the torsional ground state.

Fictitious or inertial forces in a rotating frame (the centrifugal, Coriolis, and Euler forces, see Section 2.2 for the latter) occur as soon as there is a body co-rotating or undergoing relative motion or acceleration with respect to the frame. While the (peak) centrifugal force on the internal rotors is specific to their state of torsional excitation, time-dependent Coriolis and Euler forces encountered during torsional oscillation will have an effect on the coupling of overall

and internal motion which is specific to the rotational state. It can therefore be expected that additional NCTPs describing these forces should play a role for all molecules featuring large-amplitude internal motions, but can be determined only if a high-resolution spectrum of a sufficiently high torsionally excited state (coinciding with the ground state for acetone) is fitted to experimental precision. However, it is also possible that the new parameters describe an enhanced coupling between the internal rotors and are only relevant for molecules with more than one internal rotor.

Canonical fit

An additional fit to the same data set was made without any NCTPs to gain further insight on their effect. A complete set of 106 tunneling and non-tunneling parameters up to tenth order was used to ensure the best possible convergence. Completeness of a parameter set can be easily achieved by counting through all combinations of κ , p and r (see Section 2.4.1) which are permissible within the boundaries described in [35]. If the fit converges under any subset of the complete parameter set, the presence of any further canonical parameters should not deteriorate the result significantly. A diverging fit with a complete parameter set or its convergence on a large residue can therefore be regarded as a proof that there is no parameter subset which would fit the given data set better. The canonical fit converged with a standard deviation of 13.3, which, as expected, could not be reduced any further by removing twelve underdetermined parameters. This shows that the NCTPs cannot be replaced by a set of canonical ones.

Conclusions about the effect of the NCTPs can be drawn if the lines which were not fit within one line width in the canonical fit follow any systematic behaviour. For that purpose, the deviating lines were statistically analysed in a spreadsheet. The results are shown in Figs. 4.4 and 4.5.

Table 4.2: ERHAM parameters obtained for the ground state of acetone-2- ^{13}C , in comparison to the results published so far. Superscript signs mark tunneling parameters with $\omega = -1$.

Parameter	Lovas & Groner [60]	This work	Joint fit ^c
ρ (10^{-3})	62.0740(270)	61.1812(35)	61.1517(29)
β (deg)	25.8224(33)	25.5185(93)	25.6121(26)
A (MHz)	10164.00791(76)	10164.00569(14)	10164.00561(14)
B (MHz)	8516.08462(99)	8516.083259(99)	8516.083201(98)
C (MHz)	4910.23681(74)	4910.23546(10)	4910.23548(10)
$-\Delta_J$ (kHz)	4.957000(98000)	4.852245(69)	4.852144(69)
$-\Delta_{JK}$ (kHz)	-3.08000(12000)	-3.19291(18)	-3.19293(18)
$-\Delta_K$ (kHz)	9.82900(9400)	9.85019(30)	9.85002(31)
$-\delta_J$ (kHz)	2.042000(16000)	2.038156(25)	2.038120(25)
$-\delta_K$ (kHz)	-0.61700(6100)	-0.61979(12)	-0.61967(12)
Φ_J (mHz)	50.6046 ^b	6.161(14)	6.135(14)
Φ_{JK} (mHz)	-336.741 ^b	-31.608(62)	-31.638(62)
Φ_{KJ} (mHz)	0. ^b	43.61(32)	43.74(30)
Φ_K (mHz)	423.395 ^b	23.68(35)	23.28(34)
ϕ_J (mHz)	25.3760 ^b	3.1763(69)	3.1641(68)
ϕ_{JK} (mHz)	-27.3291 ^b	37.542(68)	37.592(68)
ϕ_K (mHz)	-221.468 ^b	-76.64(19)	-76.41(18)

Continued on next page.

Table 4.2: (continued)

Parameter	Lovas & Groner [60]	Stand-alone fit	Joint fit ^c
L_{KKJ} (μHz)	--	-1.94(15)	-1.93(14)
L_K (μHz)	--	1.45(16)	1.53(15)
l_J (μHz)	--	-0.00612(51)	-0.00614(51)
l_{JK} (μHz)	--	0.2980(81)	0.2932(81)
l_{KJ} (μHz)	--	0.806(46)	0.729(44)
l_K (μHz)	--	0.778(90)	0.780(88)
Tunneling parameters			
ϵ_{10} (MHz)	-763.360(330)	-787.460(820)	-780.978(94)
ϵ_{11} (MHz)	1.049511 ^b	1.1277(63)	1.1075(58)
ϵ_{20} (MHz)	0.766643 ^b	0.6586(81)	0.6588(68)
ϵ_{1-1} (MHz)	0.0799732 ^b	0.0830(18)	0.0841(18)
$[B_{100}]_{10}$ (MHz) ^a	--	23.510(820)	17.051(94)
$[B_{\bar{1}00}]_{10}$ (MHz) ^a	--	0.0202(36)	--
$[g_a]_{10}$ (MHz) ^a	--	-1.2840(80)	-1.3182(45)
$[g_b]_{10}$ (MHz) ^a	--	0.116(15)	--
$[(B + C)/2]_{10}$ (kHz)	-18.730(330)	-7.150(270)	-5.634(93)
$[A - \frac{B+C}{2}]_{10}$ (kHz)	60.60(200)	39.77(27)	37.28(12)
$[D_{ab}]_{10}$ (kHz) ^a	--	19.09(88)	18.64(84)
$[(B - C)/4]_{10}$ (kHz)	-2.170(160)	3.820(130)	4.492(46)

Continued on next page.

Table 4.2: (continued)

Parameter	Lovas & Groner [60]	Stand-alone fit	Joint fit ^c
$[B_{030}^-]_{10}$ (Hz) ^a	--	-153.60(120)	-141.42(93)
$[B_{012}^-]_{10}$ (Hz) ^a	--	-250.3(68)	-146.0(44)
$[\Delta_J]_{10}$ (Hz)	--	16.720(150)	14.547(88)
$[\Delta_{JK}]_{10}$ (Hz)	--	-51.86(36)	-46.51(21)
$[\Delta_K]_{10}$ (Hz)	--	33.49(24)	30.39(14)
$[\delta_J]_{10}$ (Hz)	--	0.895(39)	1.134(21)
$[\delta_K]_{10}$ (Hz)	--	-18.013(92)	-17.336(62)
$[d_2]_{10}$ (Hz) ^a	--	-7.737(85)	-6.401(45)
$[B_{212}^-]_{10}$ (mHz) ^a	--	37.40(110)	16.81(67)
$[B_{032}^-]_{10}$ (mHz) ^a	--	106.6(23)	102.6(10)
$[\Phi_J]_{10}$ (mHz)	--	-0.212(19)	--
$[\Phi_{KJ}]_{10}$ (mHz)	--	1.144(89)	--
$[\Phi_K]_{10}$ (mHz)	--	-0.774(90)	0.194(24)
$[\phi_J]_{10}$ (mHz)	--	0.0742(98)	--
$[\phi_{JK}]_{10}$ (mHz)	--	0.979(56)	1.415(36)
$[\phi_K]_{10}$ (mHz)	--	-1.352(48)	-1.734(37)
$[B_{024}]_{10}$ (mHz) ^a	--	3.269(86)	2.512(19)
$[l_J]_{10}$ (μ Hz)	--	-0.02500(110)	-0.02086(66)
$[l_{JK}]_{10}$ (μ Hz)	--	0.1630(110)	0.0852(52)
$[B_{404}]_{10}$ (μ Hz) ^a	--	-0.03480(160)	-0.02893(66)

Continued on next page.

Table 4.2: (continued)

Parameter	Lovas & Groner [60]	Stand-alone fit	Joint fit ^c
$[B_{044}]_{10}$ (μHz) ^a	--	-0.2740(590)	--
$[B_{206}]_{10}$ (μHz) ^a	--	-0.01015(74)	-0.00782(42)
$[B_{026}]_{10}$ (μHz) ^a	--	-0.1750(100)	-0.1067(43)
$[(B - C)/4]_{1-1}$ (Hz)	--	26.6(27)	28.2(27)
$[B_{100}]_{20}$ (kHz) ^a	--	103.6(72)	102.0(63)
$[(B + C)/2]_{20}$ (kHz)	--	-0.133(17)	-0.194(14)
$[(B - C)/4]_{20}$ (kHz)	--	-0.263(17)	-0.210(13)
$[\Delta_J]_{20}$ (Hz)	--	0.395(22)	0.308(13)
$[\Delta_{JK}]_{20}$ (Hz)	--	-0.787(83)	-0.490(22)
$[\Delta_K]_{20}$ (Hz)	--	0.423(93)	0.328(26)
$[\delta_J]_{20}$ (Hz)	--	0.073(11)	0.077(10)
$[\delta_K]_{20}$ (Hz)	--	0.1250(300)	0.0563(97)
$[\Phi_J]_{20}$ (mHz)	--	-0.0439(37)	-0.0310(31)
$[\Phi_{JK}]_{20}$ (mHz)	--	0.281(38)	--
$[\Phi_{KJ}]_{20}$ (mHz)	--	-0.529(79)	--
$[\Phi_K]_{20}$ (mHz)	--	0.304(55)	--
$[\phi_J]_{20}$ (mHz)	--	-0.0235(21)	-0.0181(18)
$[\phi_{JK}]_{20}$ (mHz)	--	-0.121(17)	--
$[\phi_K]_{20}$ (mHz)	--	0.169(23)	--

Continued on next page.

Table 4.2: (continued)

Parameter	Lovas & Groner [60]	Stand-alone fit	Joint fit ^c
Parameters	23	74	63 ^c
Transitions fit	44	9758	9758
Lines fit	44	5922	5922
Standard deviation	0.96	1.20	1.21

^a Non-canonical and allowed odd-order tunneling parameters. See explanations in the text.

^b These parameters were kept at constant reference values from the main isotopologue.

^c Results from a joint fit with $v_{12} = 1$ data, with additional parameters separately listed in Table 4.3.

The agreement between theory and experiment is worst for medium angular momenta $J \approx 30$ to 60 [Fig. 4.4 a)]. Only few assignments were made with $J = 70$ to 79 and $J > 90$, which might explain why the agreement is significantly worse than in the preceding ranges $J = 60$ to 69 and $J = 80$ to 89. The latter ranges coincide with the prevalent values of J in the measured frequency ranges 629 – 710 GHz and 840 – 910 GHz⁵, see also the gaps in the assignments shown in Fig. 4.6.

Only a weak correlation can be figured out between the percentage of exceeding lines and the total number of assignments in a particular range of J . The increase in the fraction of deviating lines for $J = 70$ to 79 should be connected to the same circumstance, i.e., only lines in the mid- K range could be assigned for these J in the measured frequency ranges. On the contrary, this does not hold for $J > 90$, where only eight low- K lines were assigned and the high relative number of deviating lines could also be a statistical effect. Another interesting observation in Fig. 4.4 a) is the increase of deviations for $J < 10$. As can be seen in Fig. 4.6, this is the range where the asymmetry splitting is comparable or larger than the torsional splitting. A possible interpretation of the deviations in J is that the NCTPs are needed for ERHAM to correctly discern the strength of torsional and asymmetry splitting.

A clearer relation can be seen in Fig. 4.4 b): The importance of NCTPs increases with K_a ; the slight decrease in the relative number of mismatches for $K_a > 40$ may be a statistical effect. From this statistical view one cannot tell whether the deviations causing this effect accumulate at mid- K values ($K_a \approx K_c \approx J/2$) or at the “oblate end” of a series ($K_a \approx J$). For this reason the analysis was repeated with categories of the figure $\eta = \frac{K_a'' - K_c''}{J+1}$, which approaches -1 for $K_a = 0$, $K_c = J$ (oblate-like rotation, low energy) and $+1$ for $K_a = J$, $K_c = 0$ (prolate-like, high energy). It is defined in a way that resembles the asymmetry parameter ξ with interchanged prolate and oblate limiting cases, and its divisor was chosen $J+1$ instead of J to have a well-defined figure also for $J = 0$. The resulting distribution [Fig. 4.5 c)] gives evidence that transitions from levels with positive

⁵This can be estimated by noting that the unsplit $K_a = 1 \leftrightarrow 0$ P -branch transitions, which have the respective lowest frequency in each sequence of transitions of the same type with constant J'/J'' and increasing K_a , have an almost constant distance of 9810 ± 10 MHz for all $J'' > 4$.

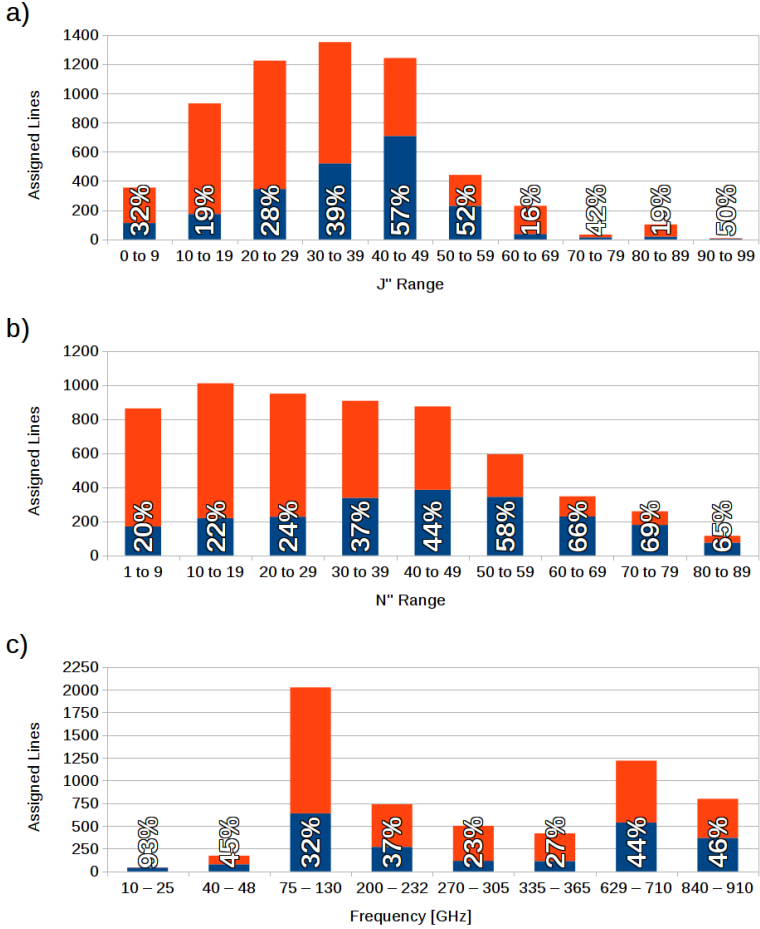


Figure 4.4: Statistical analysis of the lines exceeding 1 HWHM in a fit containing only canonical tunneling parameters. Depicted are the numbers of exceeding (blue) and matching lines (red) for different ranges of a) J ; b) N , with $K_a = N/2$ for even N or $(N-1)/2$ for odd N ; and c) frequency. As the number of assigned lines per category is subject to strong variations, the percentages of exceeding lines are given for better comparability. 5922 lines have been assigned in total.

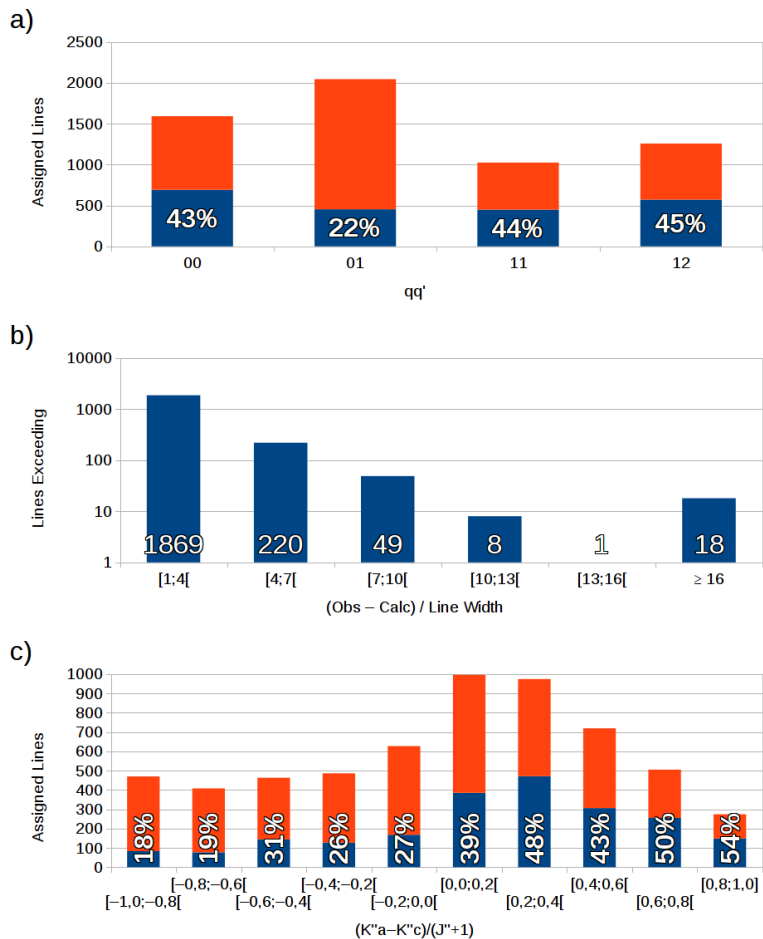


Figure 4.5: The statistical analysis of Fig. 4.4 continued. Depicted are a) the numbers of exceeding (blue) and matching lines (red) for different ranges of the four torsional line components; b) absolute numbers of lines in ranges of error ($f_{obs.} - f_{calc.}$) in multiples of the respective standard line width; and c) the distribution of mismatches for different orientations of the angular momentum vector, where transitions were counted by their lower energy level, -1 corresponds to oblate-like, and $+1$ to prolate-like rotation.

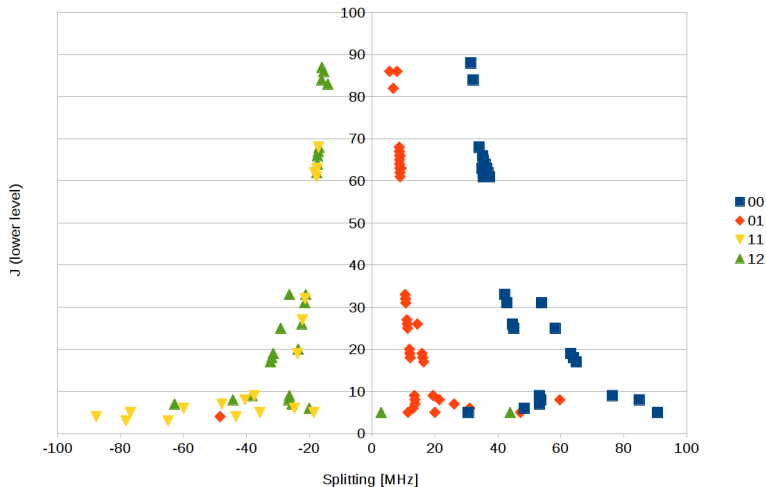


Figure 4.6: J'' dependence of the splittings of the four qq' components for assigned lines with $K_a'' = 3$, with respect to their unsplit positions as calculated by ERHAM with a standard A -reduced Watson Hamiltonian. For low J , the asymmetry splitting between transitions with $K_a + K_c = J$ and $K_a + K_c = J + 1$ becomes visible and dominates the spectrum at $J < 10$. The strongest splittings, not shown here, occur at $J'' = 3$ and reach values up to 1389 MHz.

values of η (prolate-like, high energy, large K_a) have significantly larger errors than those from lower levels. This fits the observation that, for a given series of transitions with constant J , the difficulties encountered during the assignments and fits were greatest for the respective high- K_a lines.

All frequency ranges are affected with less than half of the assigned lines (Fig. 4.6, Fig. 4.4 c), with no clear tendency noticeable except for most of the microwave lines published by Lovas and Groner [60]. With line widths of only 5 kHz, the assignments in this range are especially sensitive for deviations, which reach up to 1 MHz in this fit. Fig. 4.5 a) reveals that all torsional components except the strongest one $[(q, q') = (1, 0)]$ are affected equally. Comparison to Fig. 4.6 shows that this component is also the one with

the smallest splitting. Finally, Fig. 4.5 b) shows the number of lines within a certain distance from the calculated position, in multiples of one line width. While most lines miss the one line width criterion only closely, the number of lines deviating four line widths or more is still substantial. Especially aforementioned microwave lines reach deviations of dozens or hundreds of line widths and are predominantly included in the last column.

The statistical analysis shows no clear evidence which could yield a rationale of use for the NCTPs, which might have been the case if e.g. only one small quantum number range had been affected by a perturbation. There are, however, tendencies to be found: NCTPs improve convergence best for lines with a large splitting, regardless of its physical reason, and for transitions involving large values of K_a with respect to J , i.e., $K_a > J/2$.

Further insight into these findings may be gained with a case study of K dependences for a given J like the one for $J' = 18$ shown in Figs. 4.7 to 4.9. This set of R -branch transitions was selected because it had been showing persistent deviations, especially in the high- K_a lines, before the NCTPs were introduced. Fig. 4.7 shows the change of transition frequencies between oblate and prolate rotation. High- and low- K regions with their characteristic pairings are connected by a transition region around $K_a = (\xi + 1)J \approx 11$. In this region, the splittings of each shown transition type can change dramatically (Fig. 4.8) in an intricate, high-frequency manner which strongly differs between the transition types. The errors made by the canonical fit (Fig. 4.9) are seen to follow reasonably periodic patterns with a periodicity of $\Delta K_a \approx 8$ and larger errors coinciding with larger splittings.

Hence, the NCTPs help reproduce the observed splittings by adding K -periodic corrections to energy levels, which becomes obvious because the $(q, q') = (0, 0)$ transitions are supposed to be non-periodic in K (see eq. (2.63)). Evaluating the K -periodic part of this formula with $K = K' = K_a, q_1 = q, q_2 = q', n_1 = n_2 = n$ and $\rho_1 = \rho_2 = \rho$ yields the condition $(q + sq')_{\text{Corr}} \stackrel{!}{=} \frac{n}{\rho \Delta K}$ for an effective Fourier index pair $(q, q')_{\text{Corr}}$ which would be needed to describe the periodic correction in the canonical ERHAM formalism. With $s = -1$ (the direction cosines of the methyl rotors have different signs for all acetone isotopologues), $n = 3$ and $\rho \approx 0.0612$ in acetone-2-¹³C this condition reads $(q - q')_{\text{Corr}} = 6.127 \dots \approx 6$. The corrections

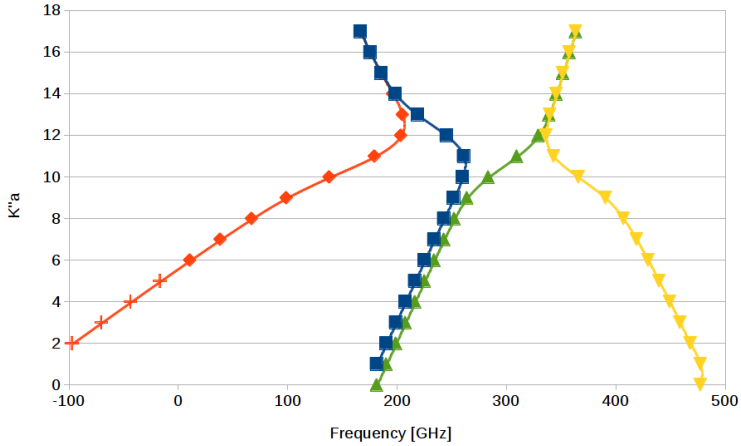


Figure 4.7: K dependence of the frequencies calculated by ERHAM for the $(\sigma_1, \sigma_2) = (0, 0)$ component of all R -branch transitions with a $J = 18$ upper level and $\Delta K_a = \pm 1$. Four types of transitions are depicted with different colours and symbols: $\Delta K_a = -1$, $K'_a + K'_c = 18$, $K''_a + K''_c = 18$ (blue squares); $\Delta K_a = -1$, $K'_a + K'_c = 19$, $K''_a + K''_c = 17$ (red lozenges); $\Delta K_a = +1$, $K'_a + K'_c = 18$, $K''_a + K''_c = 18$ (yellow tip-down triangles); $\Delta K_a = +1$, $K'_a + K'_c = 19$, $K''_a + K''_c = 17$ (green tip-up triangles). Smoothed spline curves with no physical meaning were added as a visual aid. Unphysical transitions with negative calculated frequencies are shown with “+” crosses for completeness.

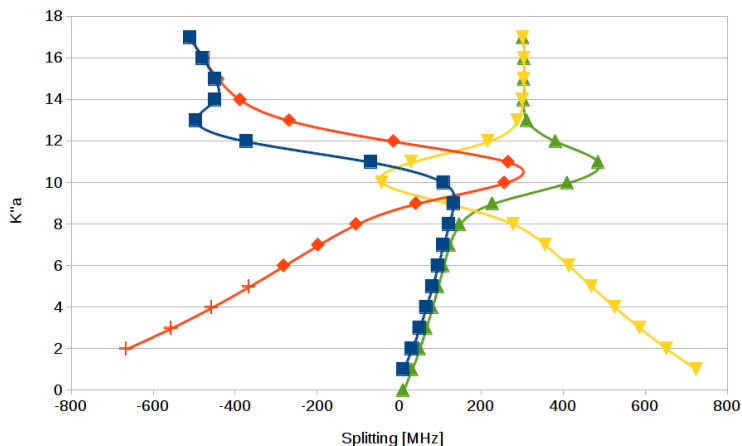


Figure 4.8: K' dependence of the splittings calculated by ERHAM for the same transitions as in Fig. 4.7. The splittings were calculated as distances from the respective theoretical unsplit positions.

derived from the case study may therefore be interpreted as additional Fourier terms of high even orders $\zeta = |q| + |q'| = 6, 8, 10, \dots$. A proof of this claim would be possible by trying to replace the NC-TPs by canonical tunneling parameters under any of the possible combinations for q and q' , but will not be pursued here due to time restrictions.

Following this interpretation, a missing part of the Fourier sum would explain why the corrections affect all quantum numbers instead of a particular range. Eventually, the ERHAM model is not falsified, but the unique combination of broadband high-resolution spectral measurements and the low torsional barrier of acetone has shown that cases may exist where the quick convergence of the ERHAM Fourier series, as is postulated in [32], is weakened in the sense that convergence is not broken, but a strictly monotonic convergence (in terms of ζ) is impeded by small contributions of higher orders.

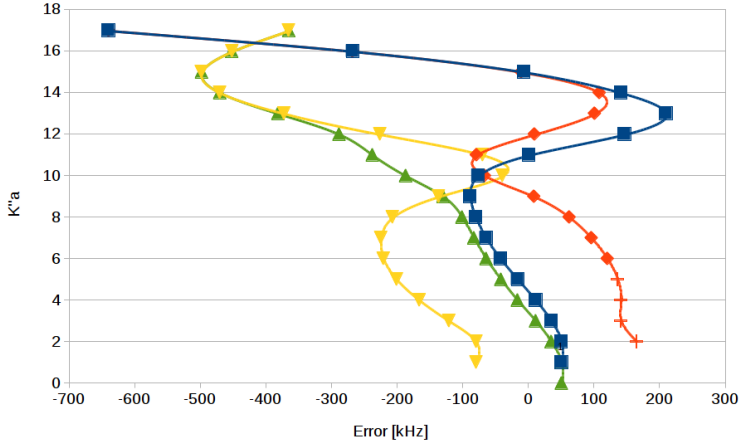


Figure 4.9: K dependence of the errors (frequency differences between the two fits with and without NCTPs) calculated by ERHAM for the same transitions as shown in Fig. 4.7.

Joint fit with $v_{12} = 1$ data

The identical set of ground-state transitions was fitted in another ERHAM calculation together with the $v_{12} = 1$ assignments reported in Section 4.3.2. The resulting parameters are also shown in Table 4.2 (“Joint fit”). Compared to the stand-alone ground-state fit, the joint fit uses eleven ground-state tunneling parameters less to fit the same data set with the same residue. The removed parameters are composed of eight sextic and three non-canonical parameters. Furthermore, the tunneling parameters often have smaller absolute values and mostly substantially smaller uncertainties. This is interpreted as the presence of excited-state data enabling ERHAM to consider, at least to some extent, inter-state coupling contributions to the splittings in a non-parametric way, which had to be expressed by tunneling parameters in the single-state fit. As the NCTPs are not affected as strongly, their role is thought to be mostly unrelated to this effect.

Continuative discussion

A rationale of use for the NCTPs used herein can be derived from their respective index classes:

- Tunneling parameters of odd order η (Section 2.4.1) or containing odd or mixed powers κ, p, r are permissible because they describe enhanced effects of inertial forces encountered by the internal rotors.
- Parameters with $\kappa > 2$ are also admissible because the A-type Watson-reduced Hamiltonian, where no equivalent non-tunneling parameters are defined, describes the centrifugal distortion of the rigid molecule rather than its internal rotors.
- Parameters with $\omega = -1$ are generally permissible, but not essential for many molecules.

An open question is to which extent NCTPs have been used earlier to fit spectra of other two-rotor molecules. The fact that Groner mentions some odd-order parameters, but at the same time expresses reservation regarding a too permissive use of obviously non-canonical parameters [35], reads like a response to earlier works, but no references are cited explicitly.

In the PhD thesis by Christian Endres [21], 9535 transitions up to $J = 59$, $K_a = 21$ from the two excited torsional states of dimethyl ether (DME) have been fit with 21 asymmetric-top rotational and centrifugal parameters up to octic order, ρ , β , and only 12 canonical tunneling parameters up to the order $\eta = 6$ for $(q, q') = (1, 0)$. In addition, a global fit made with SPFIT [80] involving the ground state and both excited states is presented where, besides a larger number of tunneling parameters up to $(q, q') = (2, 0)$, the Coriolis interaction parameters G_c and F_{ab} have been used with their respective tunneling parameters. As the torsional barrier of DME (950 cm^{-1} , [34]) is high compared to that of acetone (251 cm^{-1} , [33]), the multitude of tunneling parameters and the presence of interaction (tunneling) parameters may serve as an indicator for the torsional-rotational coupling strength. From a formal point of view, acetone, in its torsional ground state, may therefore be considered equivalent to a two-rotor molecule with a more usual barrier height, like DME, in a comparably highly excited torsional state. It may thus be predicted that presumable future ERHAM fits of such highly excited states in

other molecules must be treated in a similar way, i.e., using a large number of tunneling parameters including NCTPs.

The lacking necessity to use NCTPs for acetone in earlier works can be traced back to the fact that Groner's ^{12}C data set (1002 fit transitions) was much smaller than this work's data set for acetone- $2\text{-}^{13}\text{C}$, and mostly recorded at substantially lower resolution⁶. Under such conditions, the effects accounted for by the NCTPs are possibly too small to be seen (cf. Fig. 4.9), or could just be caught up by the canonical parameters. They become fully apparent only when a data set, which is sufficiently large and diversified in quantum numbers to get useful predictions even for high- K lines, can be built up from high-resolution, high-sensitivity, broadband measurements. If the data set is smaller, other tunneling parameters like those with $(q, q') = (1, -1)$ and $(1, 1)$ used by Lovas and Groner (Table 4.2), but which are not useful here any more, can play their role without notice.

Further inspection of Table 4.2 shows that the NCTPs consistently blend in with canonical ones of the same order η in terms of their magnitude. This work's effort of unbiasedly testing the eligibility of tunneling independently from non-tunneling parameters, non-canonical independently from canonical parameters etc. is observed here to help unfold the full use of the phenomenological nature of the ERHAM model for the benefit of preciser predictions. In particular, an application of NCTPs is suggested for all species where the spectrum cannot be easily fit with canonical parameters only, and of course in all cases where odd-order non-tunneling parameters like Coriolis interactions play a role. Retrospectively, the good agreement with observations might also have been reached with a smaller data set if non-canonical parameters had been used from the beginning.

4.3.2 First excited torsional state ($v_{12} = 1$)

During the ground state assignments reported above it was noticed that the characteristic triplet of the strong $K = 0 \leftrightarrow 1$ transitions

⁶For example, the FASSST spectrometer [79] allows for rapid BWO scanning of a spectrum around 300 GHz at the cost of a low frequency accuracy of ≈ 100 kHz. The high-resolution measurements of the same region used for this thesis had an accuracy of the order 10 Hz and were rather limited by Doppler broadening, with a typical peak-finder accuracy of less than 10 kHz.

(cf. Section 2.6) was always accompanied by one striking satellite line of only slightly lower intensity than the central line (Fig. 4.10) that was not included in the predictions. Obviously, the $(q, q') = (0, 1)$ components of the identical transitions in an excited torsional state had been found as satellite lines. From the small distance to the triplets it could further be concluded that it had to be the lower torsional mode v_{12} with $\Delta E_{12} = 77.8 \text{ cm}^{-1}$ [53]. This is further supported by the intensity ratio to the central triplet line, which should be $e^{-\Delta E_v/kT}$. For the v_{12} state and $T = 293 \text{ K}$, one would therefore expect a satellite line of 68 % intensity, whereas a satellite line from the upper torsional state ($v_{17}, 124.5 \text{ cm}^{-1}$ [37]) would be only 54% as strong as the central line. An inspection of the lines in Fig. 4.10 with the AABS peak finder yielded the intensities 1750 for the central line and 1254 for the satellite, corresponding to a ratio of 71 %. This is considered as proof for the v_{12} state; the difference of 3 % being a consequence of imprecise base line subtraction and source power variations.

As the rotational-torsional coupling in the excited states is even stronger than in the ground state (i.e., the protons tunnel with a larger amplitude and stronger anharmonicity), it is likely that the torsional splittings of the former are large compared to the latter. Hence, no further components than the (0,1) lines could be identified by searching for more satellites. A deeper analysis was deferred for time reasons. Nonetheless, all satellites to the $K = 0 \leftrightarrow 1$ triplets available in the spectral ranges covered by measurements (up to $J = 71$) were assigned as (0,1) components of the identical transitions and fit with ERHAM once as ground-state lines of a mock molecule (“Stand-alone fit” in Table 4.3) and once as an (arbitrary) excited state, extending the ground-state data set reported in Section 4.3.1 (“Joint fit” in Table 4.3). Both fits were successful: For the stand-alone fit it was sufficient to enable A, B, C, Δ_J and Φ_J to account for all ranges of J , and ρ, β and ϵ_{10} as well to include the splittings of the (0,1) components. Even a few $K = 1 \leftrightarrow 2$ satellites around 100 GHz could be added without adverse effects.

The joint fit of these lines with the ground state led to a number of effects on the parameter set with the interesting consequences discussed in Section 4.3.1. Although the numbers of transitions and parameters are small against those for the ground state, the unchanged data set could be fit here with less parameters, too. Des-

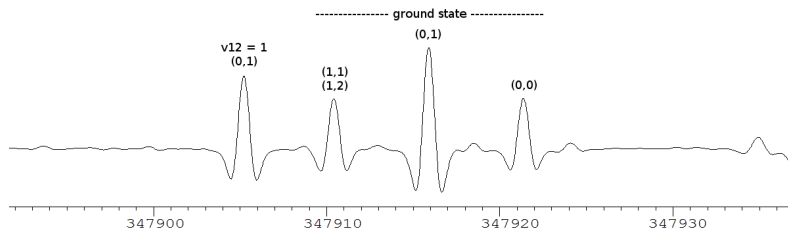


Figure 4.10: A torsional satellite accompanying the signature pattern in the acetone-2- ^{13}C spectrum, a nearly equidistant low- K triplet with intensity ratio 1:2:1. The triplet shown here is from the degenerate pair $35_{0,35} \leftarrow 34_{1,34}$ and $35_{1,35} \leftarrow 34_{0,34}$.

pite the suitability of the mock molecule parameters to fit the v_{12} lines, the larger uncertainties and often considerably different values seen in the joint fit cast doubts on the integrity of the approach to fit excited-state data with the mock ground-state parameter set of a non-existent molecule. However, the strong increase of ρ in the stand-alone fit (factor 51) can be seen as evidence for the dramatically changing dynamics already at $v = 1$.

Table 4.3: ERHAM parameters obtained for the torsionally excited state $v_{12} = 1$ of acetone-2-¹³C.

Parameter	Stand-alone fit	Joint fit ^a
ρ	3.1377900(5500)	0.0611517(29) ^b
β (deg)	47.0500(8900)	25.6121(26) ^b
A (MHz)	10035.1(31)	10131.4(47)
B (MHz)	8525.80(160)	8474.53(43)
C (MHz)	4910.1757(12)	4910.4359(73)
$-\Delta_J$ (kHz)	0.80140(65)	4.8476(100)
$-\Delta_{JK}$ (kHz)	.-	-3.19293(18) ^b
$-\Delta_K$ (kHz)	.-	9.85002(31) ^b
$-\delta_J$ (kHz)	.-	2.038120(25) ^b
$-\delta_K$ (kHz)	.-	-0.61967(12) ^b
Φ_J (mHz)	0.334(81)	6.690(100)
Φ_{JK} (mHz)	.-	-31.638(62) ^b
Φ_{KJ} (mHz)	.-	43.74(30) ^b
Φ_K (mHz)	.-	23.28(34) ^b
ϕ_J (mHz)	.-	3.1641(68) ^b
ϕ_{JK} (mHz)	.-	37.592(68) ^b
ϕ_K (mHz)	.-	-76.41(18) ^b

Tunneling parameters

ϵ_{10} (MHz)	-2381.0(330)	-4550.0(5300)
Free parameters	8	6 ^a
Transitions fit	53	53
Lines fit	30	30
Standard deviation	1.16	1.21

^a Results from a joint fit with ground-state data, with additional parameters separately listed in Table 4.2.^b These parameters are either independent from the torsional state or were kept fixed to the value of the respective ground-state parameters.

Table 4.4: Comparison of the parameters used to fit different spectroscopic data sets for acetone.

Parameter	Groner <i>et al.</i> [36]	Improved fit	Extended data set
$\rho(10^{-3})$	62.1760(60)	62.2360(380)	61.6980(110)
β (deg)	25.8322(93)	26.1990(470)	25.6039(72)
A (MHz)	10165.21654(80)	10165.21782(63)	10165.21805(29)
B (MHz)	8515.16477(65)	8515.16369(53)	8515.16351(26)
C (MHz)	4910.19903(44)	4910.19893(39)	4910.19898(22)
$-\Delta_J$ (kHz)	4.9055(25)	4.8725(20)	4.85480(23)
$-\Delta_{JK}$ (kHz)	-3.62000(1700)	-3.36900(1100)	-3.17118(64)
$-\Delta_K$ (kHz)	10.24500(1700)	10.00600(1200)	9.79130(94)
$-\delta_J$ (kHz)	2.06450(120)	2.04795(98)	2.03875(10)
$-\delta_K$ (kHz)	-0.73930(560)	-0.67990(300)	-0.60616(40)
Φ_J (Hz)	0.050600(3400)	0.030000(1800)	0.006552(75)
Φ_{JK} (Hz)	-0.33700(2000)	-0.20010(710)	-0.03117(33)
Φ_{KJ} (Hz)	-.-	-.-	0.0401(12)
Φ_K (Hz)	0.4230(200)	0.2741(55)	0.0234(15)
ϕ_J (Hz)	0.025400(1700)	0.015080(880)	0.003258(36)
ϕ_{JK} (Hz)	-0.02730(410)	-.-	0.03976(17)
ϕ_K (Hz)	-0.22150(830)	-0.16780(330)	-0.07455(62)
Tunneling parameters			
ϵ_{10} (MHz)	-763.198(62)	-764.850(180)	-764.826(41)
ϵ_{1-1} (MHz)	0.0800(83)	0.0829(58)	0.0789(25)

Continued on next page.

Table 4.4: (continued)

Parameter	Groner <i>et al.</i> [36]	Improved fit	Extended data set
ϵ_{11} (MHz)	1.0500(430)	1.0690(320)	1.0877(89)
ϵ_{20} (MHz)	0.7670(130)	0.7805(98)	0.7791(29)
$[g_a]_{10}$ (MHz) ^a	--	--	-0.327(20)
$[g_b]_{10}$ (MHz) ^a	--	0.3430(430)	-0.2985(25)
$[A - \frac{B+C}{2}]_{10}$ (kHz)	55.07(64)	85.40(190)	44.49(45)
$[\frac{B+C}{2}]_{10}$ (kHz)	-21.16(56)	-39.60(270)	-3.08(25)
$[\frac{B-C}{4}]_{10}$ (kHz)	-3.40(27)	-12.50(140)	5.84(12)
$[B_{012}]_{10}$ (kHz) ^a	--	--	-0.842(27)
$[B_{210}]_{10}$ (kHz) ^a	--	-0.3440(380)	-0.2252(96)
$[\Delta_J]_{10}$ (Hz)	39.06(34)	27.70(160)	28.98(65)
$[\Delta_{JK}]_{10}$ (Hz)	-99.8(17)	-79.9(30)	-84.4(16)
$[\Delta_K]_{10}$ (Hz)	73.7(17)	50.1(27)	54.4(12)
$[\delta_J]_{10}$ (Hz)	19.600(180)	14.000(810)	2.152(63)
$[\delta_K]_{10}$ (Hz)	-34.27(98)	-30.93(92)	-20.51(30)
$[B_{211}]_{10}$ (Hz) ^a	--	--	9.62(98)
$[d_2]_{10}$ (Hz) ^a	--	--	-12.37(34)
$[\Phi_J]_{10}$ (mHz)	--	--	-1.91(16)
$[\Phi_{JK}]_{10}$ (mHz)	--	--	5.59(45)
$[\Phi_{KJ}]_{10}$ (mHz)	--	--	-3.69(45)
$[\phi_{JK}]_{10}$ (mHz)	--	--	2.165(93)

Continued on next page.

Table 4.4: (continued)

Parameter	Groner <i>et al.</i> [36]	Improved fit	Extended data set
$[\phi_K]_{10}$ (mHz)	.-	.-	-5.42(37)
$[h_2]_{10}$ (mHz) ^a	.-	.-	0.637(85)
$[h_3]_{10}$ (mHz) ^a	.-	.-	-0.290(11)
$[B_{024}]_{10}$ (mHz) ^a	.-	.-	2.073(91)
$[B_{212}]_{10}$ (mHz) ^a	.-	.-	128.9(65)
$[A - \frac{B+C}{2}]_{1-1}$ (kHz)	1.62(25)	.-	.-
$[\frac{B+C}{2}]_{1-1}$ (kHz)	-1.43(18)	.-	.-
$[\frac{B-C}{4}]_{1-1}$ (kHz)	-0.475(73)	.-	.-
$[A - \frac{B+C}{2}]_{20}$ (kHz)	0.87(21)	.-	.-
$[\frac{B+C}{2}]_{20}$ (kHz)	-0.31(13)	.-	.-
Parameters	33	29	44
Transitions fit (total)	1000 (1175)	1000 (1175)	2219 (2254)
Lines fit	800	800	1884
Standard deviation	1.58	1.22	1.05

^a Non-canonical and allowed odd-order tunneling parameters. See explanations in Section 4.3.1.

4.4 Results for acetone-¹²C

Thanks to the work of Groner *et al.* [36], a good prediction for the low to medium K_a ranges already existed. However, a number of mid- K_a examples where the prediction was too far off to make even tentative assignments were known from high-resolution astronomy (see the figures and discussion in Chapter 5). With the new NCTP concept found for acetone-2-¹³C, it seemed likely that an improvement of the prediction is possible with merely a small effort.

The first approach was to fit the existing data set with an improved parameter set. Within one afternoon, all reasonable combinations with and without NCTPs were tried. The best fit, which showed a clearly reduced standard deviation (column “Improved fit” in Table 4.4) upon replacement of one centrifugal and five tunneling parameters by two NCTPs, was used for a new prediction. During another afternoon, the data set could be extended by more than 1200 transitions assigned in the spectra between 36 and 125 GHz (standard uncertainties 35 and 40 kHz). Assignments were possible at such a high speed because most of the already correctly predicted lines were skipped. Eventually, about one day was spent to fit this extended data set, with the results shown in the fourth column of Table 4.4. A very good agreement (dimensionless standard deviation close to 1.0) was reached for the whole data set, including all but one of the new assignments in the important 3 mm range (cf. Chapter 1). Except for ρ , the uncertainties of all former parameters could be lowered. Additionally, many lines which were assigned but not fitted by Groner *et al.* could be reassigned with a better uncertainty or reinvoked in the final fit. While the J range of assignments was not extended, the new assignments reach a maximum K_a of 34 instead of 30 before.

The extended set of transitions assigned for the main isotopologue was used to verify once more that the NCTPs introduced for acetone-2-¹³C for the first time cannot be replaced by canonical tunneling parameters. Despite its size has more than doubled, the ¹²C data set is more favourable for this task as it is faster to fit due to its smaller size (2254 transitions compared to 9758) and quantum number coverage. After removing the ten NCTPs and adding all centrifugal parameters up to eighth order; all canonical tunneling parameters for $(q, q') = (1, 0)$ up to tenth, $(1, -1)$ and $(1, 1)$ up to

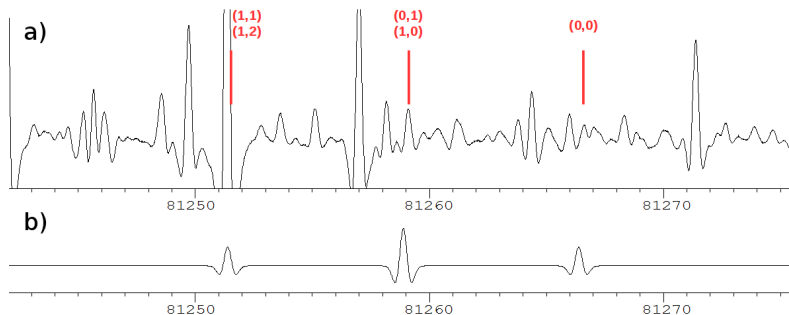


Figure 4.11: A typical situation during the assignments of acetone-1- ^{13}C lines in natural abundance. a) Measured spectrum, b) The three component lines of the degenerate transitions $8_{0/1,8} \leftarrow 7_{1/0,7}$, taken from an ERHAM prediction which was made after first tentative assignments in 2013 and contained only $K = 0 \leftrightarrow 1$ transitions. The original predictions derived from the data published by Lovas and Groner [60] were within 200 kHz from the positions indicated here. For lines which are not superposed by lines of the main isotopologue, line confusion could often be overcome by repeated cycles of assigning, fitting and predicting. The positions of the component lines as predicted after the final fit are indicated in red.

fourth, and (2, 0) up to eighth order; and for (1, 0) all canonical tunneling parameters with $\omega = -1$, the fit converged with 113 variable parameters (comparing to 44 in Table 4.4) and a standard deviation of 1.42 (1.05). In conjunction with the discussion on convergence and relevant parameter subsets presented in Section 4.2, this shows that large parts of the data set can be fit the regular way, but in a far less elegant manner and with remaining unresolvable discrepancies spanning the whole data set as shown in Section 4.3.1.

4.5 Results for acetone-1- ^{13}C

The increased experimental effort described in Section 3.4.1 made it possible to assign 63 new $K_a = 0 \leftrightarrow 1$ transitions from 17 lines. Based on the considerations in Section 4.1, standardised experimental uncertainties of 36 kHz and 70 kHz were chosen for all as-

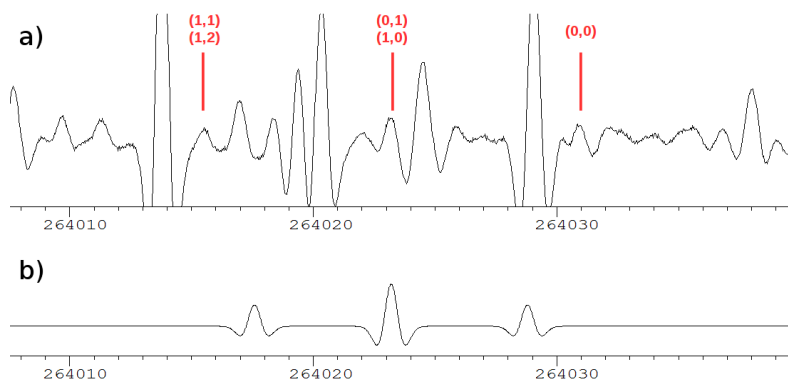


Figure 4.12: The first transition where both minor component lines could be assigned due to a lucky coincidence. a) Measured spectrum, b) The three component lines of the degenerate transitions $27_{0/1,27} \leftarrow 26_{1/0,26}$, taken from an ERHAM prediction which was made after a series of assignments in 2016 where only the central component line [(0,1) and (1,0) superposed] was to be seen in the high-sensitivity scans reported in Section 3.4.1. While no far extrapolation was needed to assign the central component, the high similarity of the two small lines indicated to the left and right of the centre was the decisive factor for an assignment which later proved to be correct.

signments in the ranges 80–130 GHz and 240–350 GHz, respectively. Two further lines below 70 GHz (36 kHz uncertainty) could be added from the broadband scans mentioned in Section 3.3. The J range has been extended up to 36.

An example which explains the difficulty of assignments in natural abundance is shown in Fig. 4.11. Strong superpositions and confusion with other lines in the dense spectrum prevented many assignments, and if possible at all, only the central superposed $(\sigma_1, \sigma_2) = (0, 1)$ and $(1, 0)$ components could be identified. However, in a handful of cases the disturbances were accidentally located in a lucky way so that also the two weaker components could be found by looking for weak lines with the same intensity and at identical shifts (with different signs) from the predicted positions (Fig. 4.12). The latter criterion could be applied only because many central lines had been assigned in an coherent series before. Sometimes a new fit had to be run after each new assignment.

As no lines were assigned with higher K , the new transitions could be fit with only few K -type parameters to account for the assignments made by Lovas and Groner. In contrast to their approach, no parameters were copied from the ground state of the main isotopologue here because their effect, if any, was not found to be beneficial. The only parameter presented as a fixed non-zero value here, δ_K , showed an adverse effect on A, B , and C at relative uncertainties between 40% and 50% when tested as a released parameter, but caused significant unresolvable deviations if fixed to zero. It was therefore fixed to the value obtained when it had been released.

As was to be expected according to the discussion in Section 4.3.1, canonical tunneling parameters up to $k = 4$ and $p, \kappa = 2$ were sufficient to fit all splittings. Three tunneling parameters for $(q, q') = (0, 1)$ were fixed to the value of the respective second-rotor parameter with $(q, q') = (1, 0)$ to prevent ERHAM from generating large artifactual splittings of opposite signs between the superposed $(\sigma_1, \sigma_2) = (0, 1)$ and $(1, 0)$ components (typically some 10 MHz) which sum up to a small combined error for the superposed line. Dimensionless standard deviations below 1.0 were achieved regularly, with the best fit for the final data set shown in column “Best fit” in Table 4.5. This result, however, was achieved with some parameters which had a relative uncertainty in excess of 30% (see the discussion in Section 4.2).

Furthermore, a too low residue may be a sign of too careless assignments, because in a dense spectrum of lines with similar intensities it is always possible to find a line matching any prediction.

Because this issue cannot be cleared with more spectroscopy in natural abundance, a second fit (“Regular fit” in Table 4.5) was generated where the 30-percent rule was strictly applied. Its resulting standard deviation of 1.01 and the fact that all microwave assignments were fitted with high precision [maximum (obs. – calc.)/unc. < 1.5] may be interpreted as a hint that the data set does not contain too many wrong assignments; on the other hand, two lines with a previously seemingly clear assignment (one of which from the (0, 1)/(1, 0) component series) could not be fit and were weighted out for the time being. Eventually, the predictions generated from the regular fit will come with more trustworthy uncertainties than those from the best fit, which might prove helpful for future assignments from the spectra to be recorded with the proposed pyrolysis experiment (Section 3.4.2).

Table 4.5: ERHAM parameters obtained for the ground-state assignments of acetone-1- ^{13}C in natural abundance.

Parameter	Lovas & Groner [60]	Best fit ^a	Regular fit
ρ_1 (10^{-3})	60.591(37)	59.792(42)	59.824(43)
ρ_2 (10^{-3})	62.047(34)	62.030(210)	62.060(110)
β_1 (deg)	29.5461(36)	29.5940(76)	29.5891(66)
$\pi - \beta_2$ (deg)	21.3035(49)	21.2632(74)	21.2630(68)
A (MHz)	10083.03470(110)	10083.03280(61)	10083.03329(65)
B (MHz)	8277.50700(130)	8277.50615(43)	8277.50610(47)
C (MHz)	4811.46920(100)	4811.46876(14)	4811.46877(16)
$-\Delta_J$ (kHz)	4.620(140)	4.546(12)	4.544(14)
$-\Delta_{JK}$ (kHz)	-2.600(140)	-2.844(69)	-2.798(76)
$-\Delta_K$ (kHz)	9.340(110)	9.506(62)	9.493(65)
$-\delta_J$ (kHz)	1.9010(210)	1.8800(63)	1.8797(71)
$-\delta_K$ (kHz)	-0.253(77)	-0.180 ^a	-0.180 ^a
Φ_J (mHz)	50.6046 ^a	.-	.-
Φ_{JK} (mHz)	-336.741 ^a	.-	.-
Φ_{KJ} (mHz)	.-	.-	.-
Φ_K (mHz)	423.395 ^a	.-	.-
ϕ_J (mHz)	25.3760 ^a	.-	.-
ϕ_{JK} (mHz)	-27.3291 ^a	.-	.-
ϕ_K (mHz)	-221.468 ^a	.-	.-

Continued on next page.

Table 4.5: (continued)

Parameter	Lovas & Groner [60]	Best fit ^a	Regular fit
Tunneling parameters			
ϵ_{10} (MHz)	-756.85(49)	-769.09(58)	-768.60(61)
ϵ_{01} (MHz)	-763.15(41)	-763.00(300)	-762.70(160)
ϵ_{1-1} (MHz)	0.0799732 ^a	0.0878(21)	0.0884(16)
ϵ_{11} (MHz)	1.049511 ^a	1.040(27)	1.071(16)
ϵ_{20} (MHz)	0.766643 ^a	-0.121 ^a	-0.121 ^a
ϵ_{02} (MHz)	0.766643 ^{ab}	0.78(22)	0.80(12)
$[A - \frac{B+C}{2}]_{10}$ (kHz)	57.8(26)	94.3(33)	91.0(36)
$[\frac{B+C}{2}]_{10}$ (kHz)	-18.25(37)	-16.54(52)	-16.59(32)
$[\frac{B-C}{4}]_{10}$ (kHz)	-2.21(18)	-1.31(26)	-1.36(16)
$[\Delta_J]_{10}$ (Hz)	--	10.032(88)	10.030(100)
$[A - \frac{B+C}{2}]_{01}$ (kHz)	57.8(26) ^b	55.0(110)	54.7(56)
$[\frac{B+C}{2}]_{01}$ (kHz)	-18.25(37) ^b	-16.54(52) ^b	-16.59(32) ^b
$[\frac{B-C}{4}]_{01}$ (kHz)	-2.21(18) ^b	-1.31(26) ^b	-1.36(16) ^b
$[\Delta_J]_{01}$ (Hz)	--	10.032(88) ^b	10.030(100) ^b
$[A - \frac{B+C}{2}]_{1-1}$ (kHz)	--	-0.24(13)	--
$[\frac{B+C}{2}]_{1-1}$ (kHz)	--	0.15(10)	--
$[\frac{B-C}{4}]_{1-1}$ (kHz)	--	0.038(30)	--

Continued on next page.

Table 4.5: (continued)

Parameter	Lovas & Groner [60]	Best fit ^a	Regular fit
$[\frac{B-C}{4}]_{11}$ (kHz)	.-	-0.071(34)	.-
$[A - \frac{B+C}{2}]_{20}$ (kHz)	.-	-7.4(13)	-6.1(13)
$[A - \frac{B+C}{2}]_{02}$ (kHz)	.-	2.2(19)	.-
Free parameters (total)	17 (30)	27 (32)	22 (27)
Transitions fit (total)	55 (55)	110 (118)	110 (118)
Lines fit (total)	55 (55)	72 (74)	72 (74)
Standard deviation	1.54	0.89	1.01

^a Parameter kept at a fixed non-zero value.

^b Parameter fixed to the value of the equivalent first-rotor parameter.

Chapter 5

Implications, summary and outlook

5.1 Related results

5.1.1 Acetone lines in an ALMA spectrum of Sagittarius B2

An early success of this work has already been achieved with the corrected spectral prediction for acetone- ^{12}C . In data from EMOCA¹, a recently published ALMA 3-mm survey of the hot-core star-forming region Sagittarius B2(N) [4, 5], several lines from the former acetone prediction by Groner *et al.* [36] with moderately high quantum numbers could not be found in the observed spectrum, although acetone was confirmed for this source from other transitions.

Fig. 5.1 shows excerpts from the spectrum of a source slightly west of Sgr B2 (N1) (positions defined in [3]), with the old (upper panel) and new (lower panel) predictions in comparison. The diagrams in this figure are a selection of those spectral portions in the observed frequency range where the differences between old and new prediction were greatest. Some lines were predicted correctly, whereas others are shifted by up to 22 MHz (left spectrum) in the improved prediction. Obviously, at the fitted overall intensity, the

¹Exploring Molecular Complexity with ALMMA

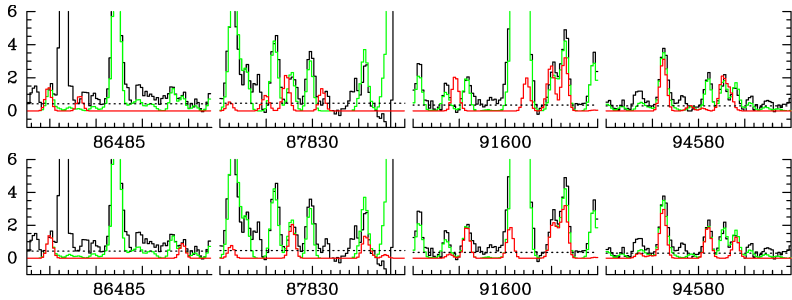


Figure 5.1: Four cases of newly identifiable acetone lines in the EMOCA survey [5] after some lines were strongly shifted in the improved prediction made from the parameters shown in Section 4.3.1. The diagrams show the observed spectrum (black) overlaid with the predicted spectrum of acetone (red; upper panel: obsolete predictions according to Groner *et al.* [36]; lower panel: new predictions) and a synthetic spectrum built from a weighted superposition of the spectra of all known species to fit the observed spectrum (green; includes only the new acetone predictions in both panels). The rest frequency in MHz at the centre of each spectral portion is given below the respective frequency axis. Small and large markings on the frequency axes are set every full 2 or 10 MHz, respectively. Images courtesy of Arnaud Belloche, Max Planck Institute for Radio Astronomy, Bonn, Germany [6].

new predictions are reproducing interstellar spectral features in all cases.

5.1.2 Dipole moment of acetone

During this thesis' works it was noticed that the value of 2.93 ± 0.03 D derived from the latest of three independent measurements [62, 78, 89] has silently grown to be accepted as the experimental value for the dipole moment. However, it should be remarked that this value has a larger experimental uncertainty than the oldest value, and that the oldest and the latest value are at the limit of mutual consistency. It is thus recommended to use the weighted average of the three independent values (2.89 ± 0.01 D) in the future.

5.2 Summary and Outlook

The greatest progress in this work was achieved for acetone-2- ^{13}C . Thanks to its commercial availability, large portions of its rotational spectrum could be recorded with high resolution and sensitivity, allowing for assignments of more than 9000 transitions. In order to obtain a precise prediction of the spectrum, at least for the frequency range up to 130 GHz, an Effective Rotational Hamiltonian was fit to its spectrum. It was shown that the fit reaches experimental precision only if the full power of the ERHAM algorithm is harnessed by allowing for non-standard configurations of the tunneling parameters. Besides allowed interaction-type tunneling parameters like g_a , which represent odd-power angular momentum dependencies of the torsional splittings, new non-canonical parameters of mixed even and odd powers or originally defined for the S reduction were found to be essential to obtain a satisfactory fit. These parameters account for an enhanced periodicity of the energy levels in K_a , which is a specialty of acetone due to its exceptionally low barrier to torsional rotation of the methyl groups and cannot be fit with canonical tunneling parameters of the usual low Fourier orders. The successful reproduction of transitions in large ranges of quantum numbers to experimental precision will allow for a detection of acetone-2- ^{13}C in the interstellar medium with the most sensitive astronomical (sub-)millimetre wave observatories.

The flexible, but accurate new concept takes the idea behind

the established ERHAM model one step further to fit the spectra of even those molecules where the coupling between large-amplitude internal torsional motion and overall rotation is especially strong. It is expected to be applicable also to molecules with a higher torsional barrier in their excited torsional states. Further evidence was gained here through its successful application to the main isotopologue, acetone- ^{12}C , whose spectrum was also measured at the Institute with the same resolution and sensitivity. Its spectrum was fit to this high experimental precision for the first time, where about 1200 transitions have been added to the data set and the parameter set was also set up with some non-canonical tunneling parameters, which cannot be omitted without gaining large errors.

The transferability of the non-canonical concept, with substantial improvements regarding fitting accuracy and work load, underlines the efficacy of the new fitting procedure presented in this thesis and the improvements which are possible if it is applied to other species in the future. The data set for acetone- $1\text{-}^{13}\text{C}$ was extended by assignments in natural abundance, but is still too small for the new concept to be applicable. An enhancement of the previous predictions for this molecule [60] was achieved nonetheless. An experiment enabling an exploration of its spectrum in the near future has been presented. Similarly, some 100 assignments have been made for the first excited state $v_{12} = 1$ of acetone- $2\text{-}^{13}\text{C}$, which could be fit together with the large set of ground-state assignments successfully.

Values for the asymmetry parameter ξ derived from the current A, B, C values are $\xi = 0.372$ for acetone- ^{12}C , $\xi = 0.315$ for acetone- $1\text{-}^{13}\text{C}$, and $\xi = 0.373$ for acetone- $2\text{-}^{13}\text{C}$.

The following list gives an overview of suggested future spectroscopy projects which are necessary to gain fully comprehensive predictions for all three isotopologues treated here.

- The acetone- ^{12}C spectrum was measured up to 908 GHz, but new assignments were made only up to 125 GHz. The remaining frequency ranges (see Section 3.3) should be screened for further erroneous predictions in the ground state.
- Based on the existing predictions made by Groner *et al.* [38, 39], it is expected that similar enhancements and improvements can be achieved for the two lowest torsionally excited states of acetone- ^{12}C .

- It is deemed possible that more lines from the $v_{12} = 1$ state of acetone-2- ^{13}C be identified by guessing positions for the other components. This may be done by generating a prediction from the parameters determined herein with additional tunneling parameters copied from the main isotopologue or acetone-2- ^{13}C .
- Vibrational satellites from the $v_{17} = 1$ state of acetone-2- ^{13}C should be apparent in the spectrum with a relative intensity of 54% and a larger splitting from the ground-state positions than those from the $v_{12} = 1$ state. It appears worthwhile to search for such satellites and repeat what was done for $v_{12} = 1$.
- The availability of spectral predictions for acetone-1- ^{13}C at a similar accuracy as that reached for acetone-2- ^{13}C would foster the astrochemical dialogue on the formation of acetone and similar complex carbon- and oxygen-bearing species. Constructing and conducting the pyrolysis experiment proposed in Section 3.4.2 to record acetone-1- ^{13}C spectra from a sample of up to 50% purity would be the first major step towards this goal. It should also be tried to use the measured ^{12}C spectra to improve the signal content from the desired isotopologue by decorrelation. Assignments, fitting and predictions should be accomplished according to the standards and procedures described here.

As a closing remark, it would be nice if a functionality was added to ERHAM where groups of strongly correlated parameters (with a correlation index above a threshold value to be set by the user) are automatically listed in a separate table.

Lists of assigned and predicted transitions for all isotopologues and torsional states treated herein will be published in peer-reviewed journals and the Cologne Database for Molecular Spectroscopy (CDMS) [68] in electronic data files.

Appendix A

Tables from the theoretical formalism

A.1 Representations of molecular coordinates

The labeling convention on the assignment of a, b, c to x, y, z axes is discussed further in [30].

Table A.1: The six possible ways to assign an x, y, z system to the inertial axes a, b, c .

	I^r	II^r	III^r	I^l	II^l	III^l
x	b	c	a	c	a	b
y	c	a	b	b	c	a
z	a	b	c	a	b	c

A.2 Character and product tables

The group C_s

Table A.2: Character table for the group C_s .

$h = 2$	E	σ_{ab}
	1	1
A'	1	1
A''	1	-1

The group C_3

The character $\epsilon = e^{2\pi i/3}$ denotes a rotation about one third of a full circle.

Table A.3: Character table for the group C_3 .

$h = 3$	E	C_3	C_3^2
	1	1	1
A	1	1	1
E_1	1	ϵ	ϵ^*
E_2	1	ϵ^*	ϵ

The groups C_{2v} and $V(a, b, c)$

Table A.4: Left: Character table for the isomorphic groups C_{2v} and $V(a, b, c)$. Middle: Corresponding even-/oddness of the asymmetric-top state subscripts K_a and K_c , and their permitted changes during the three asymmetric-top transition types. Right: Correlation to the symmetry species of G_{36} .

C_{2v}	E	C_2^b	σ_{ab}	σ_{bc}	$\mathbf{V(a, b, c)}$	$K_a K_c$	Permitted transition			G_{36}
	E	C_2^b	C_2^c	C_2^a			under type:	a	b	
$h = 4$	1	1	1	1						
A_1	1	1	1	1	A	ee	eo	oo	oe	$A_1 \oplus E_1 \oplus E_3 \oplus G$
A_2	1	1	-1	-1	B_b	oo	oe	ee	eo	$A_3 \oplus E_2 \oplus E_3 \oplus G$
B_1	1	-1	-1	1	B_a	eo	ee	oe	oo	$A_2 \oplus E_1 \oplus E_4 \oplus G$
B_2	1	-1	1	-1	B_c	oe	oo	eo	ee	$A_4 \oplus E_2 \oplus E_4 \oplus G$

The group G_{18} Table A.5: Character table for the group G_{18} .

$h = 18$	E	(123)	(456)	$(123)(456)$	$(123)(465)$	$(23)(56)^*$
	1	2	2	2	2	2
A_1	1	1	1	1	1	1
A_2	1	1	1	1	1	-1
E_1	2	-1	2	-1	-1	0
E_2	2	2	-1	-1	-1	0
E_3	2	-1	-1	2	-1	0
E_4	2	-1	-1	-1	2	0

Table A.6: Table of direct products for the group G_{18} .

	A_1	A_2	E_1	E_2	E_3	E_4
A_1	A_1	A_2	E_1	E_2	E_3	E_4
A_2	A_2	A_1	E_1	E_2	E_3	E_4
E_1	E_1	A_2	$A_1 \oplus A_2 \oplus E_1$	$E_3 \oplus E_4$	$E_2 \oplus E_4$	$E_2 \oplus E_3$
E_2	E_2	A_2	$E_3 \oplus E_4$	$A_1 \oplus A_2 \oplus E_2$	$E_1 \oplus E_4$	$E_1 \oplus E_3$
E_3	E_3	A_2	$E_2 \oplus E_4$	$E_1 \oplus E_4$	$A_1 \oplus A_2 \oplus E_3$	$E_1 \oplus E_2$
E_4	E_4	A_2	$E_2 \oplus E_3$	$E_1 \oplus E_3$	$E_1 \oplus E_2$	$A_1 \oplus A_2 \oplus E_4$

The group G_{36}

Table A.7: Character table for the group G_{36} , with the nuclear positions numbered as shown in Fig. 2.5 b).

$h = 36$	E	(132)	(123) (456)	(123) (465)	$(14)(25)$ $(36)(79)$	$(14)(26)$ $(35)(79)^*$	(142536) (79)	(142635) $(79)^*$	(23) $(56)^*$
	1	4	2	2	3	3	6	6	9
A_1	1	1	1	1	1	1	1	1	1
A_2	1	1	1	1	-1	1	-1	1	-1
A_3	1	1	1	1	1	-1	1	-1	-1
A_4	1	1	1	1	-1	-1	-1	-1	1
E_1	2	-1	2	-1	0	2	0	-1	0
E_2	2	-1	2	-1	0	-2	0	1	0
E_3	2	-1	-1	2	2	0	-1	0	0
E_4	2	-1	-1	2	-2	0	1	0	0
G	4	1	-2	-2	0	0	0	0	0

Table A.8: Table of direct products for the group G_{36} .

	A_1	A_2	A_3	A_4	E_1	E_2	E_3	E_4	G
A_1	A_1	A_2	A_3	A_4	E_1	E_2	E_3	E_4	G
A_2	A_2	A_1	A_4	A_3	E_1	E_2	E_4	E_3	G
A_3	A_3	A_4	A_1	A_2	E_2	E_1	E_3	E_4	G
A_4	A_4	A_3	A_2	A_1	E_2	E_1	E_4	E_3	G
E_1	E_1	E_1	E_2	E_2	$A_1 \oplus A_2 \oplus E_1$	$A_3 \oplus A_4 \oplus E_2$	G	G	$E_3 \oplus E_4 \oplus G$
E_2	E_2	E_2	E_1	E_1	$A_3 \oplus A_4 \oplus E_2$	$A_1 \oplus A_2 \oplus E_1$	G	G	$E_3 \oplus E_4 \oplus G$
E_3	E_3	E_4	E_3	E_4	G	G	$A_1 \oplus A_3 \oplus E_3$	$A_2 \oplus A_4 \oplus E_4$	$E_1 \oplus E_2 \oplus G$
E_4	E_4	E_3	E_4	E_3	G	G	$A_2 \oplus A_4 \oplus E_4$	$A_1 \oplus A_3 \oplus E_3$	$E_1 \oplus E_2 \oplus G$
G	G	G	G	G	$E_3 \oplus E_4 \oplus G$	$E_3 \oplus E_4 \oplus G$	$E_1 \oplus E_2 \oplus G$	$E_1 \oplus E_2 \oplus G$	$A_1 \oplus A_2 \oplus A_3 \oplus A_4$ $\oplus E_1 \oplus E_2 \oplus E_3 \oplus E_4 \oplus G$

A.3 Correlation tables

The rotational sense of each internal rotor can be expressed with the labels of the symmetry species of the respective MS group, and independently with the symmetry numbers σ_1, σ_2 introduced in Section 2.3. This correspondence provides the link to identify the symmetry-based selection rules derived in Section 2.5 with the rovibrational and internal states of the molecule.

Table A.9: Correlation between internal rotation, symmetry labels and symmetry species for acetone-1- ^{13}C , based on the coordinate conventions discussed in [74].

Top 1	Top 2	Degeneracy	(σ_1, σ_2)	G_{18}
–	–	1	(0, 0)	A_1, A_2
cw/ccw	–	2	$(\pm 1, 0)$	E_1
–	cw/ccw	2	$(0, \pm 1)$	E_2
cw/ccw	cw/ccw	2	$(\pm 1, \pm 1)$ in phase	E_4
cw/ccw	ccw/cw	2	$(\pm 1, \mp 1)$ out of phase	E_3

Table A.10: Correlation between internal rotation, symmetry labels and symmetry species for acetone- ^{12}C and acetone-2- ^{13}C . The assignment of the E species is read off the character table A.7 in an analogous manner as is done for G_{18} . An in-depth discussion of symmetry for the internal motion problem of acetone, based on a product group which is isomorphic to G_{36} , is found in [72].

Top 1	Top 2	Degeneracy	(σ_1, σ_2)	G_{36}
—	—	1	$(0, 0)$	A_1, A_2, A_3, A_4
cw/ccw	—	2	$(\pm 1, 0)$	G
—	cw/ccw	2	$(0, \pm 1)$	
			equivalent	
cw/ccw	cw/ccw	2	$(\pm 1, \pm 1)$ in phase	E_3, E_4
cw/ccw	ccw/cw	2	$(\pm 1, \mp 1)$ out of phase	E_1, E_2

Appendix B

Manufacturers and models of major laboratory devices and equipment

- Synthesizers:
 - Agilent E8257D, $f \leq 70$ GHz
 - Rohde & Schwarz SMF 100A, $f \leq 43.5$ GHz
- AMETEK Signal Recovery / EG&G Instruments 7260 DSP lock-in amplifiers
- Virginia Diodes amplifier-multiplier chains (AMCs):
 - AMC-S179 (75–130 GHz)
 - AMC-S206 (200–232 GHz)
 - AMC-405 “Starter Kit” (exchangeable modules, coverage 82.5–1,100 GHz)
- Liquid helium cooled InSb bolometers with dedicated low-noise amplifiers made by the manufacturer QMC
- “Model 109” frequency selective amplifiers
- Waveguide-mounted superlattice multipliers. These devices were developed and kindly provided to the Institute by Dr. Dmitriy Paveliev (Electronics Department, Lobachevsky State

University of Nizhny Novgorod, Russia). Their design and operating principle is described in [76], and their use in a sub-mm absorption spectrometer is demonstrated in [21].

- Bespoke parts and equipment designed and built at the Institute
 - Low-noise analogue amplifier–bias boxes (see Fig. 3.1)
 - Schottky diodes (see Fig. 3.1)
 - 345-GHz diagonal antennas [46] designed and assembled from half parts by the author
 - PTFE absorption cell windows (see Fig. 3.3)
 - HDPE lenses (diameter ≤ 100 mm)
 - Large-area millimetre-wave beam splitters (see Fig. 3.4)

Bibliography

- [1] F. Arnold *et al.*, *Observation of upper tropospheric sulfur dioxide- and acetone pollution: Potential implications for hydroxyl radical and aerosol formation*, *Geophys. Res. Lett.* **24** (1997), no. 1, 57–60.
- [2] B. Bak *et al.*, *Microwave Absorption of Some Organic Vapors*, *Phys. Rev.* **75** (1949), 1622–1623.
- [3] A. Belloche *et al.*, *Detection of amino acetonitrile in Sgr B2(N)*, *Astron. Astrophys.* **482** (2008), no. 1.
- [4] ———, *Detection of a branched alkyl molecule in the interstellar medium: iso-propyl cyanide*, *Science* **345** (2014), no. 6204, 1584–1587.
- [5] ———, *EMoCA: Exploring Molecular Complexity with ALMA*, *Revolution in Astronomy with ALMA: The Third Year*. Proceedings of a Conference held at the Tokyo International Forum, Tokyo, Japan 8–11 December 2014, ASP Conference Series, vol. 499, Astronomical Society of the Pacific, San Francisco, 2015.
- [6] A. Belloche. Private communication.
- [7] D. A. Belsley, E. Kuh, and R. E. Welsch, *Regression Diagnostics: Identifying Influential Data and Sources of Collinearity*, Wiley, New York, 1980.
- [8] P. D. Brown *et al.*, *A model of the chemistry in hot molecular cores*, *Mon. Not. R. Astron. Soc.* **231** (1988), 409–417.
- [9] P. R. Bunker and P. Jensen, *Molecular Symmetry and Spectroscopy*, NRC Research Press, Ottawa, 1998.
- [10] ———, *Fundamentals of Molecular Symmetry*, Institute of Physics Publishing, Bristol, 2005.
- [11] S. Cazaux *et al.*, *The Hot Core around the Low-mass Protostar IRAS 16293-2422: Scoundrels Rule!*, *Astrophys. J.* **593** (2002), L51–L55.
- [12] C. Codella *et al.*, *SiO collimated outflows driven by high-mass YSOs in G24.78+0.08*, *Astron. Astrophys.* **550** (2013), A81.
- [13] F. Combes *et al.*, *Acetone in interstellar space*, *Astron. Astrophys.* **180** (1987), L13–L16.
- [14] P. Cossee and J. H. Schachtschneider, *Vibrational Analysis of Acetone, Acetaldehyde, and Formaldehyde*, *J. Chem. Phys.* **44** (1944), 97–111.

- [15] T. de Graauw *et al.*, *The Herschel-Heterodyne Instrument for the Far-Infrared (HIFI): instrument and pre-launch testing*, Space Telescopes and Instrumentation 2008: Optical, Infrared, and Millimeter (Marseille, France, 2008).
- [16] F. C. de Lucia, *The submillimeter: A spectroscopist's view*, J. Mol. Spectrosc. **261** (2010), 1–17.
- [17] M. de Reus *et al.*, *On the relationship between acetone and carbon monoxide in different air masses*, Atmos. Chem. Phys. **3** (2003), 1709–1723.
- [18] M. J. S. Dewar *et al.*, *AM1: A General Purpose Quantum Mechanical Molecular Model*, J. Am. Chem. Soc. **44** (1985), no. 107, 3902–3909.
- [19] J. E. Elsila *et al.*, *Cometary glycine detected in samples returned by Stardust*, Meteor. Planet. Sci. **44** (2009), no. 9, 1323–1330.
- [20] ———, *Compound-specific carbon, nitrogen, and hydrogen isotopic ratios for amino acids in CM and CR chondrites and their use in evaluating potential formation pathways*, Meteor. Planet. Sci. **47** (2012), no. 9, 1517–1536.
- [21] C. P. Endres, *Terahertz Spectroscopy of Dimethyl Ether*, PhD thesis, University of Cologne, 2009.
- [22] D. N. Friedel and S. L. Widicus Weaver, *Complex organic molecules at high spatial resolution toward Orion-KL: II. Kinematics*, Astrophys. J. Suppl. Ser. **201** (2012), no. 17.
- [23] D. N. Friedel *et al.*, *Detection of interstellar acetone toward the Orion-KL hot core*, Astrophys. J. **632** (2005), L95–L98.
- [24] R. T. Garrod *et al.*, *Complex chemistry in star-forming regions: An expanded gas-grain warm-up chemical model*, Astrophys. J. **682** (2008), 283–302.
- [25] *GESTIS database of hazardous substances. Information system on hazardous substances of the German Social Accident Insurance*, <http://www.dguv.de/ifa/gestis-database>.
- [26] E. L. Gibb *et al.*, *Interstellar Ice: The Infrared Space Observatory Legacy*, Astrophys. J. Suppl. Ser. **151** (2004), 35.
- [27] S. C. O. Glover and P. C. Clark, *Is molecular gas necessary for star formation?*, Mon. Not. R. Astron. Soc. **421** (2012), 9–19.
- [28] C. Goddi *et al.*, *A 42.3–43.6 GHz spectral survey of Orion BN/KL: First detection of the $v = 0J = 1 - -0$ line from the isotopologues ^{29}SiO and ^{30}SiO* , Astrophys. J. **691** (2009), 1254–1264.
- [29] P. F. Goldsmith, *Quasioptical systems: Gaussian beam quasioptical propagation and applications*, IEEE Press, New York, 1998.
- [30] W. Gordy and R. L. Cook, *Microwave Molecular Spectra*, John Wiley & Sons, New York, 1984.
- [31] P. Groner, *Large-amplitude motion tunneling parameters in effective rotational Hamiltonians from rotation-internal rotation theory*, J. Mol. Spectrosc. **156** (1992), 164–189.
- [32] ———, *Effective rotational Hamiltonian for molecules with two periodic large-amplitude motions*, J. Chem. Phys. **107** (1997), 4483–4498.

- [33] ———, *Experimental two-dimensional torsional potential function for the methyl internal rotors in acetone*, J. Mol. Struct. **550–551** (2000), 473–479.
- [34] P. Groner and J. R. Durig, *Analysis of torsional spectra of molecules with two internal C_{3v} rotors: II. Far infrared and low frequency Raman spectra of dimethylether isotopes*, J. Chem. Phys. **66** (1977), 1856–1874.
- [35] P. Groner *et al.*, *Effective rotational Hamiltonian for molecules with internal rotors: Principles, theory, applications and experiences*, ApJS **142** (2002), 145–151.
- [36] ———, *Acetone: Laboratory assignments and predictions through 620 GHz for the vibrational-torsional ground state*, J. Mol. Spectrosc. **278** (2012), 52–67.
- [37] ———, *Analysis of torsional spectra of molecules with two internal C_{3v} rotors: XXIV. High resolution far infrared spectra of acetone- d_0 , - d_3 , and - d_6* , J. Chem. Phys. **86** (1987), 565–568.
- [38] ———, *Rotational spectrum of acetone, CH_3COCH_3 , in the first torsional excited state*, J. Mol. Struct. **795** (2006), 173–178.
- [39] ———, *Rotational spectrum of acetone, CH_3COCH_3 , in the ν_{17} torsional excited state*, J. Mol. Spectrosc. **251** (2008), 180–184.
- [40] E. Herbst *et al.*, *Is interstellar acetone produced by ion-molecule chemistry?*, Astrophys. J. **358** (1990), 468–472.
- [41] E. Herbst and E. F. van Dishoeck, *Complex Organic Interstellar Molecules*, Annu. Rev. Astron. Astrophys. **47** (2009), 427–480.
- [42] S. Heyminck *et al.*, *GREAT: the SOFIA high-frequency heterodyne instrument*, Astron. Astrophys. **542** (2012), no. L1.
- [43] E. Hugo *et al.*, *$H_3^+ + H_2$ isotopic system at low temperatures: Microcanonical model and experimental study*, J. Chem. Phys. **130** (2009), no. 164302.
- [44] V. V. Ilyushin and J. T. Hougen, *A fitting program for molecules with two equivalent methyl tops and C_{2v} point-group symmetry at equilibrium: Application to existing microwave, millimeter, and sub-millimeter wave measurements of acetone*, J. Mol. Spectrosc. **289** (2013), 41–49.
- [45] W. M. Irvine and R. F. Knacke, *The chemistry of interstellar gas and grains*, Origin and Evolution of Planetary and Satellite Atmospheres, 1989, pp. 3–34.
- [46] J. F. Johansson *et al.*, *Antennas for sub-millimetre wave receivers*, Second International Symposium on Space Terahertz Technology, 1991, pp. 63–81.
- [47] Z. Kisiel, *PROSPE – Programs for rotational spectroscopy*, <http://www.ifpan.edu.pl/~kisiel/prospe.htm>.
- [48] Z. Kisiel *et al.*, *Rotational spectrum of trans–trans diethyl ether in the ground and three excited vibrational states*, J. Mol. Spectrosc. **233** (2005), 231–243.
- [49] ———, *Broadband rotational spectroscopy of acrylonitrile: Vibrational energies from perturbations*, J. Mol. Spectrosc. **280** (2012), 134–144.

- [50] Z. Kisiel and L. Pszczółkowski, *The Millimeter-Wave Rotational Spectrum of Chloroacetonitrile*, J. Mol. Spectrosc. **158** (1993), 318–327.
- [51] M. Koerber, *The rotational spectrum of oxatrisulfane and dimethyl ether ^{13}C isotopologues*, PhD thesis, University of Cologne, 2012.
- [52] M. Koerber *et al.*, *Laboratory rotational spectra of the dimethyl ether ^{13}C -isotopologues up to 1.5 THz*, Astron. Astrophys. **558** (2013), A112.
- [53] T. Kundu *et al.*, *Methyl rotor effects on acetone Rydberg spectra. I. The $^1\text{A}_2(3p \leftarrow n) \leftarrow ^1\text{A}_1$ transition*, J. Chem. Phys. **97** (1992), 5410–5416.
- [54] K. Kvenvolden *et al.*, *Evidence for Extraterrestrial Amino-acids and Hydrocarbons in the Murchison Meteorite*, Nature **228** (1970), 923–926.
- [55] W. D. Langer *et al.*, *Carbon and oxygen isotope fractionation in dense interstellar clouds*, Astrophys. J. **277** (1984), 581–604.
- [56] S. M. Lederle, *Heterofermentative Acetonproduktion*, PhD thesis, University of Ulm, 2010 (German).
- [57] F. Lewen *et al.*, *Phase locked backward wave oscillator pulsed beam spectrometer in the submillimeter wave range*, Rev. Sci. Instrum. **69** (1998), 32 – 39.
- [58] A. Libavius, *Commentariorum alchymiae Andreae Libavii med. d. pars . . .*, Frankfurt am Main, 1606 (Latin).
- [59] C. C. Lin and J. D. Swalen, *Internal Rotation and Microwave Spectroscopy*, Rev. Mod. Phys. **31** (1959), no. 4, 841–892.
- [60] F. J. Lovas and P. Groner, *Microwave spectra of mono- ^{13}C substituted acetone, $(\text{CH}_3)_2\text{CO}$* , J. Mol. Spectrosc. **236** (2006), 173–177.
- [61] R. H. Mann and W. B. Dixon, *Comprehensive Urey-Bradley Force Field for Molecules with Geminal Methyl Groups: I. Acetone*, J. Chem. Phys. **57** (1972), no. 2, 792–802.
- [62] A. A. Maryott and F. Buckley, *Table of Dielectric Constants and Electric Dipole Moments of Substances in the Gaseous State*, Circ. Bur. Standards **537** (1953).
- [63] F. Merkt, *Molecules in high Rydberg states*, Annu. Rev. Phys. Chem. (1997), 675–709.
- [64] T. J. Millar, *Deuterium in interstellar clouds*, Astron. Geophys. **46** (2005), 2.29–2.32.
- [65] M. Mladenović and E. Roueff, *Ion-molecule reactions involving HCO^+ and N_2H^+ : Isotopologue equilibria from new theoretical calculations and consequences for interstellar isotope fractionation*, Astron. Astrophys. **566** (2014), no. A144.
- [66] *Model 7265 DSP Lock-in Amplifier: Instruction Manual*, AMETEK Advanced Measurement Technology Inc., Oak Ridge, Tennessee, 2002.
- [67] *Molecular spectral line catalogue of the NASA Jet Propulsion Laboratory*, <http://spec.jpl.nasa.gov>.
- [68] H. S. P. Müller, *Cologne Database for Molecular Spectroscopy*, <http://www.astro.uni-koeln.de/cdms/>.

- [69] H. S. P. Müller *et al.*, *The Cologne Database for Molecular Spectroscopy, CDMS*, *Astron. Astrophys.* **370** (2001), L49–L52.
- [70] ———, *The Cologne Database for Molecular Spectroscopy, CDMS: a useful tool for astronomers and spectroscopists*, *J. Mol. Struct.* **742** (2005), 215–227.
- [71] ———, *The CDMS view on molecular data needs of Herschel, SOFIA, and ALMA*, *AIP Conf. Proc.* **1545** (2013), 96–109.
- [72] R. J. Myers and E. B. Wilson Jr., *Application of Symmetry Principles to the Rotation-Internal Torsion Levels of Molecules with Two Equivalent Methyl Groups*, *J. Chem. Phys.* **33** (1960), 186–191.
- [73] O. Neunhoeffer and P. Paschke, *Über den Mechanismus der Ketonbildung aus Carbonsäuren*, *Chemische Berichte* **72** (1939), 919–929 (German).
- [74] N. Ohashi *et al.*, *Analysis and fit of the Fourier-transform microwave spectrum of the two-top molecule N-methylacetamide*, *J. Mol. Spectrosc.* **227** (2004), 28–42.
- [75] M. H. Ordu, *Rotationspektroskopie von n-Butylcyanid*, Diploma thesis, University of Cologne, 2011 (German).
- [76] D. G. Paveliev *et al.*, *Experimental Study of Frequency Multipliers Based on a GaAs/AlAs Semiconductor Superlattices [sic] in the Terahertz Frequency Range*, *Semiconductors* **46** (2012), 121–125.
- [77] T.-C. Peng *et al.*, *Acetone in Orion BN/KL: High-resolution maps of a special oxygen-bearing molecule*, *Astron. Astrophys.* **554** (2013), A78.
- [78] R. Peter and H. Dreizler, *Das Mikrowellenspektrum von Aceton im Torsionsgrundzustand*, *Z. Naturforsch.* **20 a** (1965), 301–312 (German).
- [79] D. T. Petkie *et al.*, *A fast scan submillimeter spectroscopic technique*, *Rev. Sci. Instrum.* **68** (1997), 1675.
- [80] H. M. Pickett, *The Fitting and Prediction of Vibration-Rotation Spectra with Spin Interactions*, *J. Mol. Spectrosc.* **148** (1991), 371 – 377, available at <http://spec.jpl.nasa.gov/ftp/pub/calpgm/>.
- [81] H. M. Pickett *et al.*, *Characterisation of a dual-mode horn for submillimetre wavelengths*, *IEEE Trans. Microwave Theory Tech.* **32** (1984), no. 8, 936–937.
- [82] ———, *Submillimeter, Millimeter, and Microwave Spectral Line Catalog*, *J. Quant. Spectrosc. Radiat. Transfer* **60** (1998), 883–890.
- [83] Renate90, *Herstellung von Aceton V2.svg* (May 18, 2015), https://commons.wikimedia.org/w/index.php?title=File:Herstellung_von_Aceton_V2.svg&oldid=161047107.
- [84] J. Rong *et al.*, *Complex molecules in the W51 North region*, *Mon. Not. R. Astron. Soc.* **455** (2016), 1428–1437.
- [85] E. Roueff *et al.*, *Isotopic fractionation of carbon, deuterium, and nitrogen: a full chemical study*, *Astron. Astrophys.* **576** (2015), no. A99.
- [86] D. W. Savin *et al.*, *The impact of recent advances in laboratory astrophysics on our understanding of the cosmos*, *Rep. Prog. Phys.* **75** (2012), 036901.

- [87] L. E. Snyder *et al.*, *A Rigorous Attempt to Verify Interstellar Glycine*, *Astrophys. J.* **619** (2005), no. 2.
- [88] ———, *Confirmation of interstellar acetone*, *Astrophys. J.* **578** (2002), 245–255.
- [89] J. D. Swalen and C. C. Costain, *Internal Rotation in Molecules with Two Internal Rotors: Microwave Spectrum of Acetone*, *J. Chem. Phys.* **31** (1959), no. 6, 1562–1574.
- [90] B. Tercero, J. Cernicharo, J. R. Pardo, and J. R. Goicoechea, *A line confusion limited millimeter survey of Orion KL*. Details about this survey have not been published yet. It was only reported on several conference posters, e.g. as poster session 2: poster 93 at the 280th IAU Symposium (2011) or as poster session 2: poster 57 at the 231st IAU Symposium (2005).
- [91] M. Thompson, *ArgusLab*, <http://www.arguslab.com>.
- [92] A. G. G. M. Tielens, *The Physics and Chemistry of the Interstellar Medium*, Cambridge University Press, Cambridge, 2005.
- [93] C. H. Townes and A. L. Schawlow, *Microwave Spectroscopy*, Dover Publications, New York, 1975.
- [94] B. E. Turner, *Recent progress in astrochemistry*, *Space Sci. Rev.* **118** (1986), 355–362.
- [95] J. M. Vacherand *et al.*, *The Rotational Spectrum of Acetone: Internal Rotation and Centrifugal Distortion Analysis*, *J. Mol. Spectrosc.* **118** (1986), 355–362.
- [96] K. P. C. Vollhardt and N. E. Schore, *Organic Chemistry, Structure and Function*, 3rd ed., W. H. Freeman and Co., New York, 1999.
- [97] J. K. G. Watson, *Determination of Centrifugal Distortion Coefficients of Asymmetric-Top Molecules*, *J. Chem. Phys.* **46** (1967), 1935.
- [98] W. D. Watson, *Interstellar molecule reactions*, *Rev. Mod. Phys.* **48** (1976), no. 4, 513–553.
- [99] W. D. Watson *et al.*, *Measurement and significance of the reaction $^{13}\text{C}^+ + ^{12}\text{CO} \rightleftharpoons ^{12}\text{C}^+ + ^{13}\text{CO}$ for alteration of the $^{13}\text{C}/^{12}\text{C}$ ratio in interstellar molecules*, *Astrophys. J.* **205** (1976), L165–L168.
- [100] S. L. Widicus Weaver and D. N. Friedel, *Complex organic molecules at high spatial resolution toward Orion-KL: I. Spatial scales*, *Astrophys. J. Suppl. Ser.* **201** (2012), no. 16.
- [101] B. Winnewisser *et al.*, *An array of scarlet and grey booklets: 65 years of the Symposium on Molecular Spectroscopy*, *J. Mol. Spectrosc.* **269** (2011), 2–11.
- [102] E. S. Wirström *et al.*, *Observations of carbon isotopic fractionation in interstellar formaldehyde*, *Lunar and Planetary Science Conference* **43** (2012), no. 1611.
- [103] A. Wollrab, *Organische Chemie*, 4th ed., Springer-Verlag, Berlin, 2014 (German).

Danksagung

So lange ich für diese Arbeit am Rechner gesessen habe, so war ich doch niemals allein. Daher möchte ich an dieser Stelle all jenen danken, die mich die ganzen Jahre über begleitet haben und ohne die diese Doktorarbeit nie möglich gewesen wäre.

- Mein Dank gebührt an erster Stelle meinem Betreuer **Prof. Dr. Stephan Schlemmer** für das reizvolle Forschungsthema und die Gelegenheit, im Umfeld eines herausragenden Spektroskopielabors und eines wunderbaren Teams mein Können an einem der „großen“ Moleküle unter Beweis zu stellen.
- **Dr. Frank Lewen** – der Mann, ohne den es einfach nicht geht. Der Beduine, der im trockensten Staub der Nüchternheit nicht untergeht! Ein großes Dankeschön für die unzähligen Stunden des Wissenstransfers, der tatkräftigen Unterstützung im Labor, bei der Auswertung und der Niederschrift, für das Korrekturlesen des Experimental- und Analyseteils sowie das größte Repertoire an Lach- und Sachgeschichten, das mir in den letzten zehn Jahren begegnet ist!
- Ich danke ebenso **Dr. Holger Müller**, für sein jederzeit offenes Ohr zu allen Fragen, Sorgen und Nöten aus dem Bereich der numerischen Anpassung, allerlei hilf- und lehrreiche Kommentare aus der Welt der Spektroskopie und wissenschaftlichen Publizistik und sein gleich bleibendes Interesse an meiner Arbeit.
- Allen anderen aktuellen und ehemaligen Mitgliedern der Kölner Spektroskopiegruppe, die mit ihrer guten Laune und einer

gehörigen Portion „Geht nicht gibt's nicht“ immer wieder dafür gesorgt haben, dass die Arbeit Spaß macht und der Laden läuft. Es sind besonders hervorzuheben:

- **Dr. Monika Koerber** und **Dr. Christian Endres** für ihre einführende Unterstützung bei der Arbeit mit ERHAM und AABS. Danke, Monika, für die vielen freundschaftlichen Gespräche zwischendurch.
- **Dr. Sandra Brünken, Dr. Nadine Wehres** und **Hanno Schmiedt** für blitzschnelles Korrekturlesen.
- **Prof. Dr. Joachim Hemberger** danke ich für die unkomplizierte Übernahme des Zweitgutachtens, **Prof. Dr. Stefanie Walch-Gassner** für den Vorsitz der Prüfungskommission sowie abermals **Dr. Frank Lewen** für den Beisitz.
- Einigen Kolleginnen und Kollegen aus dem Kölner Department für Chemie gebührt Dank für ihre Unterstützung und Beratung auf dem Weg zum perfekten Experiment zur Synthese von Aceton-1-¹³C:
 - **Prof. Dr. Uwe Ruschewitz**, der mir freundlicherweise seinen Rohofen zur Verfügung gestellt hat, und seinen Studierenden **Stefanie Busch, Verena Gramm** und **Christian Tobeck** für die Realisierung der ersten ¹²C-Acetatprobe und das umfangreiche zur Verfügung gestellte Material.
 - **Priv.-Doz. Mathias Schäfer** für seine kritische Prüfung meines Vorhabens und die freundliche Vermittlung.
 - **Prof. Dr. Axel Klein** und einigen seiner Doktoranden für den Syntheserversuch per Grignard-Reaktion.
- Ein herzliches Dankeschön geht ebenfalls an **Dr. Arnaud Belloche** vom Bonner Max-Planck-Institut für Radioastronomie für die vielen zur Verfügung gestellten ALMA-Diagramme, die Präsentation seines SFB-Talks 2014 und die gute und freundliche Zusammenarbeit.
- **Dr. Peter Groner** danke ich für die zugesendeten ERHAM-Input-Dateien.

- **Mirko Schäfer** sei für die Übernahme der 40-GHz-Messungen während meiner Elternzeit 2012 gedankt.

Es gibt sogar einige Leute, die mir durch ihre Arbeit indirekt sehr weitergeholfen haben, ohne dass ich sie wirklich kenne.

- **Zbigniew Kisiel**, whose web site “PROSPE” [47] was a helpful data and information portal through all the years.
- A big thank you goes to the community of **Wikipedia authors** for providing me hundreds of insights from myriads of searchable details in the same place. The critical hint to an alternative synthesis path for acetone came from the German Wikipedia article!
- Likewise, large parts of the software that was used as a base for most of the texts, tables, diagrams and graphics seen in this thesis were free software packages which are supported by large communities of mostly unpaid volunteers. Thank you to all who helped create **LibreOffice**, **GIMP**, **T_EXLive**, and **Linux Mint Debian**.

Zu guter Letzt, doch nicht am geringsten, sei den Menschen aus meinem privaten Umfeld gedankt, die mich unterstützt und an mich geglaubt haben. Eure Hilfe war stets unsichtbar, doch stets unverzichtbar.

- **Rebecca** – du hast für mich die Stellung gehalten, damit ich meine Aufmerksamkeit diesem Werk widmen konnte. Hier ist es nun, auf deinem Rücken geschrieben. Auch wenn dir der lange Weg manchmal hoffnungslos erschien: Es war für etwas gut. Danke!
- Meinen Eltern **Monika und Ercan Ordu**, meinen verstorbenen Großeltern **Karl und Irmgard Leukel** und meiner Taufpatin **Ute Täfler** danke ich einmal mehr für die langjährige Förderung meiner Bildung, ohne die ich es niemals bis hierher geschafft hätte!
- Meinem ehemaligen Schullehrer **Dr. Ralf Mehlmann** danke ich herzlich für die Förderung meines Interesses an der Physik. Hier sieht man, wozu das alles führen kann!

Sollte jemand in dieser Liste fehlen, bitte ich um Nachsicht und empfehle die Lektüre ebendieser Dissertation, um zu verstehen, womit ich gerade den Kopf voll hatte.

Erklärung

Ich versichere, dass ich die von mir vorgelegte Dissertation selbständig angefertigt, die benutzten Quellen und Hilfsmittel vollständig angegeben und die Stellen der Arbeit – einschließlich Tabellen, Karten und Abbildungen –, die anderen Werken im Wortlaut oder dem Sinn nach entnommen sind, in jedem Einzelfall als Entlehnung kenntlich gemacht habe; dass diese Dissertation noch keiner anderen Fakultät oder Universität zur Prüfung vorgelegen hat; dass sie – abgesehen von unten angegebenen Teilpublikationen – noch nicht veröffentlicht worden ist, sowie, dass ich eine solche Veröffentlichung vor Abschluss des Promotionsverfahrens nicht vornehmen werde. Die Bestimmungen der Promotionsordnung sind mir bekannt. Die von mir vorgelegte Dissertation ist von Prof. Dr. Stephan Schlemmer betreut worden.

Lebenslauf

Persönliche Angaben

Name: Matthias Hakan Ordu
Adresse: Liblarer Straße 23, 50321 Brühl
Geburtsdatum: 30.03.1983
Staatsangehörigkeit: Deutsch
Familienstand: Ledig, 1 Kind

Wissenschaftliche Ausbildung, Lehr- und Berufserfahrung

- Wissenschaftliche Hilfskraft, I. Physikalisches Institut, Universität zu Köln 2015 – heute
- Promotionsstudium in Experimentalphysik, Universität zu Köln 2011 – heute
Nebenprojekt: Bau eines labortauglichen 4K-SIS-Heterodynenempfängers um 345 GHz
- Gutachter für das *Journal of Infrared, Millimeter, and Terahertz Waves* 2011 – heute
- Mitglied des DFG-Sonderforschungsbereichs (SFB) 956 2011 – heute
Stellvertretender Sprecher des SFB 956 Studierendenrats 2014 – 2015
Mitwirkung am Kunstprojekt „Dialog der Sterne“ des SFB 956 2013 – 2014
- Wissenschaftlicher Mitarbeiter, I. Physikalisches Institut, Universität zu Köln 2011 – 2015
- Assistent im Physikalischen Praktikum B (Bachelor 5. – 6. Semester) 2007 – heute
Aufbau und Betreuung der Experimente:
„Stirlingmotor“ und „Infrarotabsorption in CO₂ (Treibhauseffekt)“
Stellvertretende Organisation des Lehrbetriebs
- Studentische Hilfskraft, I. Physikalisches Institut, Universität zu Köln 2007 – 2011
- Studium der Physik, Universität zu Köln 2003 – 2011
Abschluss: Diplom-Physiker (Gesamtnote: 1,5)

Nichtwissenschaftliche Berufserfahrung und Schulbildung

- Freier Mitarbeiter bei Übersetzungsservice Rebecca Göderz, Brühl 2009 – heute
Internes Lektorat Englisch – Deutsch, Spanisch – Deutsch; Buchhaltung;
Steuerberatung; IT; Webdesign
- Zivildienst bei der ev. Kirchengemeinde Mülheim am Rhein, Köln 2002 – 2003
- Abitur am Rhein-Gymnasium, Köln 2002
Durchschnittsnote: 1,7
- Betriebspraktikum als IT-Techniker bei Siemens AG, Köln 1999
- Katholische Grundschule Horststraße, Köln 1989 – 1993

Köln, den 22. Februar 2016